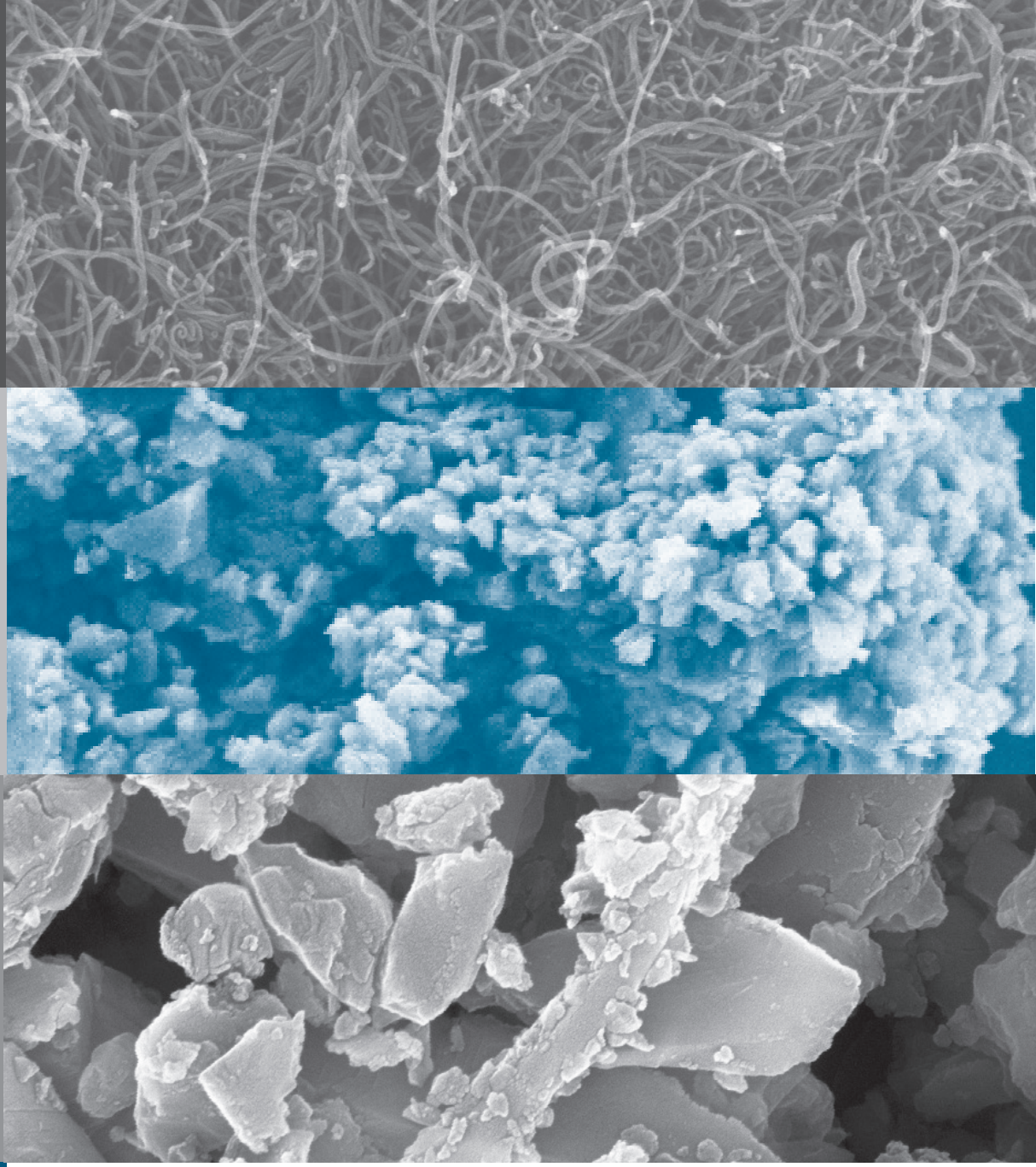

Improved hydrogen sorption kinetics in wet ball milled Mg hydrides

Li Meng

JÜLICH
FORSCHUNGSZENTRUM

Mitglied der Helmholtz-Gemeinschaft

Schriften des Forschungszentrums Jülich
Reihe Energie & Umwelt / Energy & Environment Band / Volume 93

Forschungszentrum Jülich GmbH
Institute of Energy and Climate Research (IEK)
Materials Synthesis and Processing (IEK-1)

Improved hydrogen sorption kinetics in wet ball milled Mg hydrides

Li Meng

Schriften des Forschungszentrums Jülich
Reihe Energie & Umwelt / Energy & Environment Band / Volume 93

ISSN 1866-1793 ISBN 978-3-89336-687-3

Bibliographic information published by the Deutsche Nationalbibliothek.
The Deutsche Nationalbibliothek lists this publication in the Deutsche Nationalbibliografie; detailed bibliographic data are available in the Internet at http://dnb.d-nb.de.

Publisher and Distributor:	Forschungszentrum Jülich GmbH Zentralbibliothek 52425 Jülich Phone +49 (0) 24 61 61-53 68 · Fax +49 (0) 24 61 61-61 03 e-mail: zb-publikation@fz-juelich.de Internet: http://www.fz-juelich.de/zb
Cover Design:	Grafische Medien, Forschungszentrum Jülich GmbH
Printer:	Grafische Medien, Forschungszentrum Jülich GmbH
Copyright:	Forschungszentrum Jülich 2011

Schriften des Forschungszentrums Jülich
Reihe Energie & Umwelt / Energy & Environment Band / Volume 93

D 294 (Diss., Bochum, Univ., 2010)

ISSN 1866-1793
ISBN 978-3-89336-687-3

The complete volume ist freely available on the Internet on the Jülicher Open Access Server (JUWEL) at http://www.fz-juelich.de/zb/juwel

Kurzfassung

Die vorliegende Arbeit beschreibt die Anwendung des Nasskugelmahlens zur Verbesserung des Wasserstoff-Sorptionsverhaltens von Feststoff-Hydriden durch die Optimierung der Mikrostruktur. Im Vergleich zum konventionellen Kugelmahlen bietet das Nasskugelmahlen Vorteile in Bezug auf die Mikrostruktur und das Wasserstoff-Sorptionsverhalten. Durch den Einsatz von Tetrahydrofuran (THF) konnten beim Nasskugelmahlen von MgH_2 im Vergleich zum Trockenkugelmahlen deutlich kleinere Partikelgrößen mit etwa der siebenfachen spezifischen Oberfläche erzeugt werden. Zwar werden gegenüber dem Ausgangsmaterial die Korngrößen durch das Kugelmahlen grundsätzlich deutlich reduziert, jedoch sind diese nach dem Nasskugelmahlen infolge der durch das THF verringerten Reibung größer als nach dem Trockenkugelmahlen. Die verbesserte Partikelgrößen und spezifische Oberfläche des nasskugelgemahlenen MgH_2-Pulvers bestimmen insbesondere bei niedrigen Temperaturen die Wasserstoff-Sorptionskinetik von MgH_2. Weiterhin zeigen diese Materialien gute Eigenschaften bei zyklischer Sorption, was entscheidend für eine industrielle Anwendbarkeit ist.

Bei Verwendung dreier verschiedener Dotierungen zeigten die MgH_2-Pulver ein noch verbessertes Sorptionsverhalten bei geringer Degradation. Dabei erwies sich Nb_2O_5 am wirksamsten. Verglichen mit dem nasskugelgemahlenen, reinen MgH_2 ergaben sich mit den Dotierungen ähnliche Partikelgrößen, jedoch deutlich kleinere Korngrößen. Zwei Gründe werden als Ursache für das verbesserte Wasserstoff-Sorptionsverhalten vermutet. Einerseits die verringerte Korngröße, andererseits gibt es Hinweise in der Literatur, dass durch eine Oxidation die Sorptionskinetik verbessert werde, was auch der Grund für eine verringerte Sorptionskapazität sein könne. Eine Verlängerung des Nasskugelmahlens von MgH_2 mit Nb_2O_5 bewirkte deutlich größere spezifische Oberflächen, hierdurch verbesserte sich das Wasserstoff-Sorptionsverhalten weiter.

Außerdem wurde ein einfaches Simulationsmodell mit der spezifischen Oberfläche als relevantem Parameter entwickelt, mit dem die experimentell gefundenen Ergebnisse recht gut nachvollzogen werden können.

Abstract

In this work, wet ball milling method is used in order to improve hydrogen sorption behaviour due to its improved microstructure of solid hydrogen materials. Compared to traditional ball milling method, wet ball milling has benefits on improvement of MgH_2 microstructure and further influences on its hydrogen sorption behavior. With the help of solvent tetrahydrofuran (THF), wet ball milled MgH_2 powder has much smaller particle size and its specific surface area is 7 times as large as that of dry ball milled MgH_2 powder. Although after ball milling the grain size is decreased a lot compared to as-received MgH_2 powder, the grain size of wet ball milled MgH_2 powder is larger than that of dry ball milled MgH_2 powder due to the lubricant effect of solvent THF during wet ball milling. The improved particle size and specific surface area of wet ball milled MgH_2 powder is found to be determining its hydrogen sorption kinetics especially at relatively low temperatures. And it also shows good cycling sorption behavior, which decides on its industrial applicability.

With three different catalysts MgH_2 powder shows improved hydrogen sorption behavior as well as the cyclic sorption behavior. Among them, the Nb_2O_5 catalyst is found to be the most effective one in this work. Compared to the wet ball milled MgH_2 powder, the particle size and specific surface area of the MgH_2 powder with catalysts are similar to the previous ones, while the grain size of the MgH_2 with catalysts is much finer. In this case, two reasons for hydrogen sorption improvement are suggested: one is the reduction of the grain size. The other may be as pointed out in some literatures that formation of new oxidation could enhance the hydrogen sorption kinetics, which is also the reason why its hydrogen capacity is decreased compared to without catalysts. After further ball milling, the specific surface area of wet ball milled MgH_2 with Nb_2O_5 is much larger than the standard wet ball milled MgH_2 with Nb_2O_5 and the corresponding sorption behavior is also much improved.

Furthermore, a simple model is built up in which the key parameter is main specific surface area and it follows the experimental desorption results quite well.

Content

Chapter 1 Introduction 1

1.1 Current energy society 1

1.2 Hydrogen in energy systems 2

1.3 Hydrogen storage 4

1.4 Motivation and outline 7

Chapter 2 Theory of solid state hydrogen storage and model development I

2.1 Classification of solid hydrogen storage materials 10

2.2 Metal hydrides 11

2.2.1 The Lennard-Jones Potential curve 11

2.2.2 Sorption mechanism and thermodynamics 13

2.2.3 Surface reactions 15

2.2.4 Magnesium hydride 17

2.2.5 Sodium alanate 18

2.3 Evaluation of hydrogen storage capacity 20

2.3.1 Static volumetric principle 20

2.3.2 Thermogravimetry 21

2.4 Modelling 22

2.4.1 Background of modelling 22

2.4.2 Chou's model 25

2.4.3 Introduction of own model for hydrogen sorption 27

Chapter 3 Experimental methods 30

3.1 Suspension production and characterization 30

3.1.1 Mechanical alloying and mechanical milling 30

3.1.1.1 Types of mills 31

3.1.1.2 Milling variables 35

3.1.2 Suspension production 38

3.1.3 Viscosity measurement 40

3.1.4 Particle size measurement 42

3.2 Powder production and characterization 43
3.2.1 Powder Production 43
3.2.2 X-Ray Diffraction (XRD) 43
3.2.3 Scanning Electron Microscopy (SEM) 45
3.2.4 Specific surface area measurement (BET measurement) 45
3.3 Sorption test and characterization 46
Chapter 4 Experimental results and discussion 49
4.1 Improvement of MgH_2 properties 49
4.1.1 Improvement of MgH_2 properties due to processing 49
4.1.1.1 Characteristics of MgH_2 suspension 49
4.1.1.2 Characteristics of MgH_2 powder 53
4.1.1.3 Sorption behaviour of MgH_2 powder 57
4.1.1.4 Sorption cycling behaviour of MgH_2 powder 62
4.1.1.5 P-C-T curves and Van't Hoff plot 65
4.1.2 Improvement of MgH_2 properties due to catalysts 67
4.1.2.1 Microstructure modification of wet ball milled MgH_2 with catalysts 67
4.1.2.3 Improvement of sorption behaviour due to catalysts 73
4.1.2.4 Improvement of cycling behaviour due to catalysts 81
4.1.2.5 Thermodynamics of wet ball milled MgH_2 with catalysts 84
4.1.2.6 Further improvement of the milling conditions for wet ball milled MgH_2 powder with Nb_2O_5 catalyst 86
4.2 Comparison of results with literature values 90
4.3 Mechanism of hydrogen desorption of wet ball milled MgH_2 powder 94
4.3.1 Typical features of hydrogen desorption behaviour of wet ball milled MgH_2 powder 95
4.3.2 Build up the modelling and the corresponding modelling results 95
4.4 Hydrogen sorption of $NaAlH_4$ 109
Chapter 5 Summary of the conclusions 111
Reference 114

Chapter 1 Introduction

1.1 Current energy society

Energy is the essential requirement for any aspect in the world and the more developed a nation, the more energy it needs. The total primary energy supply throughout the world has increased from 58.9 Quadrillions Btu (Btu is short term of British thermal unit, which is a traditional unit of energy and 1 Btu = 1.06kJ) in 1968 to 99.3 Quadrillions Btu in 2008, a rise of 68% in 40 years and will increase further in the future years [1]. This increase is a result of growth in the world population and a general rise in prosperity.

Fossil fuels are the major part of the current energy resources, which are consumed for a wide variety of purposes, e.g. heating houses, cooking, transportation and manufacturing of industrial products. In 2008, in the whole world 83.5 Quadrillions Btu fossil fuels were consumed and however, only 7.3 Quadrillions Btu renewable energy and 8.5 Quadrillions Btu nuclear electric energy were consumed [1]. As a result fossil fuels will be used up in the near future, e.g. with the current consumption of oil which is approx. 28 billion barrels a year, the proven reserves would last for only 40 years [2].

The production, processing and transportation of fossil fuels generally have considerable environmental impact at local and regional levels. Among them the most significant negative impact is caused by fossil fuel combustion, during which a lot of air pollutants are formed: sulphur oxides (SO_x), nitrogen oxides (NO_x), volatile organic carbon (VOC), carbon monoxide (CO) and particular matter. Besides, the main green effect gas carbon dioxide (CO_2) is also produced in large quantities [3]. Currently, most of the world energy requirement for transportation and heating (which is two thirds of the primary energy consumption) is derived from oil or natural gas. The advantages of them are high energy density from its consumption and easy to transport due to liquid or gaseous forms. Unfortunately, over half of all greenhouse gas emissions and a large fraction of air pollutant emissions come from the

combustion of hydrocarbon fuels. Both limited reserve of fossil fuels and the pollution from its combustion promote that today's world is facing an urgency in developing alternative fuels. Among various alternatives, hydrogen fuel offers the highest potential benefits in terms of diversified supply and reduced emissions of pollutants and greenhouse gases [3].

1.2 Hydrogen in energy systems

Hydrogen has a weight-based heating value of more than two times as large as that of currently used fuels and it is carbon-free, which means that there is zero or near-zero emission at the point of use [4, 5, 6, 7]. These properties are considered to enable hydrogen to compete with the current fuels and thus the hydrogen cycle is more attractive. In of hydrogen economy, the principal focus of hydrogen technology is mainly on the safe and affordable utilization of hydrogen as an alternative fuel based on seamless integration of generation, distribution and storage technologies [3]. A possible hydrogen cycle is illustrated in **Figure 1.1**. It shows that energy from photovoltaics, wind and hydropower is converted into electricity, which is then used in an electrolyzer to split water into hydrogen and oxygen. Oxygen is released to the atmosphere and hydrogen is intermediately stored, transported and distributed before being electrochemically consumed by oxygen (from the atmosphere) in a fuel cell whereby electricity is produced with the by-product water or steam released into the atmosphere [8].

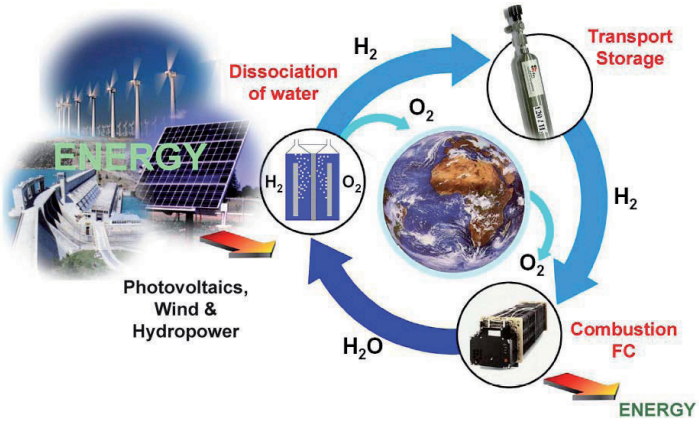

Figure 1.1 Hydrogen cycle in hydrogen society based on renewable energy and fuel cells [8].

Generally hydrogen doesn't occur on earth in the form of hydrogen molecules but is chemically bound in water and in liquid or gaseous hydrocarbons. Hydrogen can be produced using a variety of starting materials, derived from both renewable and non-renewable sources, through many different process routes. The world production of hydrogen is around 45-50 Mt per year, most of which is derived from natural gas by steam reforming [3]. The remainder is obtained basically from oil and coal by the partial oxidation process [3]. Only 4% of the worldwide hydrogen is generated by electrolysis with electricity produced from sustainable energy sources e.g. solar, wind, hydro power or directly from photolysis [3,9].

Hydrogen production is presently directly associated to its use, for example, an ammonia or methanol plant is likely to be located next to a hydrocarbon cracker or steam reformer. Small scale hydrogen in the form of compressed gas or cryogenic liquid is transported from production site to major end users via pipelines, by road in tanker trucks [10]. Two technical problems appear to be relevant:

1. The pipelines should be sealed closely and the materials for pipelines should be carefully chosen due to the very high mobility of hydrogen and its ability to permeate many solids with low density.
2. High pressure of hydrogen is required and thus adequate compressors are needed for handling high volume, high pressure hydrogen systems.

One of the most critical factors in inducting hydrogen economy is transportation and on-vehicle storage of hydrogen. Several different methods of storing hydrogen are used, which can be classified into three basic methods: compressed hydrogen storage, liquid hydrogen storage, and solid hydrogen storage. Their advantages and limitations will be shown in later **Chapter 1.3**.

In the hydrogen society energy conversion from stored H_2 into usable form can be realized through either a conventional internal combustion engine (ICE) or a fuel cell (FC). Due to Carnot cycle efficiency limitations of the ICE, a fuel cell (FC) is preferred [11], because it offers a potential efficiency approximately twice as large as that of an ICE [4]. In the FC H_2 recombines with O_2 to produce electricity and water which is the only by-product [12]. In the ICE hydrogen is combusted with an oxidizer (usually air). In this period the expansion of the high temperature and pressure gases, which are produced by the combustion, directly applies force to a movable component of the engine, such as the pistons or turbine blades and by moving it over a distance, generate useful mechanical energy [13].

1.3 Hydrogen storage

The U.S. Department of Energy (DOE) has been involved for almost 30 years in research and development (R&D) programs related to advanced vehicular technologies and alternative transportation fuels [14]. In the programs it is pointed out the actual challenges for hydrogen storage. The principal challenges to improve hydrogen storage technologies relate to the efficiency, size, weight, capacity, cost, durability and refuelling time of the hydrogen storage system.

- Efficiency

  Energy efficiency is a challenge for all hydrogen storage approaches. The energy required to get hydrogen in and out of storage is an issue for reversible solid-state materials storage systems. In addition, the energy associated with compression and liquefaction must be factored in when considering compressed and liquid hydrogen storage technologies, which will be detailed introduced later [15].

- Weight and Volume

  At the moment both weight and volume of the hydrogen storage systems are too high, thus they are inadequate for vehicles compared to the conventional petroleum fuelled vehicles. Thus the compact, lightweight hydrogen storage systems are needed for vehicles [15].

- Durability

  As the requirement from the DOE's targets of hydrogen storage [16], materials and components are needed to allow hydrogen storage systems with a lifetime at least 1500 refuelling cycles [15].

- Refuelling time

  There is a need to develop hydrogen storage kinetics in order to achieve the targets that hydrogen storage systems with refuelling times of less than 3min, over the whole lifetime of the system [15].

At the moment several different methods of storing hydrogen are available. These can be generalized into three basic methods:

Compressed Hydrogen Storage: Generally at ambient pressure and temperature one kilogram of hydrogen occupies 11m³ of volume and consequently its storage requires enormous compression [17]. High strength steel or other metals are an option from a strength perspective; however, diffusion of hydrogen into the steel and weight of the steel are major issues for vehicular storage [17]. Compressed hydrogen gas at 34.5MPa has a density of 23.5kg/m³. During this compressing process, 8.5% of the energy content of the hydrogen is required [18]. Besides, the filling rate of compressed hydrogen gas must be monitored and regulated to reduce the temperature increase of the gas in the tank during rapid filling [18].

Liquid Hydrogen Storage: Liquid hydrogen has a density of 70.8kg/m³ [18]. Five kilograms of hydrogen only require 71L of volume, and this is adequate on a volumetric basis for current vehicles [17]. The phase diagram in **Figure 1.2** for hydrogen shows the various forms of hydrogen as a function of pressure and temperature [5,19]. There is a small zone which starts at the triple point, and ends at the critical point where hydrogen exists as a liquid with a density of 70.8kg/m³ at 20K.

The energy utilized for cooling to liquid hydrogen requires an estimated 30% of the lower heating value of hydrogen, which is substantially higher as compared to compressed hydrogen [17]. There is a period during compressing over which hydrogen will warm up in a storage vessel and convert to gas and will require venting from the liquid hydrogen tank. This period is the dormancy period, and there is one estimate of 4% of liquid hydrogen converting to hydrogen gas per day for a 4.6kg tank, and the whole tank of liquid hydrogen can last for about 25days [18, 20].

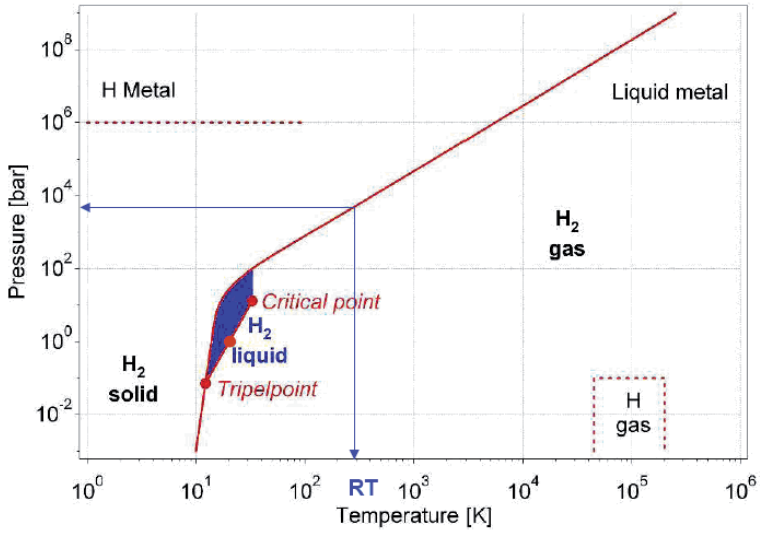

Figure 1.2 Simple phase diagram of hydrogen [21].

Solid hydrogen storage: There are a lot of different classes of solid hydrogen storage materials which will be introduced in **Chapter 2** with more details. Here are some examples about solid hydrogen materials in order to highlight the difference to compressed and liquid hydrogen storage.

Recently, a number of reversible hydrides have been studied for hydrogen storage. As a system, hydrides have a substantial advantage on a volumetric basis (0.13-0.15kgH_2/L), much safer and easier to be transformed in comparison with compressed hydrogen and liquid hydrogen [17].

The simplest groups of the hydrides are the so-called metal or intermetallic hydrides such as $LaNi_5H_6$ and $FeTiH_2$, which operate at lower temperatures of 100°C and lower pressures [18]. The weight percent of such hydrides range from 1.5 to 3wt%, and the volumetric density range from 0.05 to 0.12kgH_2/L [17]. Higher gravimetric and volumetric densities can be achieved by the higher-temperature hydrides such as MgH_2 and $MgNiH_2$ at 300-350°C. Their high gravimetric property is significantly better than the low temperature hydrides mentioned before, but the high temperature requirement probably precludes their use in vehicles. In this case, $NaAlH_4$ is attracted due to its low operating temperature about 100°C and relatively reasonable hydrogen storage capacity 4-5wt%. The sodium alanate doped with Ti has a hydrogen content by weight twice as that of the traditional low-temperature hydrides. However, the slow reaction kinetics and low reversibility continue to be a major issue for vehicular applications [17]. There are some complex hydrides with much higher gravimetric mass percentage than the DOE requirement, e.g. $LiBH_4$ with 13.8wt% of hydrogen, however, its too high operating temperature and pressure as well as low reversibility still need a lot of research.

Besides, the activated carbon is also interesting for hydrogen storage. The activated carbon storage system operates at 77K and a pressure of 50-100atm. The system consists of a cryogenic tank filled with the carbon and auxiliary components to control the release of the hydrogen. Generally liquid N_2 is used to cool the hydrogen during the filling process of the system. The hydrogen is stored as a liquid in the micropores of the carbon and as a low temperature gas in the macropores between the carbon particles. The hydrogen storage capacity of carbon is dependent on its surface area and pore size distribution and the extent to which the carbon particulates are compacted prior to loading into the cryogenic tank. For a carbon density of 0.3g/cm³, the weight metrics are 7.6wt% at 50atm and 9.5wt% at 100atm [18].

1.4 Motivation and outline

From the above introduction of different materials for hydrogen storage, in this thesis MgH_2 is selected as the main research object due to its simple composition,

high gravimetric, low cost and abundance in the earth's crust. Unfortunately, two major problems concerning MgH_2 have precluded its use in practical applications [22]. First, MgH_2 is a quite stable compound, which means low equilibrium pressure and then high temperature operation for any storage application. The second problem is its poor desorption and absorption kinetics. This work is mainly concerned with the latter problem. Nevertheless, extensive research in the last decade led to a rather strong consensus that nanocrystalline solid hydrides, specifically obtained by mechanical milling in various types of ball mills and characterized by the existence of nano-sized grains within the hydride particles, exhibit substantially enhanced desorption and absorption kinetics [23]. In the milling process, both particle size and grain size are inevitably reduced. Therefore a very fundamental question arises whether particle size and grain size plays the main role on the improved hydrogen desorption and absorption kinetics. In this work, based on the mechanical ball milling of MgH_2 powder, an organic chemical is used in order to improve the microstructure of MgH_2 powder, which should lead to a further improvement of hydrogen desorption and absorption kinetics. Through comparison with dry ball milled MgH_2 powder under the same milling conditions which gives a different ratio of grain and particle refinement, a classification whether particle size or grain size is the critical parameter for improvement of hydrogen sorption behaviour can be made clear. Besides, another aim of this work is to investigate what kind of microstructure of MgH_2 powder can favour its sorption behaviour.

Absorption and desorption of metal hydrides is a heterogeneous phase transformation. This reaction combines a number of steps taking place in series [24]. For example during the absorption process H_2 transport to the surface of metals, H_2 dissociation, H chemisorption, surface-bulk migration, H diffusion and nucleation and growth of hydride/metal phases take place. The slowest step of those mentioned previously is the rate-determining one. In this work, a spherical model is built up, with which the mechanism of hydrogen desorption is explained and the determining step of the kinetics is found. The modelling results will be compared to the experimental results in order to further adjust the modelling parameters.

Moreover, co-milling with some catalysts, e.g. transition metals, transition metal oxides, carbon nanotubes and so on could also be a benefit for hydrogen sorption behaviour of the MgH_2 powder. However, till now the mechanism how catalysts influence the sorption behaviour is still not clear and several different theories are available. In this work three different catalysts are used and it is intended to compare the effects of them on improvement of hydrogen sorption behaviour. Through analysis of the microstructure of wet ball milled MgH_2 with catalysts and the analysis of the sorption behaviour by the built up spherical model, the mechanism of catalysts influencing on hydrogen sorption will be explained.

Based on the experimental and modelling results, it will be summarized which advantages of wet ball milling compared to dry ball milling with respect to microstructure of hydrides are found and which kind of microstructure is beneficial for an enhanced hydrogen sorption kinetic. The mechanism of hydrogen sorption behaviour will be explained based on both experimental and modelling results.

Besides, another solid material sodium alanate is used as hydrogen storage material in this work. The main motivation for studying sodium alanate is to outline its desorption behaviour dependent on temperature profiles and check whether wet ball milling can improve its hydrogen sorption behaviour as found for MgH_2 powder.

Chapter 2 Theory of solid state hydrogen storage and model development

2.1 Classification of solid hydrogen storage materials

There are multiple classes of hydrogen storage materials. These classes store hydrogen by different methods. Generally the hydrogen storage materials are classified as follows:

- **Metal hydrides and complex hydrides**

Many metals and alloys are capable of reversibly storing large amounts of hydrogen and forming metal hydrides. In these, atoms of hydrogen can settle in tetrahedral or octahedral holes, called interstitial sites [17]. It is hard to define a strict criterion to distinguish interstitial hydrides from ionic and covalent hydrides. The high hydrogen capacities of interstitial hydrides, especially volumetric storage capacities in comparison to pure hydrogen and the high reversibility of the system have led them to be considered as hydrogen storage materials.

- **Organic chemical hydrides**

By utilizing hydrogen and dehydrogenation cycles of organic compounds, one can achieve storage of hydrogen [17]. For example decalin can store hydrogen with high capacities (7.3wt%, 64.8kgH_2/m³). However, the energy and equipment requirements for the dehydrogenation reaction of the organic chemical hydrides are too expensive for on-board use. Recently there is a promising hydrogen storage group named metal organic frameworks (MOFs) consist of metal ions and clusters linked together by organic unit [25]. The extraordinary low density (1.00 to 0.20 g/cm^3) and high surface area (500 to 4500 m^2/g) of these materials make them as a candidates for the storage and separation of gases [26].

- **Carbon materials**

Various forms of carbon such as graphite, nanotubes, and activated carbon with high surface area can be utilized for hydrogen storage. The single wall carbon

nanotubes can store 2.5-3wt% hydrogen [4, 27, 28]. the best activated carbon as reported, absorbed 4.8 wt% H at a temperature of 87 K and a pressure of 59 atm of hydrogen [29].

- **Silica microspheres**

Hydrogen can be stored in hollow silica microspheres. At high temperatures (e.g. 500°C), the wall of these microspheres is permeable to hydrogen, and at ambient temperatures the wall is impermeable to hydrogen [17]. High pressure hydrogen can be filled at high temperature and then they are locked inside by cooling. When needed, the trapped hydrogen can be easily released by heating [17].

As demonstrated in **Chapter 1**, the focus in this work is on the metal hydrides.

2.2 Metal hydrides

Metal and metal alloys can combine with hydrogen to form metal hydrides by three different bond types: (1) ionic, (2) covalent, and (3) metallic [8]. This chapter mainly focuses on the metallic hydride and complex metal hydrides. Metallic hydrides are normally binary compounds, in which the hydrogen acts as a halogen and obtains an electron from the other metal to form a hydride ion (H^-) to form the same stable orbital electron configuration of helium with two electrons filling up the s-orbital [30]. Chemical formula for binary ionic hydrides is generally presented by MH_x, e.g. LiH or MgH_2.

2.2.1 The Lennard-Jones Potential curve

The reaction between a metal and hydrogen can be expressed by the following reactions:

$$M(s) + x/2\ H_2\ (g) \rightleftharpoons MH_x\ (s) + Heat \qquad \textbf{(2.1)}$$

From the left to right side, this process is called absorption process, which can be described by a simplified one-dimensional Lennard-Jones potential curve [8, 31]. The

hydrogen molecules are firstly attracted to approach the metal surface due to the Van der Waals force, leading to the physisorbed state.

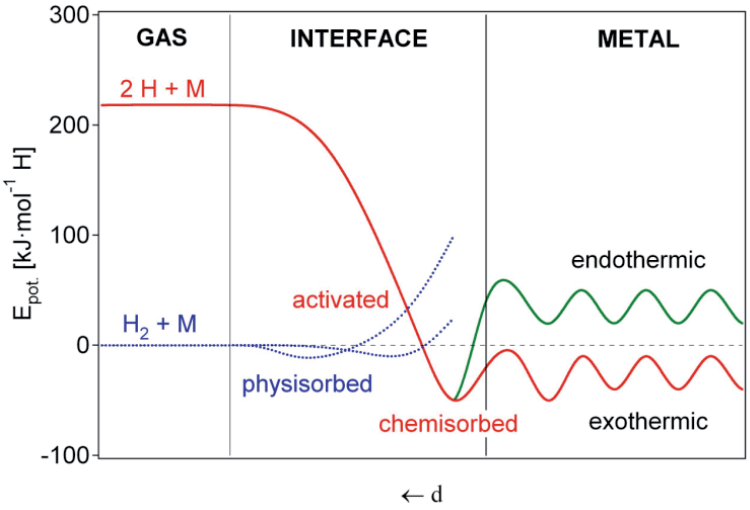

Figure 2.1 Lennard-Jones potential of hydrogen approaching a metal surface [8].

Figure 2.1 shows physisorption happens at the interface between hydrogen atmosphere and metal surface, about one hydrogen molecule radius (≈0.2nm) from the metal surface [8]. Close to the metal surface, the hydrogen has to overcome an activation barrier (the intersection between blue dash and red solid lines) for dissociation and formation of the hydrogen metal bond. The height of the activation barrier depends on the surface elements involved. The top of the barrier is sometimes called the transition state, given by the nearest distance possible to a molecule approaching the surface before dissociation. Hydrogen atoms sharing their electron with the metal atoms at the surface are called chemisorbed hydrogen ($E_{Chem} \approx -50kJ/molH$) [32]. Then the chemisorbed hydrogen atom can jump in the subsurface layer and finally diffuse and occupy the interstitial sites of the metal lattice.

2.2.2 Sorption mechanism and thermodynamics

Figure 2.2 shows the individual steps during the reaction between hydrogen and metal including bulk process. The formation of the metal hydride can be divided into the following reaction steps:

Dissociation and adsorption: The first step is the dissociation of hydrogen molecules and chemical adsorption of hydrogen atoms on the metal/hydride surface (see. **Figure 2.2** a, b and c).

Surface penetration: From the surface the hydrogen atoms can penetrate into the sub-surface (see **Figure 2.2** d).

Bulk diffusion: From the sub-surface, the hydrogen atoms can diffuse into the bulk to form a solid solution (see **Figure 2.2** e). The formed metal hydrogen solid solution is called α-phase.

Hydride formation: Hydrogen atoms in the bulk of additional hydrogen atoms (the formed solid solution) can create hydride nuclei which can grow to larger hydride grains by trapping of additional hydrogen atoms (see **Figure 2.2** f). The formed metal hydride is called β-phase.

Desorption is the reverse process, i.e. the hydride phase decomposes and hydrogen atoms diffuse in the bulk to the sub-surface and subsequently to the surface, where the hydrogen atoms recombine and desorb as H_2 molecule.

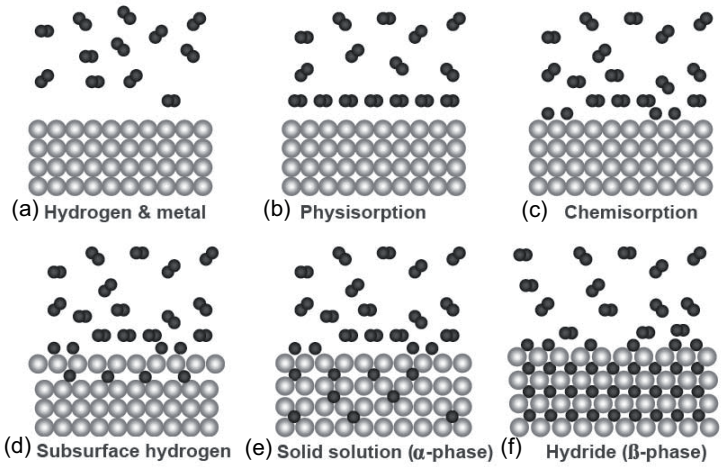

Figure 2.2 Schematic mechanism of hydrogen absorption of metal [4,33]

During the absorption of hydrogen with increasing hydrogen pressure first of all the diluted phase (α-phase) is formed. In the diluted solution phase, a further pressure increase is needed to induce a higher hydrogen content. At a certain equilibrium hydrogen pressures the metal hydride β-phase starts to form and two phases coexist. The β-phase grows at the cost of the α-phase. In the coexisting period, the pressure does not increase further until forming a complete β-phase. Then a larger pressure increase is needed again to induce a higher hydrogen content. The hydrogen pressure at which the transition takes place at a given temperature is the so-called "plateau pressure" of the equilibrium between both phases [3]. For different isothermal sorption temperatures the plateau pressure obeys the Van't Hoff equation, here take Mg as an example (here p_0 is reference pressure, 10^5Pa):

$$Mg(s) + H_2 \leftrightarrow MgH_2(s)$$

$$\Delta G^0 = -RT \ln K_{eq} = -RT \ln\left[\frac{p}{p_0}\right] = \Delta H^0 - T\Delta S^0$$

$$\ln\left[\frac{p}{p_0}\right] = -\frac{\Delta H^0}{R} \cdot \frac{1}{T} + \frac{\Delta S^0}{R} \qquad \textbf{(2.2)}$$

where ΔG^0 is the standard change of Gibbs free energy, ΔH^0 is the standard enthalpy change and ΔS^0 is the standard entropy change during the phase transformation. p_0 is the standard pressure, i.e. $p_0 = 1.01 \times 10^5 Pa$. K_{eq} is the equilibrium constant at the absolute temperature T. R represents the gas constant.

With the equilibrium conditions, thermodynamic characteristics of the hydrogen sorption can be derived from a plot of $\ln[p/p_0]$ vs 1/T (**see Figure 2.3**). The intercept with $\ln[p/p_0]$ axis yields the sorption entropy, which amounts approximately to the standard entropy of hydrogen ($S^0 = 130 JK^{-1}mol^{-1}$ [43]). The slope of the plot is a measure of the sorption enthalpy, which is independent on the isothermal desorption temperature.

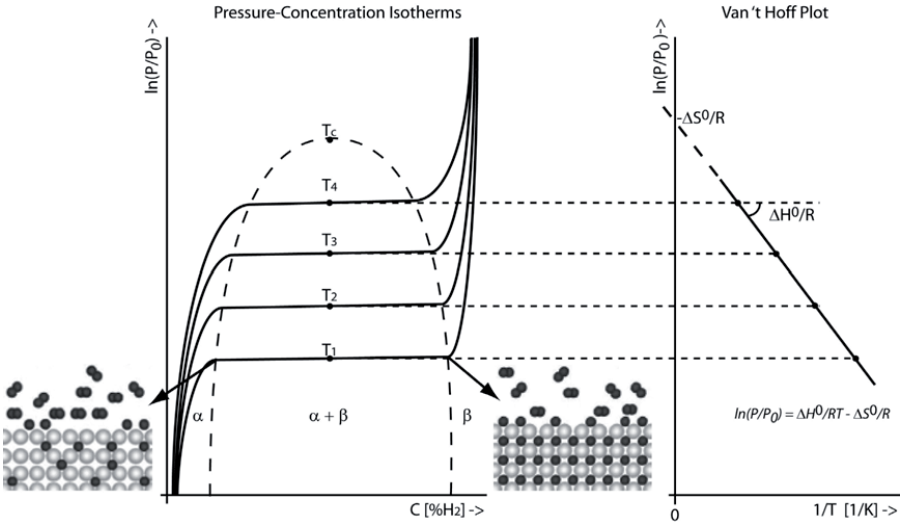

Figure 2.3 The Pressure-Concentration-Isothermal/Temperature Plot (PCT) and corresponding Van't Hoff Plot. The α-phase is the solid solution of hydrogen and metal and β-phase is the metal hydride phase [3].

2.2.3 Surface reactions

Hydrogen absorption in metal hydrides mentioned in **Chapter 2.2.2** involves two main steps: dissociation of the hydrogen molecule and transport of the chemisorbed hydrogen toward the subsurface and adjacent diffusion in the bulk (see **Figure 2.2).** From the diffusion data, it is known that hydrogen transport inside metal or metal

hydrides is fast enough to provide high hydrogen absorption and desorption rates at room temperature. However, most metal hydrides system show slow absorption and desorption rates. Thus it is concluded that dissociation and surface adsorption controlled by the surface properties are critical for determining the sorption kinetics.

In order to improve the sorption kinetics, the first important step is to understand the surface structure and its corresponding properties. Generally the equilibrium position of atoms on the top surface is different from the normal lattice periodicity of the bulk corresponding to the minimum of the free energy of a crystal. The contraction between the top surface and subsurface is often ranging 5-10%. Generally the crystallographically open surfaces [fcc(110), bcc(111) and (211), hcp(1010)] are more susceptible to relaxation and reconstruction than the closed-packed surfaces [fcc(111), bcc(110)] [34].

With the increase of hydrogen pressure, the adsorbed H atoms form disordered or at lower temperatures ordered surface phases [8]. Experimental and theoretical evidence prove that the chemisorbed H atom occupy not only sites on top of the first metal atom layer, but also sites between and below top layer metal atoms. The subsurface H atom is generally accompanied by a strong surface reconstruction (surface hydride formation) and can be considered as an intermediate stage between metal hydrogen solution and bulk metal hydride.

The deformation of the lattice structure during absorption of hydrogen in metals leads to the energy change of metals. When the hydrogen molecules approach to the surface of the metal, they are attracted by the weak van der Waals force leading to the so called physisorption. The corresponding heats of physisorption are very small (>-5kJ/molH_2), and physisorption experiments are performed at low temperatures. Chemisorption of atomic hydrogen occurs through electronic bonding states formed by H 1s and metal states [35]. The heat of chemisorption is of the order of 20-60kJ/molH [35]. Both hydrogen adsorption by the top surface, dissociation from molecules to atoms, and chemisorption are called surface activation, during which the activation barrier should be overcome.

The surface and bulk absorption processes are not completely separated. The coverage of the surface, and therefore the number of free active sites for dissociation, depends also on the concentration of hydrogen in the bulk [36, 37]. During hydrogen sorption, the concentration of hydrogen in the bulk as well as at the surface, changes until it reaches its equilibrium.

2.2.4 Magnesium hydride

Magnesium hydride is considered as one of the most interesting options for the reversible storage of hydrogen due to a high gravimetric storage capacity with the theoretical maximal value of 7.6wt%; almost four times higher than those of conventional room temperature interstitial hydrogen storage alloys such as AB_5, AB and AB_2 systems [38]. Its high abundance and low price are also in favour of automotive applications. However, its main drawbacks are its high sorption temperature (>300°C) and its sluggish sorption kinetics [39, 40].

Two promising methods have been applied in order to overcome these limitations: (i) improved kinetics is obtained by reducing the Mg particle size and by adding a catalyst [41] and (ii) thermodynamic destabilization is achieved by alloying with other elements. However, the sorption capacity is always reduced by improved thermodynamic and kinetic properties. For example, Mg_2NiH_4 shows improved [42]. Furthermore, improvements in sorption temperature of milled and doped magnesium compounds are often lost in the first few cycles of charging and discharging with H_2, whereas the H_2-storage materials need a lifetime of at least hundreds of cycles. In order to avoid sacrifices in hydrogen storage capacity, distorting the MgH_2 lattice should be achieved with low amount of alloying or additives. Instead distorted lattice a lower sorption temperature is attained by high energy milling introducing lattice defects and decreasing the particle size of Mg or MgH_2.

During absorption of magnesium, as hydrogen is introduced into the hexagonally close-packed (HCP) Mg metal lattice, the H atoms initially occupy tetrahedral interstitial sites, forming the α-phase [43]. Upon further addition of H, the β- MgH_2 is

formed. The β- MgH_2 phase has a body centre tetragonal lattice of rutile type, space group $P4_2/mnm$, with lattice parameters a = 0.452nm and c = 0.301nm [44,45] and a density of $1.42\times10^3 kg\cdot m^{-3}$ Mg atoms are octahedcrally coordinated to six H atoms, while the H atoms are coordinated to three Mg atoms in a planar coordination [45]. When the β- MgH_2 is subjected to high compressive stress (7-8GPa), which might occur during high energy ball milling process, a new γ-phase is induced. γ- MgH_2 has an orthorhombic structure with space group P*bcn* and lattice parameters a = 0.453nm, b = 0.544nm, and c = 0.493nm [45, 46]. The packing and coordination of the Mg and H atoms are not affected by the transformation but the H octahedral surrounding each Mg atom are deformed, as the straight octahedral chains are in a zigzag form [43].

2.2.5 Sodium alanate

A novel approach for hydrogen storage is to combine the favourable kinetics and thermodynamics of conventional metal hydrides with that of the large hydrogen storage capacity of organic molecules such as CH_4. The properties of a class of materials called alanates which have the chemical composition $M(AlH_4)_n$ (M= Na, Li, K, Mg) are favorable for hydrogen storage, although the temperature of which hydrogen desorbs is high.

Alanates are complex metal hydrides, the main difference between the alanates and metallic hydrides is the transition to an ionic or covalent compound upon hydrogen absorption. The hydrogen in the alanates is often located in the corners of a tetrahedron with Al in the center. The negative charge of the anion, $[AlH_4]^{-1}$, is compensated by a cation, e.g. Li or Na. The hydride complexes of the tetrahydroaluminates are known to be stable and decompose only at elevated temperatures, often above the melting point of the complexes. Among alanates sodium alanate ($NaAlH_4$) is a promising material for hydrogen storage with a theoretical reversible storage capacity of about 5.5wt%. It is one of the known complex hydride with favourable thermodynamics and an acceptable gravimetric storage capacity for use in conjunction with a polymer electrolyte membrane (PEM)

fuel cell system, which operates at about 90°C. Reversibility kinetics of $NaAlH_4$ is improved upon addition of titanium and/or zirconium dopants, which causes a dramatic decrease in the primary crystal size. Hydrogen is released from $NaAlH_4$ in two steps [47]:

$3NaAlH_4 \leftrightarrow Na_3AlH_6 + 2Al + 3H_2$ (3.7wt% hydrogen released)

$Na_3AlH_6 \leftrightarrow 3NaH + Al + 1.5H_2$ (another 1.8wt% hydrogen released)

Thus, $NaAlH_4$ first decomposes to evolve molecular hydrogen and forms an intermediate compound Na_3AlH_6, which further decomposes to NaH with the formation of additional metallic aluminium and hydrogen. The first reaction could happen at above 180°C with desorption of 3.7wt% hydrogen, whereas the second reaction takes place about 240~250°C and can release an additional 1.8wt% hydrogen [48]. Absorption is preferably done at 10MPa and slightly above 100°C. The kinetics are faster at higher temperatures, but a drawback is the increase in the hydrogen equilibrium pressure with increasing temperature. Therefore, a compromise between fast rate and equilibrium processing is needed.

In 1997 it was discovered that the kinetic barriers for the hydrogen uptake of the material can be lowered considerably when a transition metal promoter is added to the alanate [49]. The first attempts to introduce the catalyst were made using wet impregnation techniques with Ti tetra-n-butylate ($Ti(BuO)_4$) and Fe ethylate ($Fe(OEt)_2$), dissolved in toluene and diethylether [48]. Numerous other materials including rare earth compounds were also investigated [48].

Besides wet impregnation, the catalyst can also be incorporated by adding the precursor to the alanate and ball-milling the mixture under inert conditions [50, 51]. This technique was applied in screening experiments with many elements and confirmed early results which had indicated that Ti based promoters are most active for the hydrogen exchange [52, 53, 54]. Furthermore, it was shown in cycling experiments that the $TiCl_3$ loading had a negative effect on the H_2 capacity. In contrast, the $TiCl_3$ loading had a positive effect on the dehydrogenation kinetics,

which increased with increasing $TiCl_3$ loading. However, a full understanding of how and why Ti can lower the hydrogen desorption temperature is not fully obtained.

According to a theoretical study on the role of Ti in diminishing the hydrogen binding energy in the crystalline sodium alanate ($NaAlH_4$) has been determined. This effect is one of the main contributions to a decrease in the hydrogen desorption temperature. But what is the mechanism of Ti effecting in the sodium alanate is still not clear. A number of experiments involving x-ray diffraction, neutron and Raman scattering, and electron spectroscopy have yielded controversial results. While some of them suggest that Ti occupies the Na sites in the bulk lattice, others report the presence of Ti on the surface in the form of amorphous Ti-Al alloys. A recent experiment result has even suggested that Ti must diffuse in the bulk during the absorption/desorption cycling.

2.3 Evaluation of hydrogen storage capacity

The different procedures for the determination of the amount of gas absorbed or desorbed may be divided into two groups: (a) through measuring pressure change in gas phase, i.e. gas volumetric methods and (b) through direct determination of change in mass by gravimetric methods. Actually, both methods are adequate for measuring hydrogen sorption kinetics.

In this part, the two different principles for measuring hydrogen sorption kinetics will be introduced detailed. A comparison will give the respective advantages and disadvantages. Based on each principle, the corresponding instrument available will be introduced here.

2.3.1 Static volumetric principle

In the static volumetric determination a known quantity of gas is usually admitted to a confined volume, maintained at constant temperatures. As absorption takes place, the pressure in the certain volume falls until equilibrium is established. The amount of hydrogen absorbed can be calculated from the change of the pressure in a fixed

volume and under constant temperatures with the aid of the gas laws. The volume of the dead space must, of course, be known accurately: it is obtained by pre-calibration of the confined volume filled with helium (calculated from its pressure).

If the establishment of equilibrium is sufficiently fast, this method may be regarded as equivalent to a 'static' procedure, e.g. at a slow and constant rate under quasi-equilibrium conditions.

The desorption, which is the reverse procedure of absorption, is also measured with the same principle. Before the starting of desorption, the confined volume is evacuated. And then temperature is heated up to the definite value and the pressure in the confined volume increases until equilibrium is established. The amount of hydrogen desorbed from material is also calculated through the pressure increase in a fixed volume and under constant temperature with the help of gas laws.

The instrument BELSORP-HP used in this work is based on the volumetric principle. The measurement temperature ranges from room temperature to 400°C using a small heater and up to 800°C for the bigger one. The loading pressure can reach up to 12MPa. As adsorption gas as in addition to H_2 also N_2, Ar, CO_2, CH_4 and other inert gases can be used. In this work, H_2 works as the adsorption gas for the experiments of hydrogen storage materials.

2.3.2 Thermogravimetry

In a gravimetric instrument the mass change of the sample is directly measured in order to determine the desorption rate. The main difficulty when using conventional gravimetric instruments is the direct connection of the measuring cell (sample atmosphere) to the weighing instrument. The balance can be damaged or disturbed by the measuring atmosphere, which can be adversely affected by flushing gases and pollution. These limitations considerably reduce the field of applications of conventional measuring devices.

The ISOsorp instruments from Rubotherm Präzisionsmesstechik GmbH are gravimetric adsorption and/or absorption analysis. The ISOsorp instruments are

equipped with Rubotherm's patented "Magnetic Suspension Balance" so that they can perform highly precise gravimetric sorption measurements with different gases a large pressure and temperature range.

2.4 Modelling

2.4.1 Background of modelling

Kinetics of hydrogen desorption and absorption from the metal hydrides (MH) is a complex process which involves gaseous hydrogen and two (α-solid solution of hydrogen in the metal and a β-hydride) or more solid H-containing phases. Hydrogen desorption includes processes (elementary stages) proceeding in the bulk (phase transformation and bulk diffusion) and in the surface layer (recombination of hydrogen molecules). Since each stage contributes to the overall process, the slowest process is the rate-limiting process.

The most frequently applied model of the kinetics of phase transformations relevant to the process of H desorption was proposed by Avrami [55] and Johnson and Mehl [56]. The model is based on the approach describing the kinetics as nucleation and growth of the nuclei of a new phase within the bulk of the matrix phase as the rate-limiting step.

Then Rudman [57] has extended this approach to apply it to the metal-hydrogen systems considering hydrogen diffusion as the rate-limiting process for the kinetics of desorption.

Mintz and Zeeri [58] further developed this approach. Their analysis extended a consideration of the conventional case of a shrinking core moving with a constant velocity of an interface to include two more complex situations:

(i) shrinking core moving with decelerating velocity; the process is controlled by hydrogen diffusion through the growing layer of the product;

(ii) random multiple nucleation and growth of the new phase in the bulk material.

In addition, and for the first time, the factors causing deviation of the kinetic characteristics of the absorbed powders from behaviour of a single hydride particle were taken into account. The influence of the: (i) particle size distribution; (ii) particle shape variations; (iii) time delay in the beginning of the desorption process in the specific particle compared to the average process in the powder were considered.

Recently, Castro and Meyer [59] have studied kinetics of hydrogen desorption by modelling of the spectra of hydrogen thermal desorption. Here, the desorption is described in a rather general way. They related four alternative rate-limiting steps including:

(i) bulk diffusion;

(ii) phase transformation;

(iii) bulk to surface transfer;

(iv) H-H recombination on the sample surface.

However, for practical purposes, it is very difficult to apply general models similar to those presented above to describe the experimental thermal desorption spectra for the specific metal-hydrogen systems. One reason for that is the ambiguity of the interpretation of the results in the case of the overlapping rate-limiting stages.

Up to the present model fitting method is extensively used to study the kinetic mechanism of gas-solid reaction including desorption/absorption reactions in hydrogen storage alloys. Although many studies on the kinetic mechanisms of absorption reaction were performed, due to the complex heterogeneous solid-gas properties of the desorption/absorption reaction, the theoretical investigation on the hydrogen absorption and desorption of kinetics in MgH_2 based alloys is still not satisfactory in comparison with the experimental study. There are basically three models describing different critical kinetic steps during absorption behaviour:

(1) Surface reaction model

In the surface reaction model the chemisorption is the critical step of the sorption process, e.g. dissociation of hydrogen molecules during absorption and recombination of hydrogen molecules during desorption [43]. The transformed fraction α s proportional to the sorption time:

$$\alpha = kt \quad \textbf{(2.3)}$$

Where k is the reaction rate and independent on t.

(2) The Johnson-Mehl-Avrami (JMA) model

The JMA model describes the nucleation of randomly dispersed second phase particles independently from location, i.e. surface or bulk. The growth rate k of new phase is controlled by temperature and is independent of time [58,60]. Its equation is:

$$\left[-\ln(1-\alpha)\right]^{1/n} = kt \quad \textbf{(2.4)}$$

where n depends on the dimensional growth of new phase, e.g. $n=2$ or $n=3$ correspond to two- or three-dimensional growth of the existing nuclei, respectively. It is only valid when the nucleation rate is not time dependent. Under both situations, the rate-limiting step is the moving of the metal/metal hydride interface [60] under the assumption that the hydrogen diffusion is quick enough.

(3) Contracting volume (CV) model

As mentioned above in JMA model the nucleation and growth of the new phase start randomly on the particle surface or in the bulk, i.e. there is no priority on the surface of the existing particles. However, in CV model, nucleation starts from the surface of the existing particles and then continuous growth towards the bulk. In this case, when hydrogen diffusion is not rate-limiting step, when the growth of new phase has the constant interface velocity, the kinetics corresponds to [60]:

$$1-\left[1-\alpha\right]^{1/n} = kt \quad \textbf{(2.5)}$$

where $n=2$ or $n=3$ depends on two- or three-dimensional growth of the new phase, respectively.

When hydrogen diffusion is the rate-limiting step, the metal/hydride interface doesn't move with constant velocity but with a decreasing velocity with growth of the new phase. In this case, the velocity is described as [60]:

$$1-\left(\frac{2\alpha}{3}\right)-(1-\alpha)^{2/3} = kt \quad \textbf{(2.6)}$$

The different kinetics equations are listed in **Table 2.1** summarized by G.Barkhordarian et al.[60]:

Table 2.1 Kinetic equations in different situations [60]

Kinetic equation	Situation description
$\alpha = kt$	Surface reaction model (chemisorption) [58,60]
$[-\ln(1-\alpha)]^{1/3} = kt$	JMA model: three dimensional growth of existing nuclei with constant velocity of metal/hydride interface movement [58, 61]
$[-\ln(1-\alpha)]^{1/2} = kt$	JMA model: two dimensional growth of existing nuclei with constant velocity of metal/hydride interface movement [58, 60,61]
$1-(1-\alpha)^{1/3} = kt$	CV model: three dimensional growth of existing nuclei with constant velocity of metal/hydride interface movement [58,60]
$1-(1-\alpha)^{1/2} = kt$	CV model: two dimensional growth of existing nuclei with constant velocity of metal/hydride interface movement [58,60]
$1-\left(\frac{2\alpha}{3}\right)-(1-\alpha)^{2/3} = kt$	CV model: three dimensional growth of existing nuclei with decreasing velocity of metal/hydride interface movement, i.e. diffusion controlled [58,60]

2.4.2 Chou's model

Chou's model has further simplified the shrinking model for absorption. The model was built up based on the metal with initial absorption process. **Figure 2.4** shows the geometry for a model of reaction between hydrogen gas and spherical metal particle. A general mechanism of absorption reaction for a particle can be described as the following seven steps, they are [62]:

i. Hydrogen in the bulk gas phase transfers to the surface of the metal particle;
ii. Hydrogen diffusion through the boundary layer between gas phase and solid particle;
iii. Physisorption of hydrogen molecules on the solid surface;
iv. Dissociation of hydrogen molecules and chemisorption;
v. Surface penetration of hydrogen atoms;

vi. Diffusion of hydrogen atoms through the hydride product layer to the hydride/metal interface;

vii. Chemical reaction and nucleus formation producing hydride.

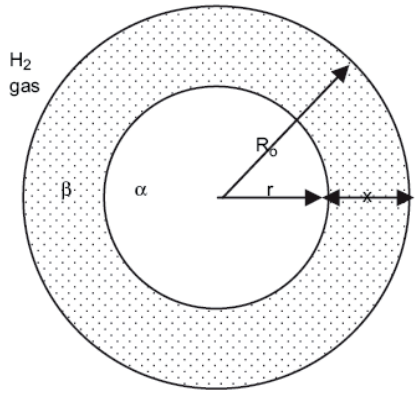

Figure 2.4 Geometry for the model description of the reaction between hydrogen gas and metal particle.

Chou thought the above seven steps are basically enough to describe the mechanism of absorption process from the point of view of the mathematical formalism. In most cases, only two steps (v) and (vi) could be the rate-controlling steps because the "penetration of hydrogen atoms" and "the diffusion of hydrogen atoms through hydride layer" are slower than others. In his model, all powders of metal or alloy are assumed to be spherical balls with the same density and radius as shown in **Figure 2.4** where α represents metal phase with radius of r, β is hydride layer with thickness of x. The whole particle is a ball of radius R_0. The transferred (or reacted) fraction of hydride ξ at radius r and time t can be calculated in the light of the following equation:

$$\xi = 1 - \left(\frac{r}{R_0} \right)^3 \tag{2.7}$$

Through differentiation of Eq. (2.5) with respect to time t,

$$\frac{d\xi}{dt} = -\frac{3r^2}{R_0^3} \frac{dr}{dt} \tag{2.8}$$

where the derivative of radius *r* corresponding to time is proportional to the rate of absorption process, i.e.,

$$\frac{dr}{dt} = \frac{V(r)}{v_m} \tag{2.9}$$

where *V* is the reaction rate (velocity of boundary movement) and v_m is a constant coefficient that depends on the density of the storage material. Combining Eqs. (2.7) - (2.9),

$$\frac{d\xi}{dt} = -\frac{3(1-\xi)^{\frac{2}{3}}}{R_0}\frac{V(r)}{v_m} \tag{2.10}$$

With the initial condition, $t = 0, \xi = 0$, and the characteristic reaction time t_c, which means the required time for completion of the adsorption reaction and is defined as:

$$t_c = \frac{v_m R_0}{V} \tag{2.11}$$

The transferred fraction of hydride ξ can be expressed as:

$$\xi = 1 - (1 - \frac{t}{t_c})^3 \tag{2.12}$$

In general case, steps (i) and (ii) are much faster than others so that they are ruled out from Chou's consideration. For other steps becoming rate-controlling, the characteristic reaction time can be derived

2.4.3 Introduction of own model for hydrogen sorption

The shrinking model is also used in our work. The initial material in our own experiments is MgH_2 not Mg thus the modelling started from the hydrogen desorption. At the beginning of the hydrogen desorption, the hydrogen atoms on the top surface of the particles are first separated from the Mg hydride to form the Mg hydrogen solid solution, i.e. α-phase. And then the desorbed hydrogen atoms form the hydrogen molecules on the surface which are released into the atmosphere. With the growth of

α-phase, there is a α-phase shell formed around the core of the β-phase (see **Figure 2.5a**).

The absorption of Mg is the reverse situation. At the beginning of the absorption, the hydrogen molecules are physisorbed on the top surface of the particles due to the van der Waals force and then the hydrogen molecules dissociate into hydrogen atoms. The Mg atoms on the top surface of the particle will firstly combine with hydrogen atoms to form the β-phase. With the growth of β-phase, a shell of β-phase is formed around the core of the α-phase (see **Figure 2.5b**).

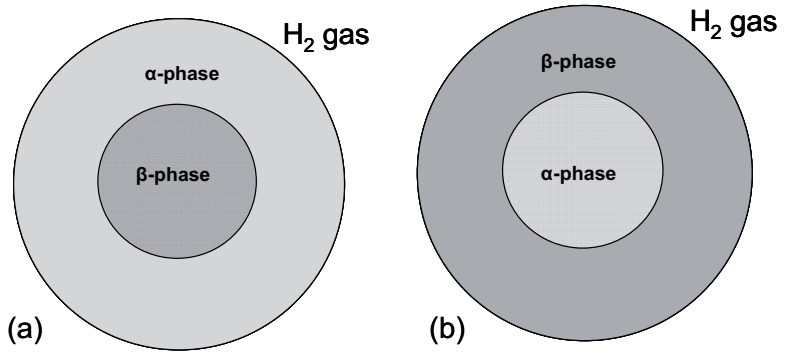

Figure 2.5 Shell model of (a) hydrogen desorption and (b) hydrogen absorption of MgH_2 particles

In this model the particle sizes distribute homogeneously and the particle size is characterized with the characteristic size radius *d*. The rate of the total hydrogen permeation is therefore proportional to the surface area *S*, i.e. ~ d^2, and the hydrogen content of the particle is proportional to its volume *V*, ~ d^3. From these suggestions it is to expect that the characteristic sorption time τ (especially for short time intervals) depends linearly on the characteristic particle size d, i.e. $\tau \sim d$. The characteristic sorption time τ is defined as the time for full completion of the sorption, i.e. from the beginning of sorption to the sorption completion. Thus the characteristic sorption times of two particles 1 and 2 are expected to relate to each other like their characteristic particle sizes, $\tau_1 / \tau_2 \sim d_1 / d_2$.

In our own modelling of hydrogen desorption behaviour, the real experimental conditions are taken into account. For example, the temperature distribution in the instrument and the influence of hydrogen pressure inside of the sample holder. The temperature inside of the sample holder and the instrument is not homogeneous and the temperature point where the pressure sensor is located is cooler than the real sample temperature of point where sample is located. Thus if the pressure value shown by the sensor will be used for the modelling, the temperature difference should be considered. Besides, the BELSORP-HP is based on the volumetric principle. During the whole desorption process, the desorbed hydrogen stayed in the closed volume which is connected to the sample. Thus with the desorption progressing, the hydrogen pressure around the sample increases, which increases the reverse reaction rate and finally blocks the further desorption. The large amount of sample is used for the desorption experiment, the higher hydrogen pressure will be observed during the desorption inside the sample holder. To take into account the influences of the reverse reaction, i.e. absorption, the sample mass is also considered in our own model. Thus the modelling of hydrogen desorption predicts two different regions: (a) the desorbed hydrogen pressure is low and the hydrogen desorption follows a linear kinetic; (b) desorbed hydrogen pressure is high enough and the desorption processing is close to the degassing equilibrium.

The ratio of $\sqrt{S}/\sqrt[3]{V}$ is dependent on geometry/morphology of the particle. It is 2.684 for particle with tetrahedron geometry and 2.199 for spherical geometry showing the influence of the surface area. From the comparison of modelling and experimental results, the relationship between desorption kinetics and specific surface area of particles will be concluded.

The detailed building up the model and the description of the basic equations will be introduced in **Chapter 4.3**.

Chapter 3 Experimental methods

In this thesis a new method to produce nano-structural powder is introduced, which is different from the traditional dry ball milling. The new method is wet ball milling of hydrogen storage powder to produce stable suspension first, and then based on the suspension, nano-structured hydrogen storage powder, which has certain benefits for hydrogen sorption properties.

3.1 Suspension production and characterization

As briefly introduced above, the first step for the production of nano-structural hydrogen storage powder with the new method is to produce nano-structural stable suspension with the high energy ball milling. Thus in this chapter the milling process and its corresponding parameters are described first.

3.1.1 Mechanical alloying and mechanical milling

The most typical processing techniques to produce the nanocrystalline hydrogen storage powder are mechanical alloying (MA) or mechanical ball milling (MM) [63]. Mechanical alloying (MA) describes the process when mixtures of powders (different metals or alloys/compounds) are milled together. During this process material transfer is involved to obtain a homogeneous alloy. On the other hand, for the milling uniform (often stoichiometric) composition powders, such as pure metals, intermetallics, or pre-alloyed powders are used. No material transfer happens in the process of mechanical milling (MM) [64]. Generally the time of mechanical milling is shorter than that of mechanical alloy. In this work the aim is improve the microstructure of MgH_2 particles but not to form a new alloys. Thus in this work the processing is mechanical milling.

3.1.1.1 Types of mills

Different types of high-energy milling equipment are used to produce mechanically milled powders. They differ in their capacity, efficiency of milling and additional arrangements for cooling, heating, etc. A brief description of the different mills is listed below.

- SPEX shaker mills

Shaker mills such as SPEX mills (see **Figure 3.1**), which mill about 10-20g of the powder at a time, are most commonly used for laboratory investigation [64]. This kind of mill has one vial, containing the sample and grinding balls, secured in the clamp and swung energetically back and forth several thousand times a minute. The back-and-forth shaking motion is combined with lateral movements of the ends of the vial, so that the vial appears to be describing a figure 8. With each swing of the vial the balls impact against the sample and the end of the vial, both milling and mixing the sample. Because of the amplitude (about 5cm) and speed (about 1200rpm) of the clamp motion, the ball velocities are high (on the order of 5m/s) and consequently the colliding force of the ball on the powder is large. Therefore, these mills can be considered as high-energy mills [64].

The most recent design of the mills has provision for simultaneously milling the powder in two vials to increase the throughput. A variety of vial materials is available for the SPEX mills and these include hardened steel, alumina, tungsten carbide, zirconia, stainless steel, silicon nitride, agate, plastic, and methacrylate [64].

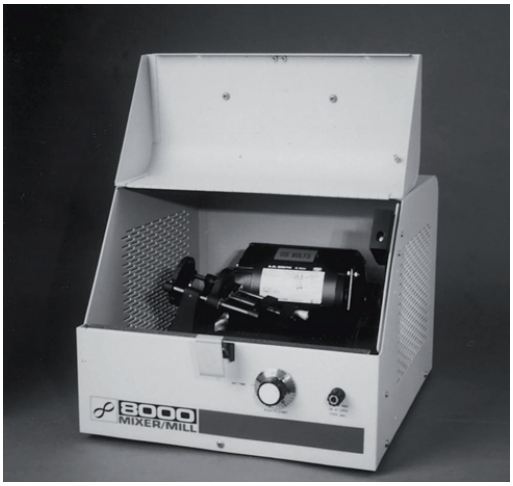

Figure 3.1 Schematic of SPEX 8000 mixer/mill in the assembled condition [64].

- Planetary ball mills

Another popular mill for conducting MA or MM experiments is the planetary ball mill in which a few hundred grams of the powder can be milled at a time. The planetary ball mill owes its name to the planet-like movement of its vials. These are arranged on a rotating support disk and a special drive mechanism causes them to rotate around their own axes [64] (see **Figure 3.2**). The centrifugal force produced by the vials rotating around their own axes and that produced by the rotating support disk both act on the vial contents, consisting of material to be ground and the grinding balls. Since the vials and the supporting disk rotate in opposite directions, the centrifugal forces alternately act in like and opposite directions (see **Figure 3.3**). This causes the grinding balls to run down the inside wall of the vial – the friction effect, followed by the material being ground and grinding balls lifting off and travelling freely through the inner chamber of the vial and colliding against the opposing inside wall-the impact effect [64].

Figure 3.2 Schematic of planetary ball mill in the assemble situation in this work

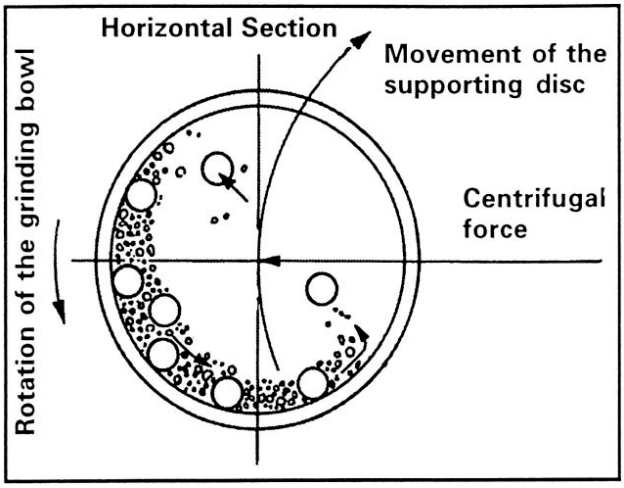

Figure 3.3 Schematic depicting the ball motion inside the ball mill [64].

- Attritor mills

A conventional ball mill consists of a rotating horizontal drum half-filled with small steel balls. As the drum rotates the balls drop on the metal powder that is being ground; the rate of grinding increases with the speed of rotation [64]. At high speeds, however, the centrifugal force acting on the steel balls exceeds the force of gravity, and the balls are pinned to the wall of the drum. At this point the grinding action stops.

To overcome this drawback from conventional ball mill the attritor mills are used. Attritors can mill large quantities of powder (from about 0.5 to 40kg) at a time [64]. An attritor (a ball mill capable of generating higher energies) consists of a vertical drum with a series of impellers inside it. Set progressively at right angles to each other, the impellers energize the ball charge, causing powder size reduction because of impact between balls, between balls and container wall, and between balls, agitator shaft, and impellers (see

Figure 3.4) [64]. Some size reduction appears to take place by interparticle collisions and by ball sliding. A powerful motor rotates the impellers, which in turn agitate the steel balls in the drum.

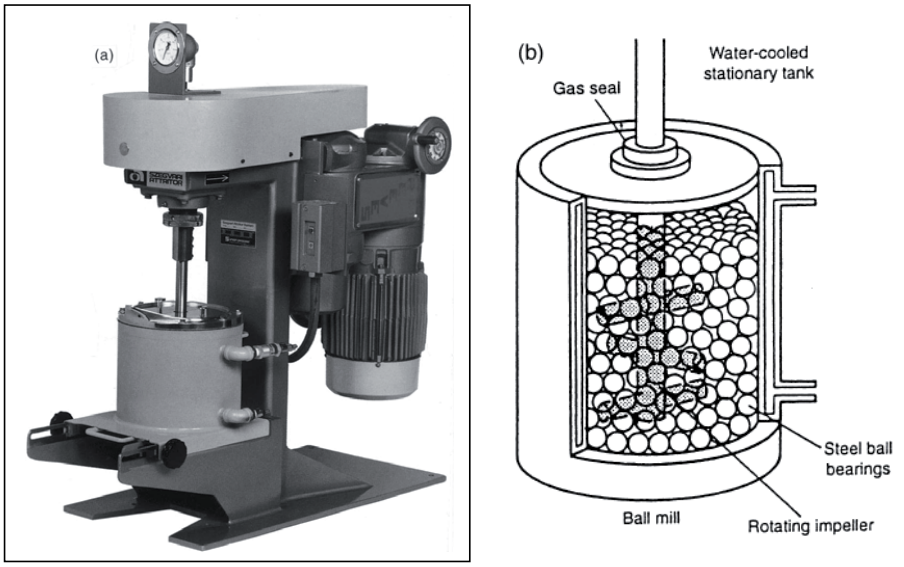

Figure 3.4 Schematic of (a) Model 1-S attritor. (b) Arrangement of rotating arms on a shaft in the attrition ball mill. [64]

In this work, due to the mass of powder and high rotation speed wanted, the planetary ball milling is used to improve the microstructure of the powder.

3.1.1.2 Milling variables

Mechanical ball milling is a complex process and hence involves optimization of a number of variables to achieve the desired product phase and/or microstructure. Except the type of mill, some of the important parameters that have an effect on the final constitution of the powder are [64]:

- Milling container

The material used for the milling container (grinding vessel, vial, jar, and bowl etc) is important due to the impact of the grinding medium on the inner walls of the container; some material will be dislodged and get incorporated into the powder [64]. This can contaminate the powder or alter the chemistry of the powder. Hardened steel, tool steel, hardened chromium steel, tempered steel, stainless steel, WC-Co, WC-lined steel [65], and bearing steel are the most common types of materials used for the grinding vessels. In this work hardened steel was used as container material. And the milling container can be tightly sealed by screws.

Figure 3.5 Photo of one of the hardened steel milling containers used in this work

- Milling speed

Typically it is realised that the faster the mill rotates the higher is the energy input into the powder. But depending on the design of the mill there are certain limitations for the employed maximal speed [64]. For example, in the normal mill the moving speed of the milling balls increase with the increasing rotation speed of the mill.

Above a critical speed, the balls will be pinned to the inner walls of the vial and do not fall down to exert any impact force. Therefore, the maximum speed should be just below this critical value so that the balls can produce the maximal collision energy [64].

Another limitation to the maximum speed is that at high speeds (or intensity of milling), the temperature of the vial may reach a high value. This may be advantageous in some cases where diffusion is required to promote homogenization and/or alloying in the powders. But, in some cases, this increase in temperature may be a disadvantage because the increased temperature accelerates the transformation process and results in the decomposition of supersaturated solid solutions or other metastable phases formed during milling [66]. Additionally, the high temperatures generated may also lead to the grain growth. It has been reported that during nanocrystal formation, the average crystal size increases and the internal strain decreases at higher milling intensities due to the enhanced dynamical recrystallization [67]. The maximal temperature reached is different in different types of mills and the values vary widely.

- Milling time

The time of milling is the most important parameter. Normally the time is so chosen in such a way that a steady state between the fracturing and cold welding of the powder particles is achieved [64]. The times required vary depending on the type of mill used, the intensity of milling, the ball-to-powder ratio, and the temperature of milling. These times have to be decided for each combination of the above parameters and for the particular powder system. However, it should be realized that the level of contamination increases and some undesirable phases form if the powder is milled for times longer than required [68]. Therefore, it is desirable that the powder is milled for the proper duration. In this work the milling time varied between 24h and 72h.

- Grinding medium

Hardened steel, tool steel, hardened chromium steel, tempered steel, stainless steel, WC-Co, and bearing steel are the most common types of materials used for the grinding medium (milling ball). However, some special materials are used for the

grinding medium and these include copper, titanium, niobium, zirconia, agate, yttria stabilized zirconia (YSZ), etc.

The size of the milling ball also influences the milling efficiency. Generally speaking, a large size (and high density) of the milling balls is useful since the larger weight of the balls will transfer more impact energy to the powder particles [64]. Throughout this work YSZ milling balls with diameter 2mm and 5mm were used.

- Ball-to-powder weight ratio

The ratio of the weight of the milling balls to the powder (BPR), sometimes referred to as charge ratio (CR), is an important variable in the milling process. The BPR has a significant effect on the time required to achieve a particular phase in the powder being milled. The higher the BPR, the shorter is the milling time required. With a high BPR, because of an increase in the weight proportion of the balls, the number of collisions per unit time increases and consequently more energy is transferred to the powder particles [64]. In this work, BPR of 5:1 and 10:1 were used in comparision.

- Milling atmosphere

As during milling the surface of the powder is highly activated, a reaction between powder surface and the milling atmosphere might take place. As a protection of the powder the milling containers are always filled with the pure argon or helium [64].

- Suspension solvent

The most common solvent is water. Other commonly-used solvents are organic chemicals [64]. These organic solvent usually have low boiling-point and evaporate easily, leaving the dissolve substance behind. Due to high reactivity of hydrogen storage material with water, organic solvent are used to produce suspensions. In this work, two kinds of solvents n-hexane and tetrahydrofuran (THF for short later) were used for comparison. Hexane has a chain structure (see **Figure 3.6**), and is frequently used as an inert solvent because it is non-polar [69]. THF is a moderately polar solvent and can dissolve a wide range of nonpolar and polar chemical compounds [70, 71]. Solvent polarity is defined and measured in several different ways, one of the most common method is the description by the **dielectric constant, ε**. High dielectric

constant solvent usually have high dipole moments. When subject to the electric field of an ion, such polar molecules orient themselves to oppose the field, and shield it [69].

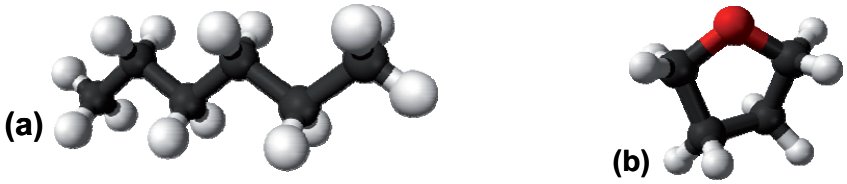

Figure 3.6 Molecular schematic of (a) n-hexane and (b) THF. White ball represents H atom, black ball represents C atom and red ball states for O atom.

3.1.2 Suspension production

In this work, hydrogen storage materials such as MgH_2 and $NaAlH_4$ powder were used as starting material. The initial magnesium hydride powder (90 % purity; the rest being metallic magnesium) was purchased from ACROS ORGANICS and the initial sodium aluminium hydride (93% purity) was purchased from Sigma Aldrich. In the traditional high-energy ball milling process, Mg hydride is ball milled in various types of vials filled with inert gas and the whole process is totally dry. In contrast, wet ball milling, as the name suggests, implies the help of solvent as n-hexane or tetrahydrofuran. In our studies, n-hexane and tetrahydrofuran (THF) were purchased from Sigma Aldrich (n-hexane with 95% purity and water < 0.005%, THF without water and inhibitors and ≥ 99.5 % purity).

In **Chapter 3.1.2**, the most important milling parameters were introduced, which significantly influence on the suspension characteristics and further on the evaporated powder characteristics. However, not all the milling parameters mentioned in **Chapter 3.1.2** were variable in this work, only some have to be determined. All the pre-treatment for ball milling was done in a glovebox which was filled with argon atmosphere. Thus the milling container was also filled with argon atmosphere, i.e. milling atmosphere, which can prevent the oxidation and contamination of MgH_2 powder. The mill type was planetary ball mill with milling speed of 260rpm. The

milling vial was made of hardened steel with sealed cover and the corresponding grinding medium was YSZ in order to avoid the contamination of Fe in the MgH_2 powder. N-hexane and THF were selected as suspension solvent in order to compare the influence of unpolar and polar solvent on the characteristics of MgH_2 suspension. Thus the main variable milling parameters were milling time, ball-to-powder weight ratio (BPR) and size of grinding medium.

At the beginning n-hexane was used as the suspension solvent, four MgH_2 suspensions based on the different milling parameters were produced (see **Table 3.1**). For all the samples here the ball milling time was 72h.

Table 3.1 MgH_2 n-hexane Suspensions after 72h milling with different milling parameters

Suspension No.	MgH_2 mass percentage in suspension	BPR(ball-to-powder weight ratio)	YSZ grinding balls size
No.4-1	20%	5:1	Both 5mm and 2mm diameter YSZ milling balls with weight ratio 7:3
No.4-2	50%	5:1	Both 5mm and 2mm diameter YSZ milling balls with weight ratio 7:3
No.4-3	50%	10:1	Both 5mm and 2mm diameter YSZ milling balls with weight ratio 7:3
No.4-4	50%	10:1	Both 5mm and 2mm diameter YSZ milling balls with weight ratio 1:1

In comparison, MgH_2 THF based suspensions with 20wt%, 30wt%, 40wt% and 50wt% MgH_2 powder were also produced with the same method as mentioned above. For ball milling MgH_2 THF suspensions the BPR was 10:1 and only 5mm diameter YSZ milling balls were used. The ball milling time was also 72h.

In order to test the influence of catalysts on the hydrogen sorption of MgH2, wet ball milled MgH_2 with catalysts THF suspensions were also produced.

Except the MgH_2 powder and THF purchased from the same company as previously, the catalysts niobium ethoxide (Nb_2O_5 with 99.95% purity), vanadium (V with -325 mesh and 99.5% purity) were purchased from Sigma Aldrich. Single-wall

carbon nanotubes are supplied by Bayer MaterialScience AG (Product name is BAYTUBES C 150 P).

As-received MgH_2 powder, one kind of the above catalysts and THF organic solvent were mixed. The weight of the MgH_2 powder and catalyst is 20wt% of the mixture. Wet ball milling was performed for 72h under an Ar atmosphere in Fritsch planetary mill with YSZ balls (diameter=5mm) in a hard steel vial and with a ball to powder weight ratio of 10:1. All the before and after ball milling handling was performed in Glovebox with Ar atmosphere.

Besides, the nano-sized $NaAlH_4$ THF suspension was also produced with same method. 20wt% of as received $NaAlH_4$ and THF solvent were also milled in the hardened steel vial for 24h. YSZ milling balls had the diameter of 5mm and BPR was 10:1. Then the produced wet ball milled $NaAlH_4$ THF suspension was separated from YSZ balls under Ar atmosphere supplied in a glovebox..

3.1.3 Viscosity measurement

The viscosity of the MgH_2 THF suspensions with different weight percentages of MgH_2 powder was measured by the Physica Rheometer MCR100 (Anton Paar, Ostfildern, Germany). The rheometer measures the rheology of a liquid, suspension or slurry in response to the applied forces. There are two types of rheometers depending on the geometry of applied stress [72]. Rheometers that deal with shear stress are called shear rheometers, whereas rheometers that apply extensional stress are extensional rheometers. Physica Rheometer MCR100 (see **Figure 3.7**) is a shear rheometer.

Figure 3.7 Schematic of Physica Rheometer MCR100.

In the experiments, the MgH_2 THF suspensions were placed within the annulus of one cylinder inside another. One of the cylinders rotated with a setting speed, which determined the shear rate inside the annulus. At this moment the suspension tended to drag the other cylinder around. The force which suspension exerted on the latter cylinders was measured and recorded by the software and converted to shear stress.

In a Newtonian fluid, the relation between the shear stress and the strain rate is linear. The ratio of them is defined as viscosity.

$$\eta = \frac{\tau}{\dot{\gamma}}[Pa \cdot s] \qquad \textbf{(3.1)}$$

where η is viscosity with the unit $[Pa \cdot s]$, τ is shear stress and $\dot{\gamma}$ is strain rate with the unit of Pa and s^{-1}, respectively.

All other fluids which don't show this "ideal" flow behaviour are called non-Newtonian fluids. In a non-Newtonian fluid, the relation between shear stress and the strain rate is nonlinear, and sometimes dependent on time. Viscosity is defined as the ratio of shear stress and strain rate.

For Newtonian fluid, viscosity is a constant (see **Figure 3.8**) while for non-Newtonian fluids, it is not a constant any more but time dependent. Non-Newtonian fluids can be divided into three different fluids:

(1) Pseudoplastic fluids

When the strain rate increases, their viscosity decreases (see **Figure 3.8**)

(2) Dilatant fluids

When the strain rate increases, their viscosity also increases (see **Figure 3.8**)

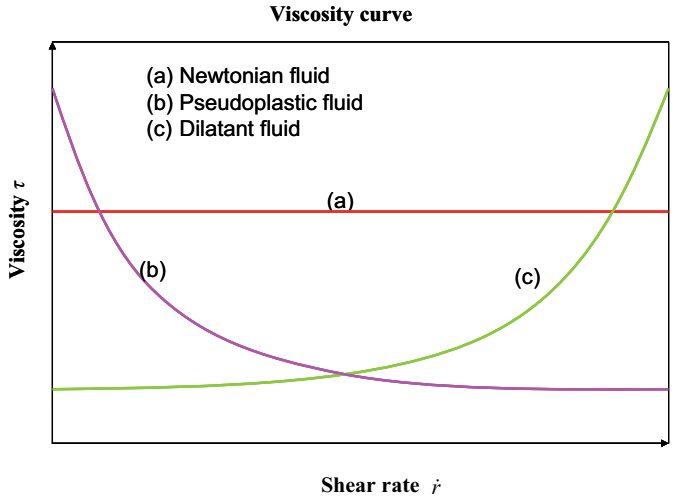

Figure 3.8 Viscosity curve of different kinds of fluids.

3.1.4 Particle size measurement

The particle size of MgH_2 THF suspension was measured by Horiba LB-550 (Retsch Technology GmbH, Haan, Germany). It uses scattered laser beam and the "Fourier-Transform/Iterative Deconvolution" technique to provide accurate results not only for average particle size, but also for distribution shape [73]. It can measure particle size over the range of 1nm-6000nm. Horiba's original optical design makes it possible to perform measurements over a wide range of concentrations, from the ppm level up to 40% solids.

The working principle of Horiba LB-550 is shown in **Figure 3.9**. The focal point of the laser beam is brought as close as possible to the inner wall of the cell. This suppresses the effects of multiple scattering in highly concentrated samples and still provides sufficient signal strength for lower concentration samples because the scattered light is not attenuated by passing through a large volume of the sample dispersion. The angle of irradiation into the cell is also carefully controlled, eliminating the effects of stray and reflected light. This increases the signal-to-noise ratio and the ability of the LB-550 to measure diluted samples.

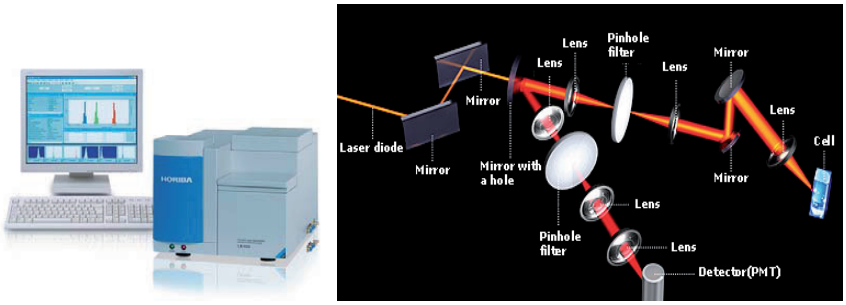

Figure 3.9 Schematic and working principle of Horiba LB-550

3.2 Powder production and characterization

3.2.1 Powder Production

The wet ball milled MgH_2 / $NaAlH_4$ suspensions were filtered and separated from the YSZ milling balls. Due to low boiling point of n-hexane and THF, they can easily evaporate. Then the evaporated MgH_2 / $NaAlH_4$ pieces were milled in a mortar to form nano-structured powder. In order to compare, the dry ball milled MgH_2 / $NaAlH_4$ powder with the same ball milling parameters was also produced. The dry ball milled MgH_2 / $NaAlH_4$ powder were also separated from YSZ milling balls by sieving. All these treatments were operated in a glovebox.

3.2.2 X-Ray Diffraction (XRD)

The phase composition and microstructure of the powders was analyzed by X-ray diffraction (XRD) with a Bruker D4 ENDEAVOUR diffractometer (Siemens AG, Germany) equipped with diffracted-beam monochromator for Cu-K_α. The crystallite size of MgH_2 powder was also measured based on its peak broadening using the Williamson-Hall method [74].

When an incident X-ray beam encounters a crystal lattice, it is generally scattered. Most scattering interferes with itself are eliminated (destructive interference). When certain geometric requirements are met, X-rays scattered from a crystalline solid can

constructively interfere, producing a diffracted beam. In 1912, W. L. Bragg recognized a predicatable relationship among several factors. Because each crystalline material has a characteristic atomic structure, it will diffract X-rays in a unique characteristic pattern. Bragg Law describes the relationship between the crystal structure and characterization of X-ray (see **Figure 3.10**):

$$2d \cdot \sin\theta = \lambda \qquad \textbf{(3.2)}$$

where d is the lattice interplanar spacing of the crystal, θ is X-ray incidence angle (Bragg angle) and λ is wavelength of the characteristic x-rays.

The X-ray diffractometer is an apparatus used to determine the angles at which diffraction occurs for powdered specimens; its features and working principle are represented schematically in **Figure 3. 11**. The powder specimen is located on a flate plate which is supported for rotation around the axis. This axis is perpendicular to the plane of the supported plate. The monochromatic X-ray beam is generated at a X-ray source in the tube and the intensities of diffracted beams are detected with a counter. The counter is mounted on a movable carriage, which rotates around the powder specimen according to the diffractometer circle. The angle which counter rotates is twice as much as that of supported plate rotates.

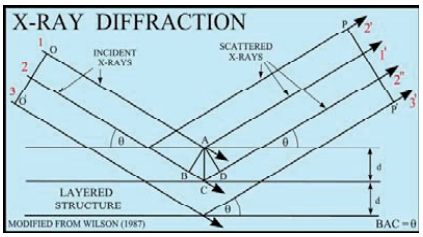

Figure 3.10 Schematic of X-ray diffraction.

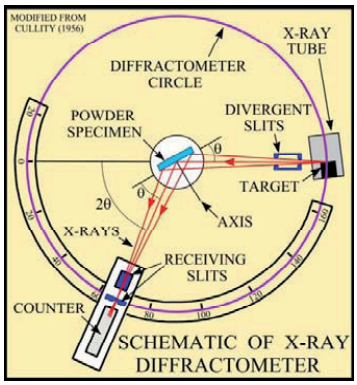

Figure 3. 11 Schematic of X-ray diffractometer.

3.2.3 Scanning Electron Microscopy (SEM)

Surfaces and morpholoy were imagined with a high local resolution by a scanning electron microscope (SEM) (Zeiss, Ultra55, Oberkochen, Germany) with an energy dispersive X-ray spectrometer (EDX) (Model Inca, Oxford Instruments, Oxfordshire, U.K.).

SEM stands for scanning electron microscope and is a microscope that uses electrons instead of light to generate an image.

3.2.4 Specific surface area measurement (BET measurement)

The specific surface area of the MgH_2 samples was determined using an Areameter II instrument (Ströhlein Instruments, Germany, see **Figure 3.12**). The test is based on the BET (Brunauer Emmet und Teller, 1938). The gas adsorption method is to measure the amount of gas adsorbed on the surface of a powder sample as a function of the pressure of the adsorbate gas, and is used to determine the specific surface area of a powder sample. Measurements are usually performed at the boiling point of liquid nitrogen (-196°C). When the gas is physically adsorbed by the powder sample, the following relationship holds when P/P_0 is in the range of 0.05 to 0.3 for pressure P of the adsorbate gas in equilibrium for the volume of gas adsorbed V_a.

$$\frac{1}{V_a(\frac{P_0}{P}-1)} = \frac{(C-1)}{V_m C} \times \frac{P}{P_0} + \frac{1}{V_m C} \quad \textbf{(3.3)}$$

P: Partial vapor pressure of adsorbate gas in equilibrium (kPa)

P_0: Saturated pressure of the adsorbate gas at -196°C (kPa)

V_a: Volume of gas adsorbed at equilibrium (mL)

V_m: Volume of gas adsorbed in monolayer (mL)

C: Dimensionless constant related to the enthalpy of adsorption and condensation of the adsorbate gas

The specific surface area S is determined from V_m, the volume of gas adsorbed in a monolayer on the sample.

$$S = \frac{V_m \times N \times a}{m \times 22400}$$

S : Specific surface area (m^2/g)

N : Avogadro constant

a : Effective cross-sectional area of one adsorbate molecule (m^2)

m : Mass of the test powder (g).

Area Meter II makes use of the dynamic flow method to measure the specific surface area of powder. In this method, a mixture of the adsorbate gas and a carrier gas is passed over a sample, and the volume of gas adsorbed is determined from the change in the concentration of the adsorbate gas in the mixture before and after the exposure to the powder sample. Nitrogen is typically used as the adsorbate gas, and a gas such as krypton is preferred for samples with a small specific surface area. Helium is generally used as the diluent gas.

Figure 3.12 Photo of Areameter II from Ströhlein Instrument.

3.3 Sorption test and characterization

Kinetic sorption measurements and P-C-T (Pressure-Composition-Temperature) isotherms of MgH_2 or $NaAlH_4$ powder were carried out using a volumetric Sievert

apparatus BELSORP-HP (BEL Japan, INC), which is an automatic high-pressure gas adsorption system.

Generally the sorption measurement can be operated based on both gravimetric method and volumetric method. The gravimetric method is relatively simple in terms of the measurement principle; however, in this method the sample is fixed in a balance and the equilibrium status of the microbalance is influenced by the desorbed/adsorbed gas pressure in the system and the sorption temperature. Thus, the gravimetric method requires a highly skilled technique for obtaining the sorption data accurately. As for the volumetric method, on the other hand, it reaches heat equilibrium quickly in the testing system. With this method, the volume of measurement system is measured precisely to determine the volume of sorption. Then, the volume of sorption is calculated from the gas pressure change in the measurement system, using the gas equation.

BELSORP-HP is a full automatic sorption measurement system, which adopts the volumetric method for the measurement. Highly reproducible data can be obtained by easy operation, using a precision diaphragm pressure sensor.

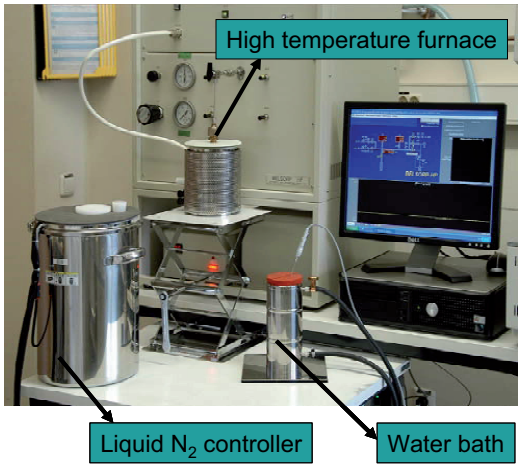

Figure 3.13 Photo of the BELSORP-HP instrument

BELSORP-HP has a wide temperature range from 77K up to 1073K with three different temperature controller (see **Figure 3.13**) and various kinds of adsorptives, e.g. H_2, CO_2, Ar, N_2, CH_4 and so on.

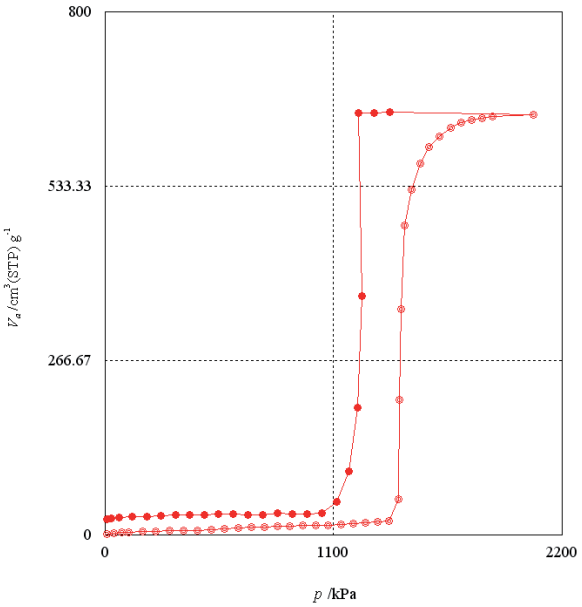

Figure 3.14 Example of an isothermal sorption measurement at 375°C of wet ball milled MgH_2 with 3wt%Nb_2O_5 powder.

Adsorption isotherms describe the relationship between the pressure and adsorption amount at a constant temperature. The horizontal axis indicates the equilibrium pressure P (see **Figure 3.14**). The adsorption amount in the vertical axis is commonly expressed as V/ml(STP)g^{-1}.

Chapter 4 Experimental results and discussion

4.1 Improvement of MgH_2 properties

4.1.1 Improvement of MgH_2 properties due to processing

4.1.1.1 Characteristics of MgH_2 suspension

As described in **Chapter 3.1.3**, both MgH_2 n-hexane and MgH_2 THF based suspension were produced. First of all four MgH_2 n-hexane suspensions (see **Table 3.1**) were compared in order to determine an optimal combination of milling parameters.

The difference of sample No.4-1 and No.4-2 was that MgH_2 mass percentage in the suspension. In sample No.4-2 and No.4-3 only ball-to-powder weight ratio (BPR) was different, which was 5:1 and 10:1, respectively. And ratio of YSZ grinding balls with 5mm and 2mm diameter in sample No.4-3 and No.4-4 differs from 7:3 to 1:1. Through the comparison between two different adjacent samples the influence of the variable milling parameters on the formed MgH_2 suspension could be attained. Thus the optimal combination of the three parameters was determined.

The particle size distribution of MgH_2 in n-hexane suspension was measured by Horiba LB-550 (see **Figure 3.9**). The comparison of No.4-1 and No.4-2 in **Figure 4.1** showed that the 20wt% MgH_2 n-hexane suspension had a smaller average particle size than the 50wt% MgH_2 suspension. With increased BPR ratio, the average particle size of MgH_2 decreased significantly (see No.4-2 and No.4-3 in **Figure 4.1**). Finer YSZ grinding balls (diameter = 2mm) produced relatively larger particle size of MgH_2 in n-hexane suspension due to less collision forces provided on the MgH_2 powder, which is obtained from the comparison of No.4-3 and No.4-4.

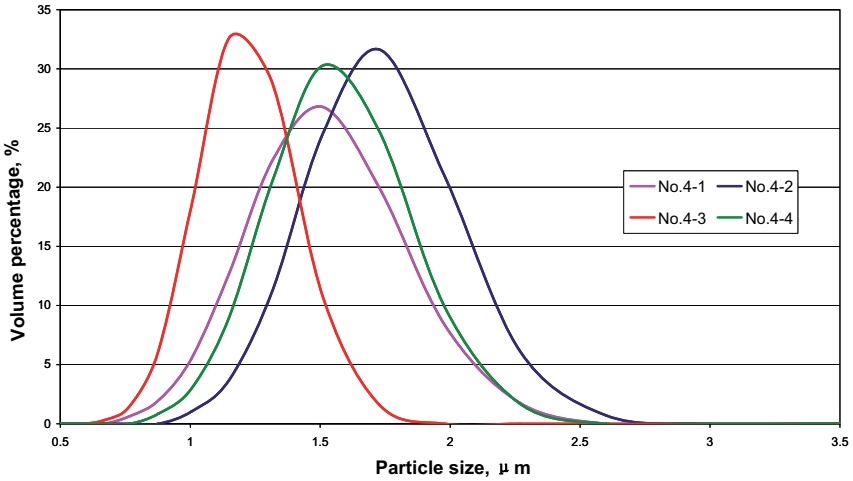

Figure 4.1 Particle size distribution of MgH_2 suspension with different milling parameters

Combining these results for the MgH_2 n-hexane suspension characteristics, in order to get the finer particle size of MgH_2 in the suspension the mass percentage of MgH_2 powder in the suspension is 20wt%, the BPR is 10:1 and YSZ grinding balls with diameter 5mm.

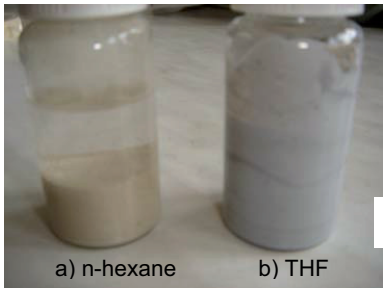

Figure 4.2 Comparison of MgH_2 a)n-hexane and b)THF suspension with 20wt% MgH_2 powder inside

It was found that all the ball milled n-hexane MgH_2 suspension was not stable. Its stability was achieved only within 10 min, afterwards most of the MgH_2 particles [illegible] bottom of the container. Two obvious layers were formed in the suspension independent on ball milling parameters, the upper layer is mainly n-hexane solvent and the down layer is mainly MgH_2 powder (**Figure 4.2a**). Thus a respective viscosity value for the MgH_2 n-hexane suspension was difficult to measure.

In order to improve the characteristics of MgH_2 suspension, the solvent was changed to THF with different mass percentage of MgH_2 inside, i.e. 20wt%, 30wt%

and 40wt%. BPR of 10:1 was used for milling of MgH_2 THF suspensions. The grinding balls were 5mm diameter YSZ balls and milling time was still 72h.

With ball milling, stable MgH_2 THF suspensions could be produced. Even one week after ball milling, the MgH_2 THF suspensions were still homogeneous and stable (**Figure 4.2b**). The viscosity of the MgH_2 THF suspensions with different MgH_2 mass percentage was measured by Physica Rheometer MCR100 (see **Figure 3.7**).

Pure THF as a reference showed Newtonian behavior, i.e. its viscosity (quotient between shear stress of suspension and its shear rate) does not change with its shear rate but remained almost constant (see **Figure 3.8a**). The viscosity of the suspension increased with solid loading. All suspensions exhibited pseudoplastic behavior, i.e. the viscosity decreased with an increasing shear rate, especially for high mass percentages of MgH_2 powder inside the MgH_2 THF suspension. It is shown in **Figure 4.3** that the viscosity of the THF suspension with 30 wt% MgH_2 was 10 times higher than that of the THF suspension with 20 wt% MgH_2. When the MgH_2 mass percentage increased from 30 wt% to 40 wt%, its viscosity enhanced to about 10^5~10^6 times as the former. However, due to low flowability of the THF suspension with more than 40 wt% MgH_2, its viscosity could not be accurately measured. The THF has not only an advantages effect on the stabilization; it also leads to finer particle sizes compared to n-hexane. This is shown through the comparison of the MgH_2 n-hexane and MgH_2 THF suspension both with 20wt% MgH_2 powder in **Figure 4.4**.

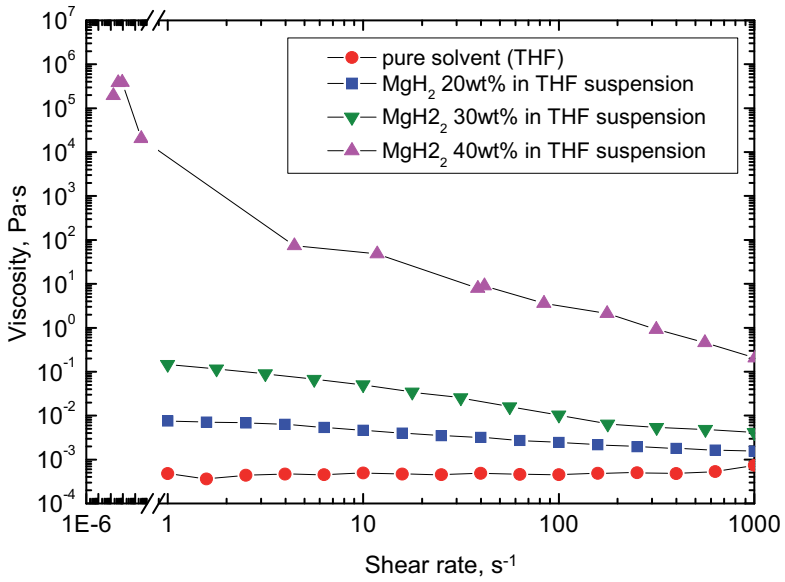

Figure 4.3 Viscosity of (a) pure THF, MgH_2-THF suspension with (b) 20wt% MgH_2, (c) 30wt% MgH_2 and (d) 40wt% MgH_2 powder, respectively.

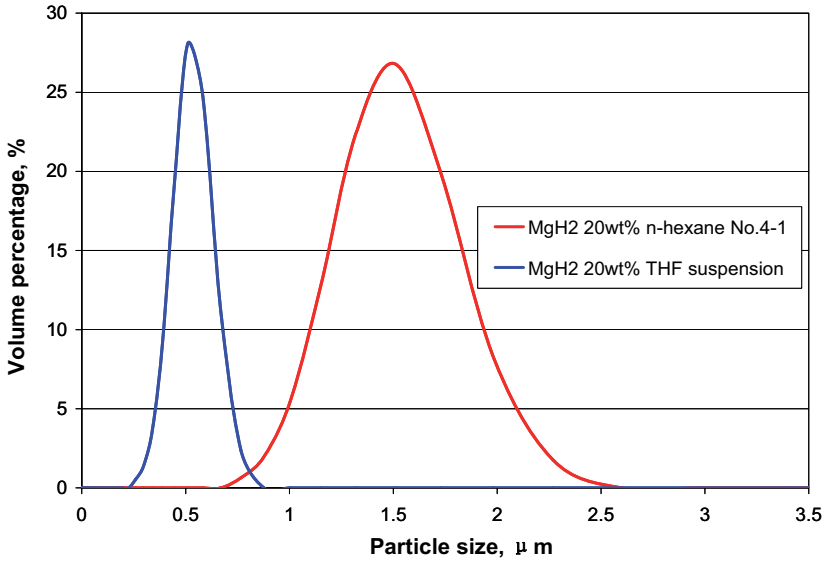

Figure 4.4 Particle size comparison of MgH_2 n-hexane suspension and MgH_2 THF suspension.

Although the MgH_2 THF suspension is not the final hydrogen storage material, this by-product can be suitable for an industrial application. By dip coating substrates

in the MgH_2 THF suspension, a nano-structured MgH_2 coating can be obtained. With 20wt% MgH_2 THF suspension, a single layer of MgH_2 coating on the porous Al_2O_3 substrate was produced (**Figure 4.5**), which was a porous and nano-structured MgH_2 coating.

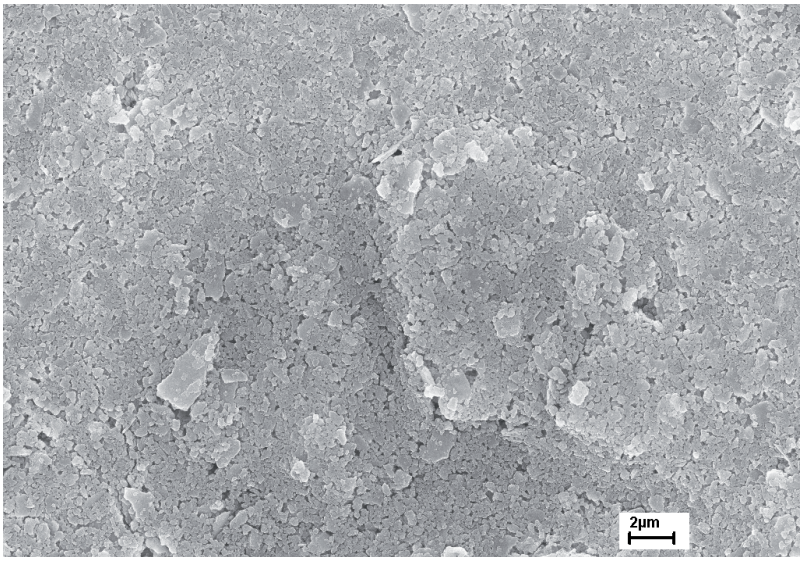

Figure 4.5 SEM image of nano-structured MgH_2 coating on porous Al_2O_3 substrate

4.1.1.2 Characteristics of MgH_2 powder

The wet ball milled MgH_2 powder was produced from the wet ball milled 20wt% MgH_2 THF suspension based on the method given in **Chapter 3.2.1**. The dry ball milled MgH_2 powder was also produced with the same ball milling parameters as mentioned in **Chapter 3.2.1**.

Figure 4.6 show SEM micrographs of as-received, dry ball milled and wet ball milled MgH_2 powder in order to compare their microstructures. The particle size of the as-received MgH_2 powder ranged from 20~100 μm with different kinds of shapes (see **Figure 4.6a**) and its specific surface area was ~6.2 m^2/g measured by BET. After dry ball milling, the particle size was much finer than that of as-received MgH_2 powder, ranging from 0.5~4μm, as can be seen in **Figure 4.6b**. The dry ball milled MgH_2 particles had a mainly spherical morphology and the fine particles

agglomerated together with a relatively dense surface (~16.4 m^2/g measured by BET). Compared to **Figure 4.6b**, the particle size of wet ball milled MgH_2 powder was much smaller (ranging from 30 to 500 nm) than that of as-received and dry ball milled MgH_2 powder. In addition, wet ball milled MgH_2 particles did not have a spherical morphology but rather a polyhedron morphology. After evaporation of the THF, the wet ball milled MgH_2 nanocrystalline particles formed big porous agglomerates. **Figure 4.6c** shows larger magnification in addition. The agglomerate had a very low packing density because of their surface roughness and the electrostatic repulsion of the wet ball milled MgH_2 particle surface. In addition, due to the lubrication of the THF solvent during wet ball milling, MgH_2 particles exhibited a lower re-welding force compared to the dry ball milling case. BET measurements showed a specific surface area of 75.5 m^2/g for the wet ball milled MgH_2 powder, which is about 7 times larger than that of dry ball milled MgH_2 powder due to a considerable decrease in particle size and also due to a porous open particle surface as a result of the evaporation of THF solvent.

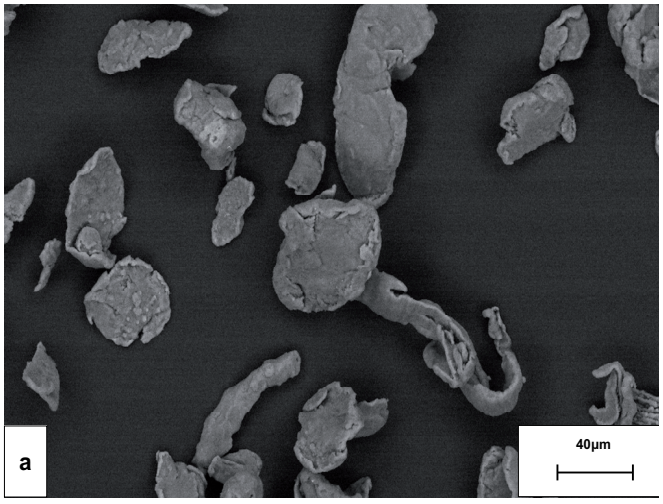

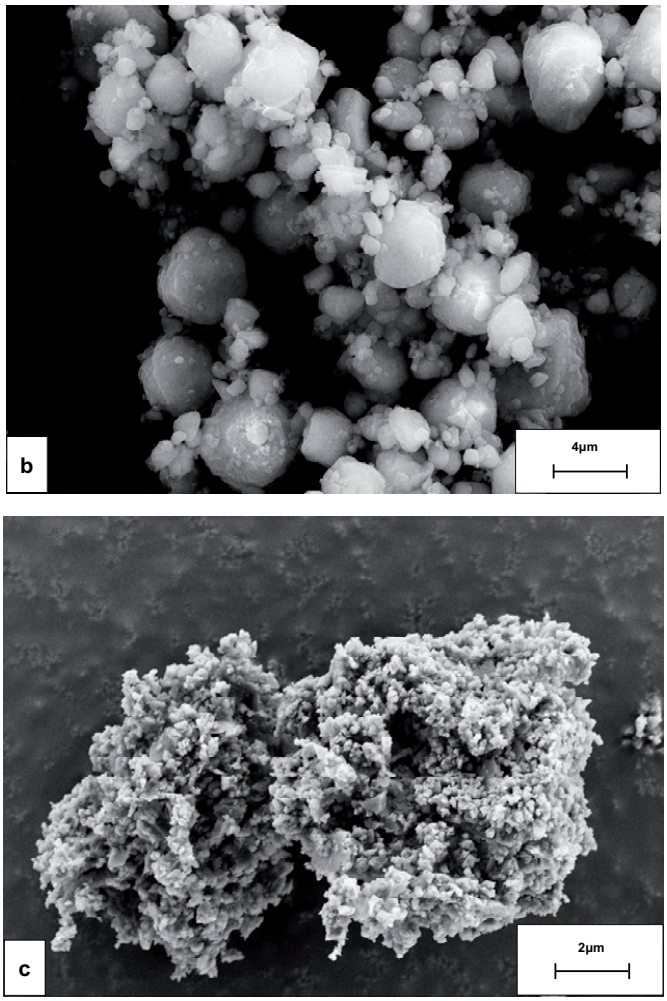

Figure 4.6 SEM images of (a) as-received MgH_2, (b) dry ball milled MgH_2 and (c) wet ball milled MgH_2 powder.

XRD patterns of the nanocomposite dry and wet ball milled MgH_2 powder as well as as-received MgH_2 powder are shown in

Figure 4.7. The positions of their XRD patterns indicate that the main phase of dry and wet ball milled MgH_2 powder is the same as that of as-received MgH_2 powder, i.e. tetragonal β-MgH_2 phase. However, in addition the metastable orthorhombic γ-MgH_2 phase appeared in both dry and wet ball milled MgH_2 powder, but not in as-received MgH_2 powder. The metastable γ-MgH_2 phase is a high-pressure polymorphic form of

the β-MgH_2 phase [75] and is commonly observed to appear after ball milling of MgH_2 [76]. The high pressure required to transform β-MgH_2 into γ-MgH_2 is provided during ball milling through the localized on-contact impacting action of milling balls on the MgH_2 powder particles in the milling vial. After both dry and wet ball milling, the peak broadening of the β-MgH_2 phase was very obvious due to a large decrease in grain size. Based on the Bragg reflection equation, it is possible to evaluate the grain sizes from the line broadening [77]. The mean grain size of as-received, wet ball milled and dry ball milled MgH_2 powder determined by calculating the XRD line broadening were found to be 120 nm, 31 nm and 7 nm, respectively. Thus from the XRD patterns and SEM analysis it can be concluded that with the same ball milling parameters, wet ball milled MgH_2 powder had a much smaller average particle size but a larger average grain size than those of the dry ball milled MgH_2 powder. From the comparison of their desorption/absorption and cycling behavior the question can be discussed whether particle size or grain size has more pronounced influence on hydrogen sorption and what kind of microstructure is favorable for the hydrogen sorption of MgH_2.

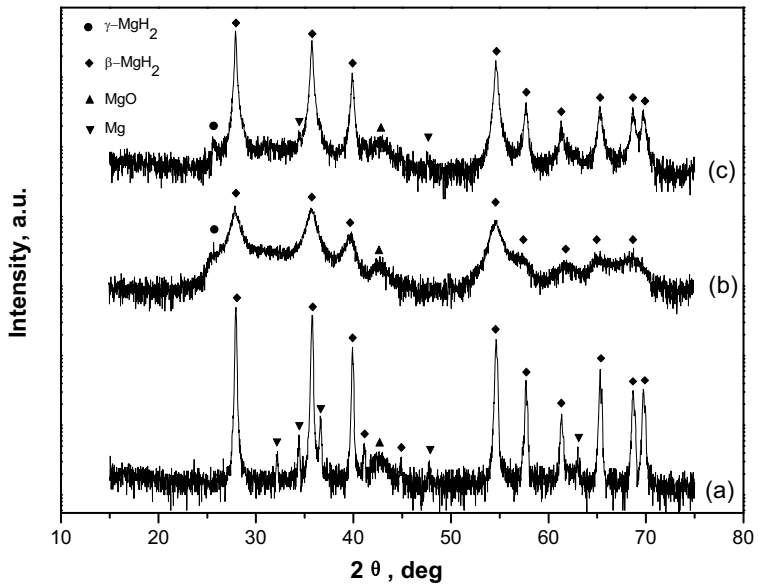

Figure 4.7 X-ray powder diffraction pattern (CuK_α radiation) of (a) as-received MgH_2, (b) dry ball milled MgH_2 and (c) wet ball milled MgH_2 powder.

4.1.1.3 Sorption behaviour of MgH_2 powder

Isothermal kinetic sorption measurements were carried out using a volumetric Sievert apparatus which was introduced in **Chapter 3.3**. The desorbed/absorbed hydrogen amount in the following section is calculated based on the assumption of pure MgH_2. **Figure 4.8** shows isothermal desorption of as-received, dry ball milled and wet ball milled MgH_2 powder at 450, 400, 350, 300 °C, respectively, and 250 °C only for wet ball milled MgH_2 powder in an initial vacuum atmosphere (~0.1 Pa). Before desorption measurements were performed, all three samples were pre-heated at 100 °C under a vacuum (~0.1Pa) for 2 h. At both 400 °C and 450 °C, the desorption kinetics and desorbed hydrogen capacity of as-received, dry ball milled and wet ball milled MgH_2 powder were found to be very similar, because at both temperatures, all three kinds of MgH_2 powder were partly melted and then desorbed (see **Figure 4.9**). At 350 °C, as-received MgH_2 powder showed almost no hydrogen desorption in 100 min, while dry ball milled MgH_2 powder desorbed 1.4 wt% hydrogen and wet ball milled MgH_2 powder desorbed 7.0 wt% in the same period. At 300 °C both as-received and dry ball milled MgH_2 powder showed very little hydrogen desorption, however, wet ball milled MgH_2 powder desorbed 2.3 wt% hydrogen in 100 min. Even at 250 °C wet ball milled MgH_2 desorbed 1 wt% hydrogen after 100 min.

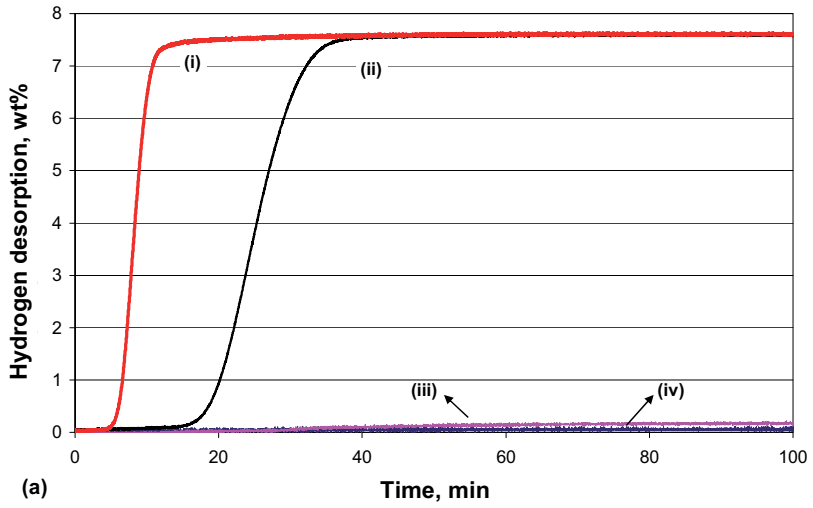

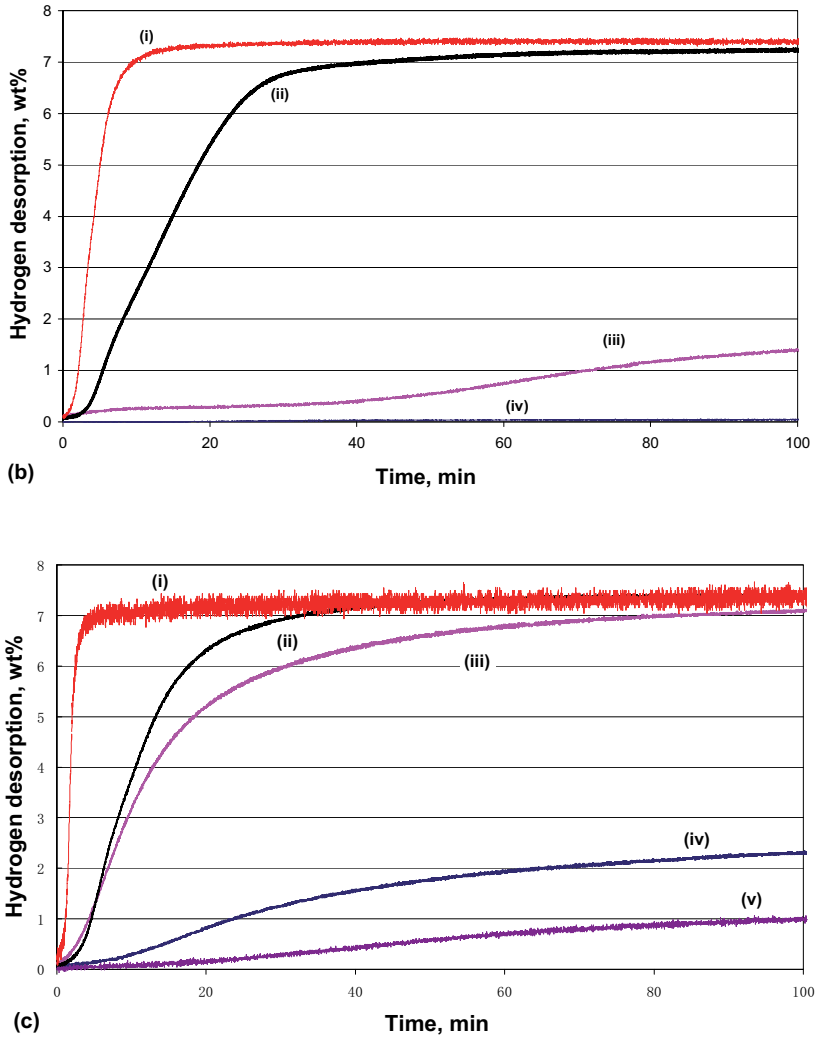

Figure 4.8 Desorption behaviour of (a) as-received, (b) dry ball milled and (c) wet ball milled MgH_2 powder at (i)450°C, (ii)400°C, (iii)350°C, (iv)300°C and (v)250°C with an initial vacuum (~0.1Pa) atmosphere.

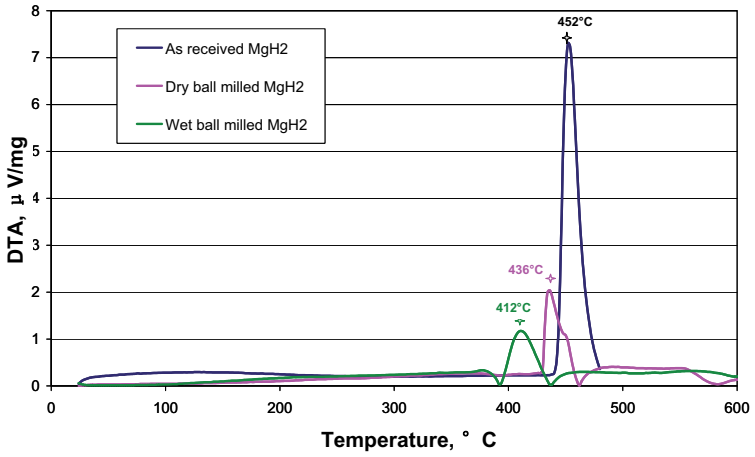

Figure 4.9 DTA curves of as-received, dry ball milled and wet ball milled MgH_2 powder

In addition a hydrogen desorption experiment with a temperature increasing rate of $0.33Kmin^{-1}$ in the temperature range of 40°C~450°C was made for as-received, dry ball milled and wet ball milled MgH_2 powder in order to compare their desorption starting temperature. **Figure 4.10** shows that as-received MgH_2 powder started to desorb hydrogen significantly from 380°C on, while the starting desorption temperature for dry ball milled MgH_2 powder was about 320°C and that for wet ball milled MgH_2 powder was much lower, about 250°C. The wet ball milled MgH_2 powder started to desorb hydrogen much earlier than the other powders and the desorbed hydrogen amount at the same desorption temperature and desorption time was much larger than others.

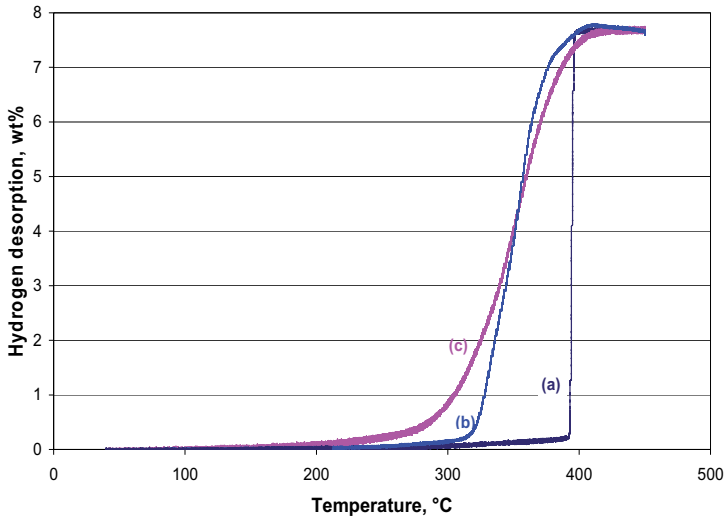

Figure 4.10 Hydrogen desorption plots of (a) as-received, (b) dry ball milled and (c) wet ball milled MgH_2 powder with temperature increasing speed of 0.33°C/min in the temperature range from 40~450°C.

In order to compare the influence of wet ball milling and dry ball milling on the hydrogen absorption, both dry ball milled and wet ball milled MgH_2 powders were first then pre-heated at 100 °C for 2 h in a vacuum atmosphere (~0.1 Pa). Dry ball milled MgH_2 powder was desorbed at 350 °C for 24 h and the desorbed hydrogen amount was 5.3 wt%. However, full desorption equilibrium was not reached in this time. In comparison, wet ball milled MgH_2 powder was also desorbed at 350 °C for 3 h and the desorbed hydrogen amount almost reached the theoretical maximal value of 7.6 wt%. Absorption experiments were then performed on both samples at 300 °C, 250 °C, 200 °C, 150 °C and 100 °C (**Figure 4.11**) with an initial hydrogen pressure of 1.2 MPa. Dry ball milled MgH_2 powder did not exhibit obvious absorption behavior below 200 °C, while wet ball milled MgH_2 powder absorbed considerable amounts even at 100 °C. The improved absorption behaviour of the wet ball milled MgH_2 powder is also shown in **Figure 4.12**, the absorbed hydrogen amount after 1 h of absorption.

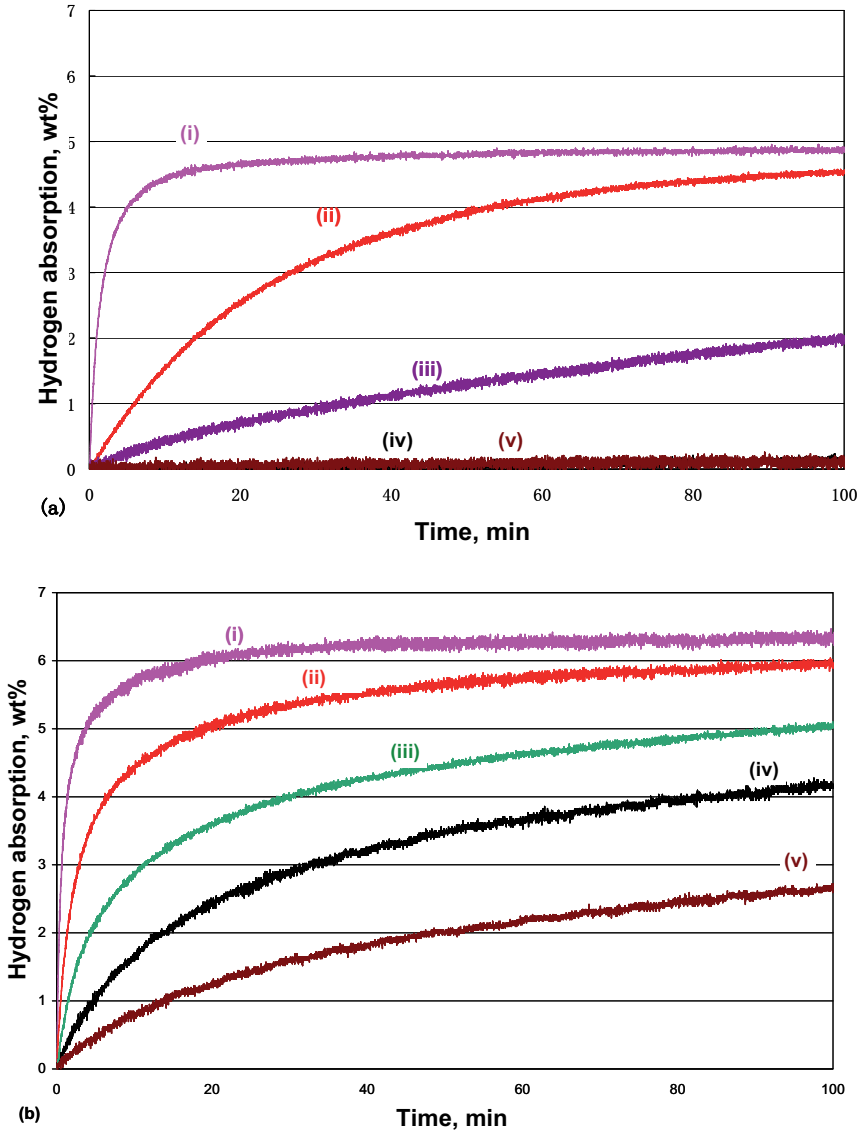

Figure 4.11. Hydrogen absorption of (a) dry ball milled and (b) wet ball milled MgH_2 powder at (i)300°C, (ii)250°C, (iii)200°C, (iv)150°C and (v)100°C with an initial hydrogen pressure of 12 bar

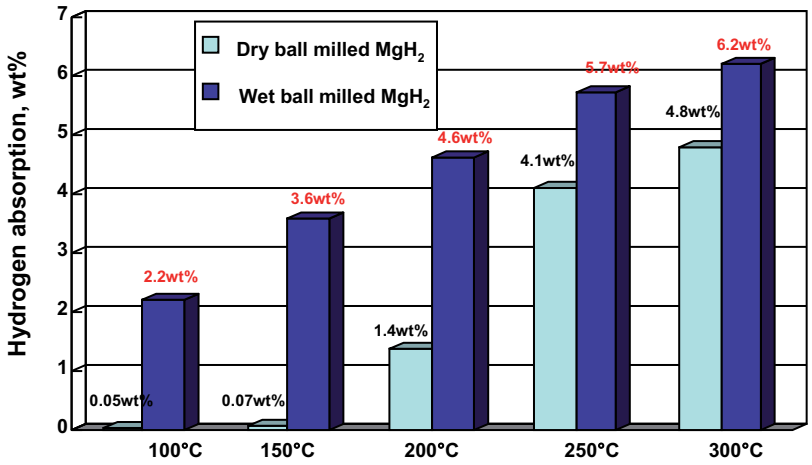

Figure 4.12. Comparison of dry ball milled and wet ball milled MgH_2 powder after 1h absorption behaviour with an initial hydrogen pressure of 12bar.

4.1.1.4 Cyclic sorption behaviour of MgH_2 powder

Cyclic desorption and absorption behavior of nanocrystalline MgH_2 powder are key properties for an industrial application. Before the cycling tests, wet ball milled MgH_2 powder was first pre-heated at 100 °C for 2 h in a vacuum atmosphere (~0.1 Pa). Its hydrogen was then desorbed at 350 °C in a vacuum atmosphere for 10 h. After full desorption procedure, the remaining powder was cooled down to 150 °C for an absorption with an initial hydrogen pressure of 1.2 MPa for 100 min. Further cyclic testing was performed on the basis of the same procedure. **Figure 4.13** shows that the cyclic desorption kinetics of wet ball milled MgH_2 powder improved considerably from the 1st to 5th cycle at the expense of the amount of desorbed hydrogen, i.e. the desorbed hydrogen amount of wet ball milled MgH_2 powder after 1 h decreased from 6.35 wt% in the 1st cycle to 5.94 wt% in the 5th cycle. However, from the 5th to 10th cycle, hydrogen desorption showed almost no attenuation and it maintained the improved fast kinetics. Thus, the hydrogen desorption kinetic was improved by cyclic sorption but with only few loss of hydrogen capacity.

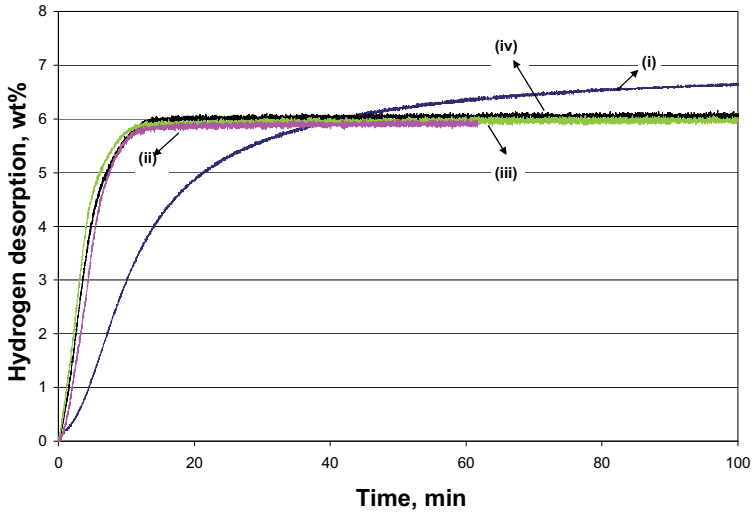

Figure 4.13 Cyclic desorption behavior of wet ball milled MgH_2 powder at (i) 1st, (ii) 5th, (iii) 8th and (iv) 10th cycle in an initial vacuum (~0.1Pa) atmosphere at 350°C.

Figure 4. 14 shows the cyclic absorption behavior of wet ball milled MgH_2 powder at 150 °C with an initial hydrogen pressure of 1.2 MPa. From the 1st to 10th cycle, both hydrogen absorption kinetics and the amount of absorbed hydrogen improved significantly. At 1 h of hydrogen absorption, the amount of absorbed hydrogen of wet ball milled MgH_2 powder increased from 3.16 wt% in the 1st cycle to 3.69 wt% in the 5th cycle, to 4.85 wt% in the 8th cycle and 5.68 wt% in the 10th cycle. Although the amount of absorbed hydrogen of wet ball milled MgH_2 powder up to equilibrium at the 5th, 8th and 10th cycle is nearly the same, i.e. 6.0 wt%, the time to equilibrium decreased from the 5th cycle to the 8th and 10th cycle. It is shown that after 10 cycles of desorption/absorption wet ball milled MgH_2 powder can absorb at least 4.8 wt% hydrogen in 20 min at 150 °C with an initial hydrogen pressure of 1.2 MPa. For comparison a cycling test of as-received MgH_2 powder was also performed. Due to quite low desorption behavior of as-received MgH_2 powder at 350°C (see **Figure 4.9a**), the cyclic desorption of as-received MgH_2 powder was made at 400°C with an initial vacuum (~0.1 Pa) atmosphere and the cyclic adsorption was performed at 150°C with an initial hydrogen pressure of 1.2 MPa. In the 1st cyclic desorption, it

showed the same desorption behavior as shown in **Figure 4.9a**, but it had nearly no absorption behavior in the 1st cyclic absorption and thus no further desorption and absorption took place in the following cycles.

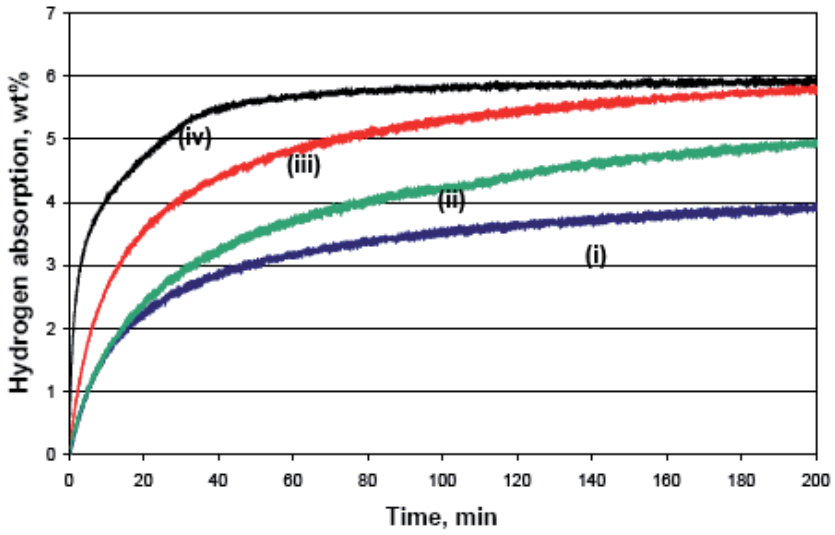

Figure 4. 14. Cyclic absorption behaviour of wet ball milled MgH_2 powder at (i) 1st, (ii) 5th, (iii) 8th and (iv) 10th cycle with an initial hydrogen pressure of 1.2 MPa at 150°C.

The significantly improved hydrogen cycling properties of wet ball milled MgH_2 powder can be mainly ascribed to the much finer particle size and larger porous surface due to wet ball milling. These dispersed nanosized wet ball milled MgH_2 particles result in a greatly enhanced reduction in hydrogen diffusion path lengths and also promoted the surface reaction of hydrogen atoms. Our modeling results will indicate that the improved surface reaction is the main reason.

Compared to dry ball milled MgH_2 powder, wet ball milled MgH_2 powder has an average finer particle size but an average larger grain size. However, it should be noted that the average particle size and grain size of dry ball milled and wet ball milled MgH_2 powder are much finer than those of as-received MgH_2 powder. The improved hydrogen desorption/absorption behavior of wet ball milled MgH_2 powder compared to dry ball milled MgH_2 powder, leads us to conclude that the reduction in

MgH_2 particle size has more influence on hydrogen sorption properties than a decrease in grain size.

4.1.1.5 P-C-T curves and Van't Hoff plot

In this work thermodynamic properties of MgH_2 powder were determined accurately by the volumetric method using a Sievert's apparatus. A typical isotherm of a reversible metal hydride is shown in **Chapter 2.2.2 Figure 2.3.**

This experiment started with hydrogen absorption. Thus wet ball milled MgH_2 powder was first desorbed at 350°C for 5h with an initial vacuum atmosphere in order to desorb all hydrogen inside. In order to investigate the thermodynamic change due to wet ball milling, the same experiment was made for as-received MgH_2 powder but a desorption performed at 400°C was also operated.

Figure 4.15 shows P-C-T curves and the corresponding van't Hoff plots of the absorption process of as-received and wet ball milled MgH_2 powder. At the beginning for low hydrogen pressure, only the α-phase, i.e. hydrogen atoms dissolved inside the Mg matrix, exists. Before β-phase, i.e. the Mg hydride appeared, the hydrogen pressure always increases with hydrogen content. When the hydrogen pressure reaches a certain equilibrium, Mg hydride starts to form two phases, which are existing. From this point on, the fraction of Mg hydride grows while the Mg matrix disappears. The hydrogen pressure keeps its equilibrium value with increasing hydrogen content within the maximal hydrogen storage capacity. At higher isothermal temperature the plateau pressure was also higher for both as-received and wet ball milled MgH_2 powder corresponding to **equation 2.2**. During hydrogen absorption process more hydrogen amount can be absorbed by wet ball milled MgH_2 powder than by as-received MgH_2 powder. After formation of pressure plateau, a larger pressure increase was accompanied by an increase of hydrogen content in the Mg and Mg hydride matrix.

From the slope of the van't Hoff plot based on the P-C-T plateaus, the formation enthalpy for as-received MgH_2 powder and wet ball milled MgH_2 powder were calculated as 72.7 $kJ \cdot mol^{-1}H_2$ and 74.12 $kJ \cdot mol^{-1}H_2$, which are very close to the standard data of MgH_2 powder 74.5 $kJ \cdot mol^{-1}H_2$ [43]. This allows the conclusion that the enhanced hydrogen sorption of wet ball milled MgH_2 powder is the result of improved kinetics and not a change in the formation enthalpy. The entropy of wet ball milled MgH_2 powder determined from the intercept of van't Hoff plot is about 135.9 $J/(molH_2 \cdot K)$ which is also in accordance with the literature value of 130.7 $J/(molH_2 \cdot K)$ [43].

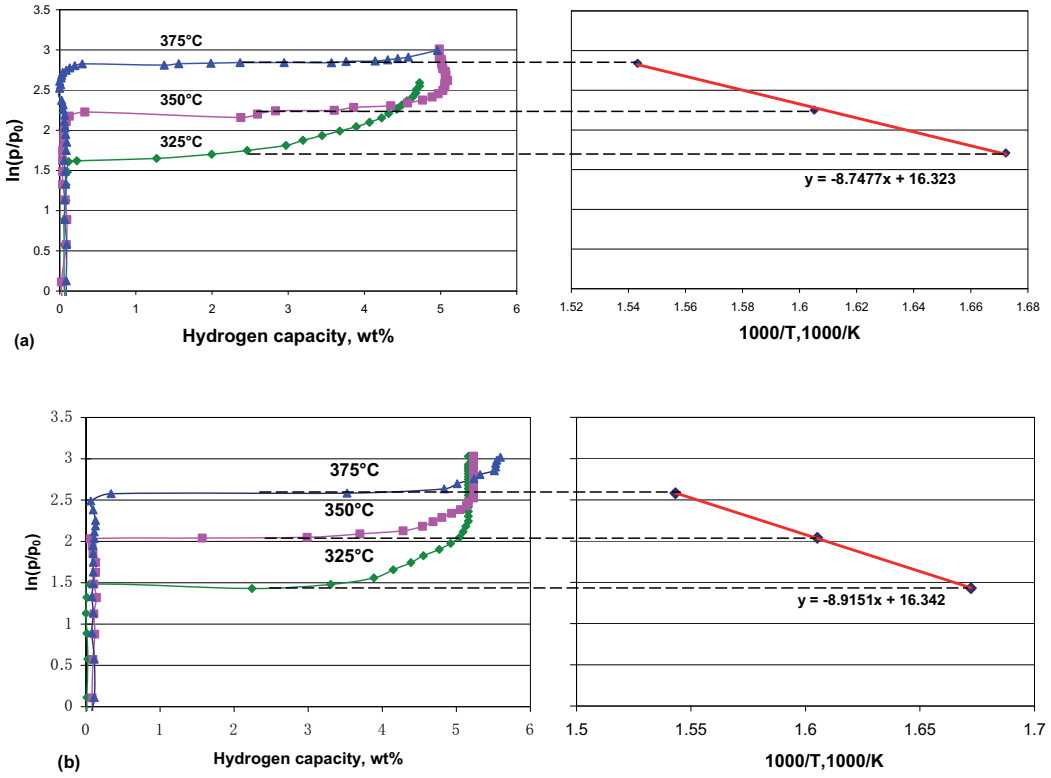

Figure 4. 15 P-C-T curves of (a) as received MgH_2 powder and (b) wet ball milled MgH_2 powder during absorption at different temperatures (left) and the corresponding van't Hoff plot (right) (see equation 2.2).

4.1.2 Improvement of MgH_2 properties due to catalysts

In order to improve the kinetics of Mg hydride, a series of binary and ternary Mg alloys have been studied. In 1960s, Reilly and Wiswall found that the MgH_2 decomposition temperature in alloys could be lowered by transition metal alloying through investigation of Mg_2Ni and Mg_2Cu [78]. In the 1970s, Tanguy et al. [79] found that the $LaNi_5$ and Pd ball milled with MgH_2 could obviously improve its kinetics. Liang et al. [39] found that the 3d-elements, Ti, V, Mn, Fe and Ni could improve the desorption/absorption kinetics of Mg and indicated that the 3d transition metals acted as catalysts, chemisorbing hydrogen and transferring it to the Mg matrix. Liang et al. also found that the mechanical milling of MgH_2-V led to the formation of a new composite, which can desorb hydrogen at low temperatures. This behaviour was considered to be a catalytic effect of vanadium by the particular microstructure of the composite [80].

As stated in **Chapter 4.1.1**, high energy ball milling produced nanoscaled MgH_2 powder with a large specific surface area, which favours dissociation of hydrogen atoms by offering a large number of dissociation sites allowing fast diffusion to the center of the particles due to the fine particle size. By combining this approach with a catalyst, a significant improvement in the kinetics can be made by allowing electron transfer and hydrogen dissociation through a mechanism called spillover [81] in which hydrogen molecules dissociate on the catalyst surface.

In this work, three different catalysts niobium ethoxide, vanadium and single-wall carbon nanotubes were wet ball milled with MgH_2 powder in order to improve its microstructure and further sorption behaviour.

4.1.2.1 Microstructure modification of wet ball milled MgH_2 with catalysts

The production of wet ball milled MgH_2 with catalysts powders was introduced in **Chapters 3.1.3** and **3.2.1**. **Figure 4.16** shows the XRD patterns of wet ball milled MgH_2 with 1wt% and 3wt% single-wall carbon nanotubes (CNTs) compared to as-received and wet ball milled CNTs. After wet ball milling of MgH_2 and CNTs

together, no obvious CNTs patterns could be realized. Possible explanations are: (1) too low amount of CNTs in the MgH_2 powder; (2) its microstructure was damaged by the collision with MgH_2 powder but not by YSZ balls (see **Figure 4.15(b)** which shows the patterns of CNTs even after wet ball milling).

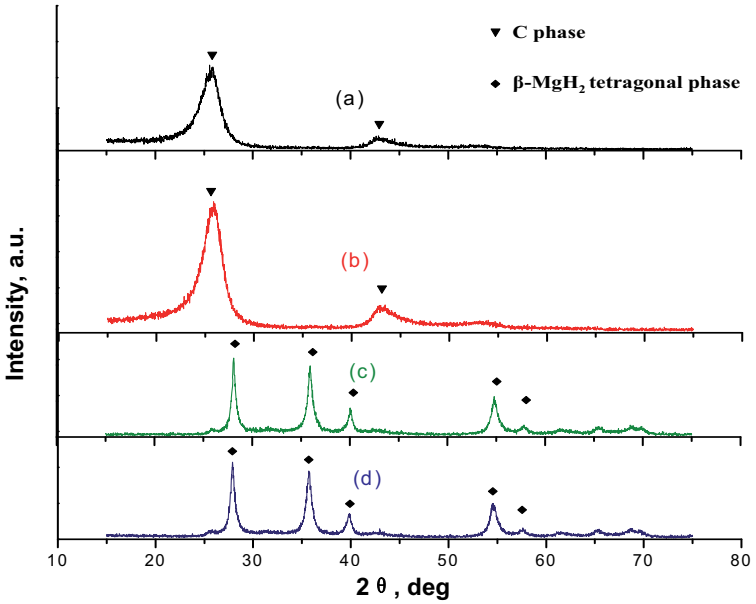

Figure 4.16 XRD patterns of (a) pure as-received CNTs; (b) wet ball milled CNTs; (c) wet ball milled MgH_2+1wt%CNTs; (d) wet ball milled MgH_2+3wt%CNTs powder.

In order to explain what happened to the CNTs during wet ball milling with the MgH_2 powder, the morphology of as-received CNTs, wet ball milled CNTs and wet ball milled MgH_2 powder with 1mol% CNTs was analysed (see **Figure 4.17**). Before wet ball milling CNTs are long curved tubes. After ball milling alone for 72h with the same milling parameters, the tubes were significantly shortened and compressed together to form big ends. However, when CNTs were ball milled with MgH_2 powder, nearly no more tube morphology was found in the wet ball milled MgH_2 with CNTs powder (in **Figure 4.17c** the red cycle shows a remaining single carbon nanotube). Obviously, the microstructure of CNTs was damaged by the collision between MgH_2 powder during wet ball milling.

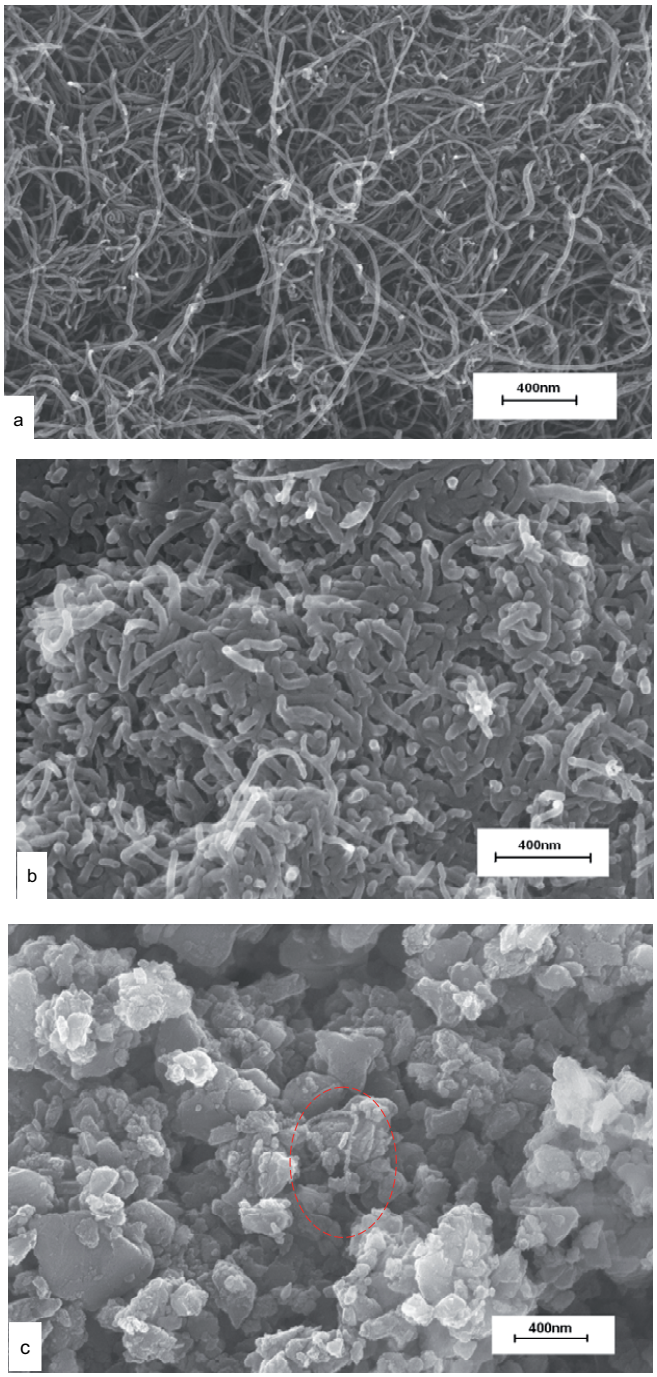

Figure 4.17 SEM images of (a) as-received CNTs, (b) wet ball milled CNTs and (c) wet ball milled MgH_2 powder with 1mol%CNTs.

The morphology of wet ball milled MgH_2 with 1mol% Nb_2O_5 is shown in **Figure 4.18** as well as its EDX composition analysis. It is obvious that the bright points which are located on the top surface contain more Nb than the dark points. Thus it can be concluded that the nanoscaled Nb_2O_5 particles were dispersed on the surface of MgH_2 agglomerates during wet ball milling.

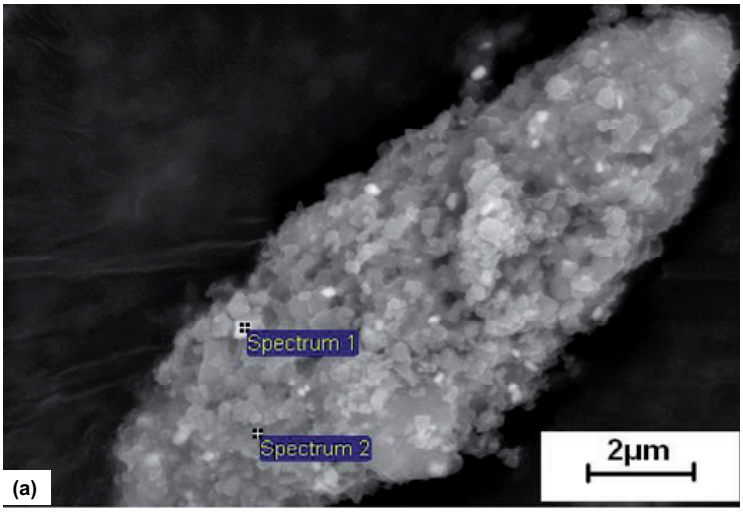

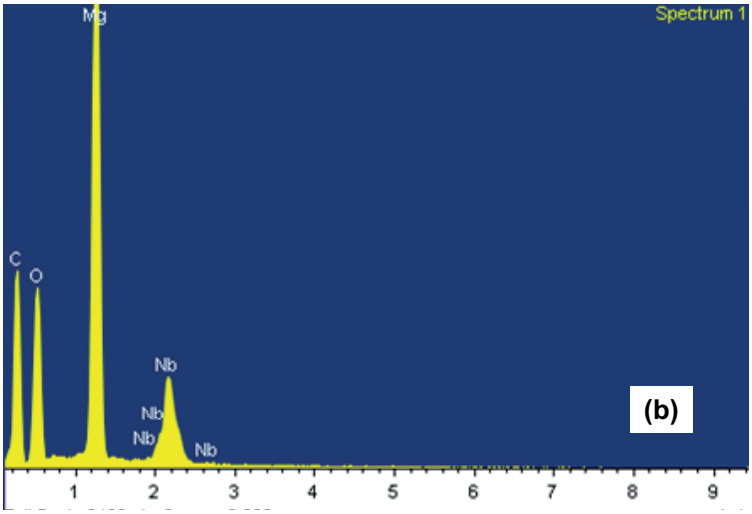

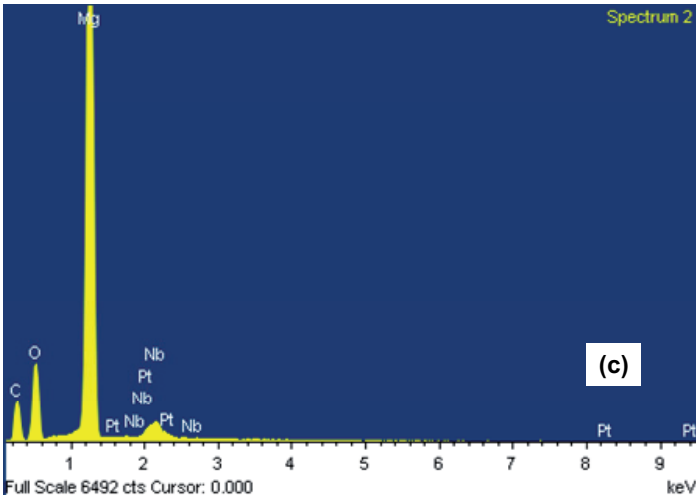

Figure 4.18 (a) SEM image of wet ball milled MgH_2 powder with 1mol%Nb_2O_5, and corresponding EDX analysis of (b) bright point 1 and (c) dark point 2.

In order to compare the influence of the catalysts on the hydrogen sorption and cycling behavior of wet ball milled MgH_2 powder, the weight of all three catalysts was 3wt%. **Figure 4.19** shows the comparison of XRD patterns of wet ball milled MgH_2 powder with different catalysts and without catalyst.

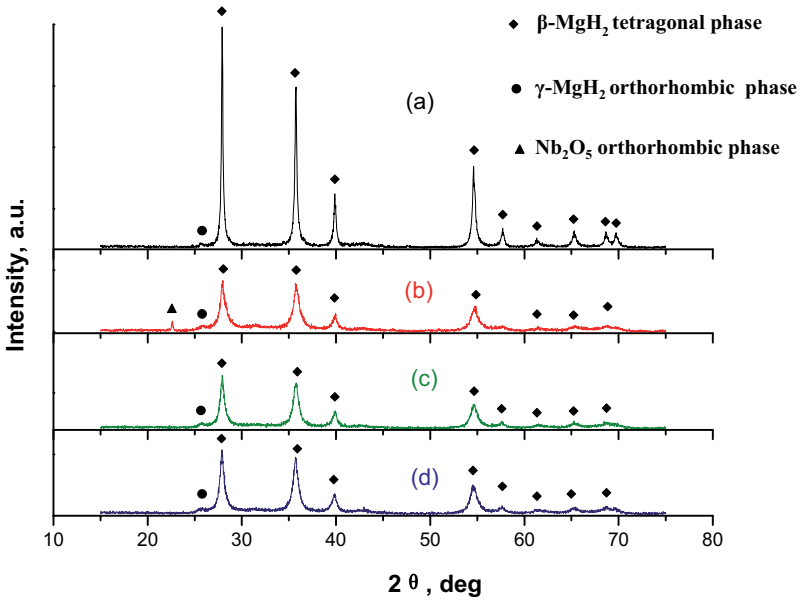

Figure 4.19 XRD patterns of wet ball milled MgH_2 powder (a) without catalyst; (b) with 3wt%Nb_2O_5; (c) with 3wt%V and (d) with 3wt%CNTs.

Compared to wet ball milled MgH_2 powder without catalysts, it is obvious that the wet ball milled MgH_2 powder with catalysts kept the main microstructure of the as-received MgH_2 powder, i.e. β-MgH_2 tetragonal structure and a minor γ-MgH_2 phase. Only wet ball milled MgH_2 powder with 3wt% Nb_2O_5 showed Nb_2O_5 orthorhombic structure. The other XRD patterns of the two kinds of MgH_2 with catalysts powder did not show any indication of the catalysts. Compared to wet ball milled MgH_2 powder without catalysts, the peaks of the XRD patterns of wet ball milled MgH_2 powder with catalysts are much broader. The grain size of wet ball milled MgH_2 powders with catalysts was also measured based on its peak broadening using the Williamson-Hall method [82]. The mean grain size of wet ball milled MgH_2 with 3wt%Nb_2O_5, 3wt%V and 3wt%CNT were 13 nm, 14 nm and 14 nm, respectively, which were much smaller than that of wet ball milled MgH_2 without catalysts 31 nm. However, their specific surface areas are similar to that of wet ball milled MgH_2 powder without catalysts. The specific surface area of wet ball milled MgH_2 powder with 3wt%Nb_2O_5, 3wt%V and 3wt%CNT were measured by BET gave 78.8m^2/g,

79.4m^2/g, and 73.7m^2/g, respectively (that of wet ball milled MgH_2 powder without catalysts was 75.5m^2/g).

4.1.2.3 Improvement of sorption behaviour due to catalysts

With catalysts the wet ball milled MgH_2 powder showed a much finer grain size but its particle size and specific surface area remained similar to values of the wet ball milled MgH_2 without catalysts (see **Table 4.1**). The influence of the microstructure and of the type of selected catalysts (metal oxide catalyst, transition metal catalyst and non metal catalyst) will be investigated in the following.

Table 4.1 Summary of grain size, particle size and specific surface area of different MgH_2 powder in this work

Powder	Grain size (nm)	Particle size (nm)	Specific surface area (m^2/g)
As-received MgH_2	120	20000-100000	6.2
Dry ball milled MgH_2	7	500-4000	16.4
Wet ball milled MgH_2	31	30-500	75.5
Wet ball milled MgH_2 with 3wt%Nb_2O_5	13	20-500	78.8
Wet ball milled MgH_2 with 3wt%V	14	20-500	79.4
Wet ball milled MgH_2 with 3wt%CNTs	14	20-500	73.7

The hydrogen desorption experiments of wet ball milled MgH_2 powder with 3wt%Nb_2O_5, 3wt%V and 3wt%CNT were made under an initial vacuum atmosphere (hydrogen pressure of ~0.1Pa) at 350, 300 and 250°C. Before the desorption measurements each powder was pre-heated at 100 °C under vacuum (~0.1Pa) for 2 h.

Figure 4.20 shows the comparison of the desorption behaviour of wet ball milled MgH_2 powder without/with different catalysts at different desorption temperatures.

At 350°C MgH_2 with catalyst Nb_2O_5 shows the best hydrogen desorption behaviour. Addition of both catalysts V and CNTs reveals similar results. All wet ball milled MgH_2 powder with catalysts show an improved hydrogen desorption kinetics compared to wet ball milled MgH_2 powder without catalysts. Wet ball milled MgH_2 with 3wt%Nb_2O_5, 3wt%V and 3wt%CNTs desorbed 5.4wt%, 4.9wt% and 4.3wt% of hydrogen in the first 10 min, respectively, while wet ball milled MgH_2 without catalysts desorbed only 1.1wt% of hydrogen during the same desorption period at 350°C. At 300°C and 250°C wet ball milled MgH_2 powder with 3wt%CNT and 3wt%Nb_2O_5 desorbed hydrogen more quickly than that of wet ball milled MgH_2 powder with 3wt%V and wet ball milled MgH_2 powder without catalysts. Wet ball milled MgH_2 powder with 3wt%CNT and 3wt%Nb_2O_5 showed very similar hydrogen desorption kinetics at 300°C and 250°C. The comparison of hydrogen desorption of wet ball milled MgH_2 without/with catalysts at different desorption temperatures is shown in **Figure 4.21.** Thus for the hydrogen desorption, both Nb_2O_5 and CNTs showed the better improvement in desorption for the used times.

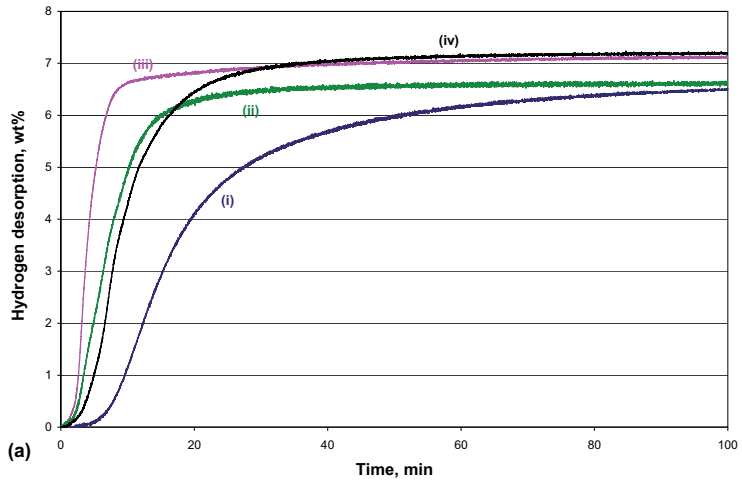

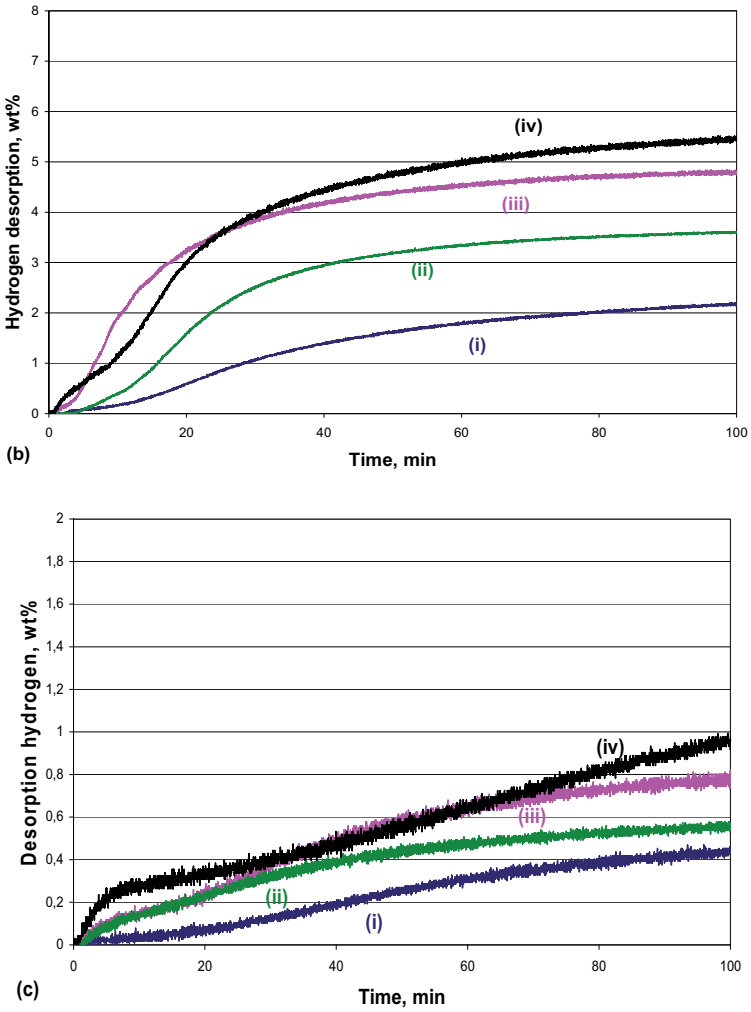

Figure 4.20 Hydrogen desorption of different samples: (i) wet ball milled MgH_2 powder; (ii) wet ball milled MgH_2+3wt%V powder; (iii) wet ball milled MgH_2+3wt%Nb_2O_5 powder and (iv) wet ball milled MgH_2+3wt%CNTs powder under a vacuum atmosphere for three different temperatures: (a) 350°C; (b) 300°C and (c) 250°C.

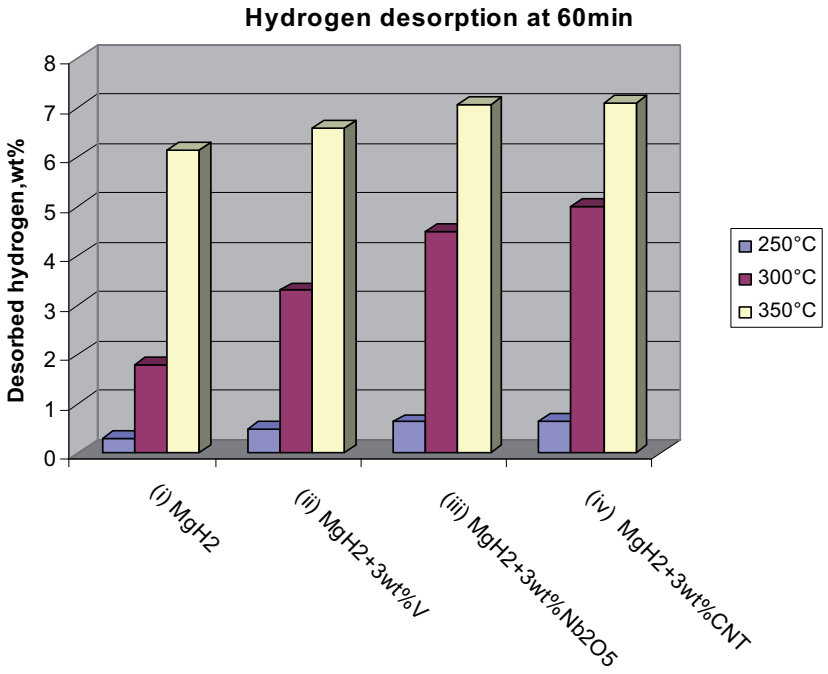

Figure 4.21 Comparison of the desorption of wet ball milled MgH_2 without/with catalysts at different desorption temperatures at 60min desorption.

As the specific surface area of wet ball milled MgH_2 powder without catalysts and with 3wt%Nb_2O_5 is similar (see **Table 4.1**), it might be concluded that the improvement of hydrogen desorption is connected with the influence of Nb atoms on the surface of MgH_2 particles.

The hydrogen desorption under vacuum in the temperature range of 40~450°C with an increasing rate of 0.33Kmin^{-1} was performed in order to determine the initial desorption temperature of wet ball milled MgH_2 powder with Nb_2O_5. **Figure 4.22** shows that wet ball milled MgH_2 powder with 3wt%Nb_2O_5 started to desorb hydrogen from 200°C on while that of wet ball milled MgH_2 powder without catalysts was from about 250°C on. However, the improvement of Nb_2O_5 on hydrogen desorption kinetics of wet ball milled MgH_2 powder was at the expense of hydrogen capacity, which decreased from 7.6wt% to about 7.0wt%.

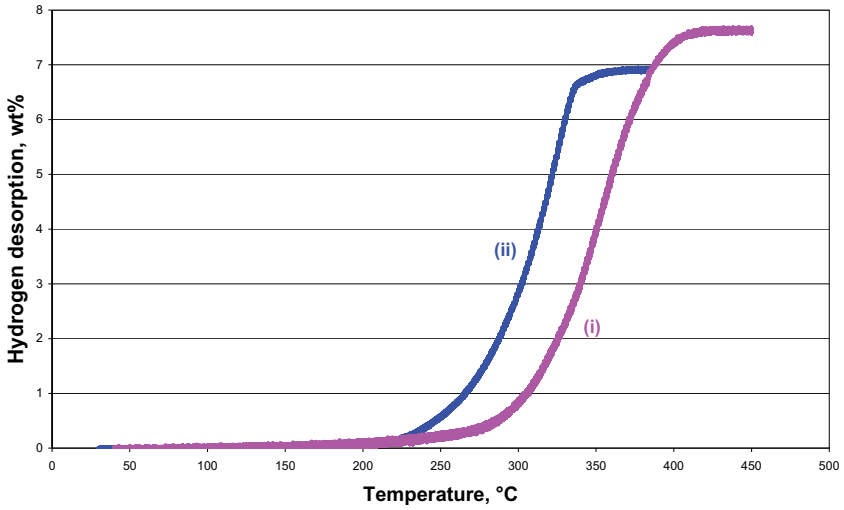

Figure 4.22 Comparison of hydrogen desorption of (i) wet ball milled MgH_2 without catalyst and (ii) with 3wt%Nb_2O_5 in the temperature range from 40~450°C with heating rate of 0.330.33Kmin^{-1}.

The hydrogen absorption of wet ball milled MgH_2 powder with the 3 different catalysts were also performed with the same experimental conditions as the ones of wet ball milled MgH_2 powder without catalysts. **Figure 4.23** presents the hydrogen absorption curves of the wet ball milled MgH_2 powder without/with catalysts under the initial pressure of 12 MPa hydrogen. Before the absorption, all the samples desorbed first at 350°C for 6h with an initial vacuum atmosphere. Then the desorbed wet ball milled MgH_2 powder without/with catalysts was cooled down to the absorption temperature for the further experiments. It is obvious that at all different adsorption temperatures, i.e. 250°C, 200°C, 150°C and 100°C, wet ball milled MgH_2 powder with catalysts show a much better absorption behaviour than that of wet ball milled MgH_2 powders without catalysts. Among the wet ball milled MgH_2 powder with catalysts, the wet ball milled MgH_2 powder with 3wt%Nb_2O_5 demonstrated the best absorption kinetics. The influence of Nb_2O_5 and V on hydrogen absorption behaviour of wet ball milled MgH_2 powder was much stronger than that of CNTs at the different absorption temperatures. At 150°C CNTs showed a slight improvement of the hydrogen absorption behaviour of wet ball milled MgH_2 powder, at 100°C the

CNTs addition even lead to a slow down of the influence on hydrogen absorption kinetics. In **Figure 4.24** the hydrogen absorption amount of wet ball milled MgH_2 powder without/with catalysts after 10min of hydrogen absorption at different temperatures is compared**.** Wet ball milled MgH_2 powder with 3wt%Nb_2O_5 addition showed the highest hydrogen absorption, i.e. 6.8wt%, 6.5wt%, 4.8wt% and 2.0wt% at 250°C, 200°C, 150°C and 100°C, respectively. From improvement of three kinds of catalysts on both hydrogen desorption and absorption, the Nb_2O_5 catalyst showed the best result and might be the most suitable catalyst for an industrial application.

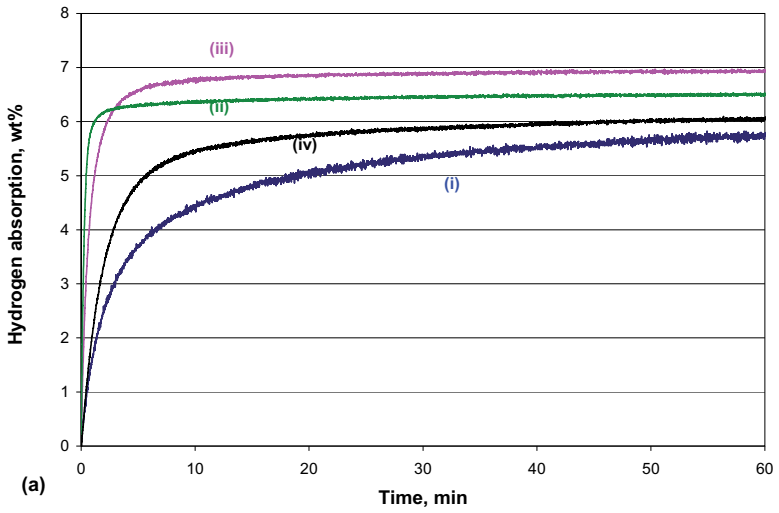

(a)

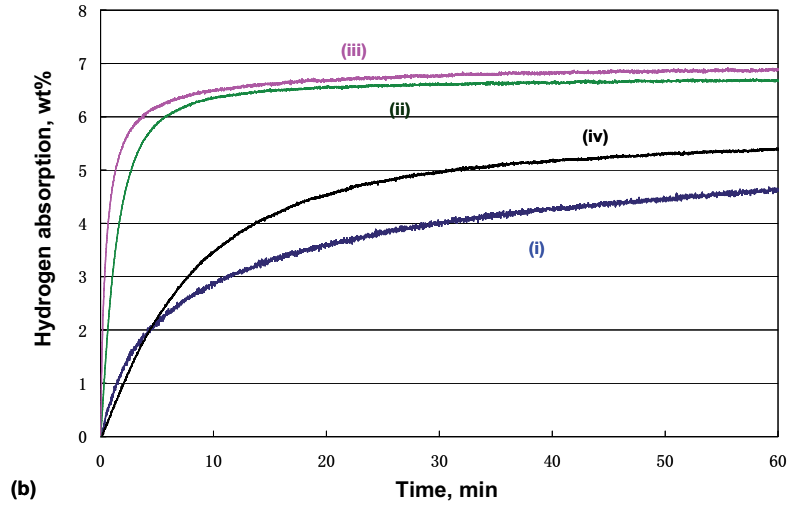
Hydrogen absorption, wt%
Time, min
(iii)
(ii)
(iv)
(i)
0
1
2
3
4
5
6
7
8
0
10
20
30
40
50
60

(b)

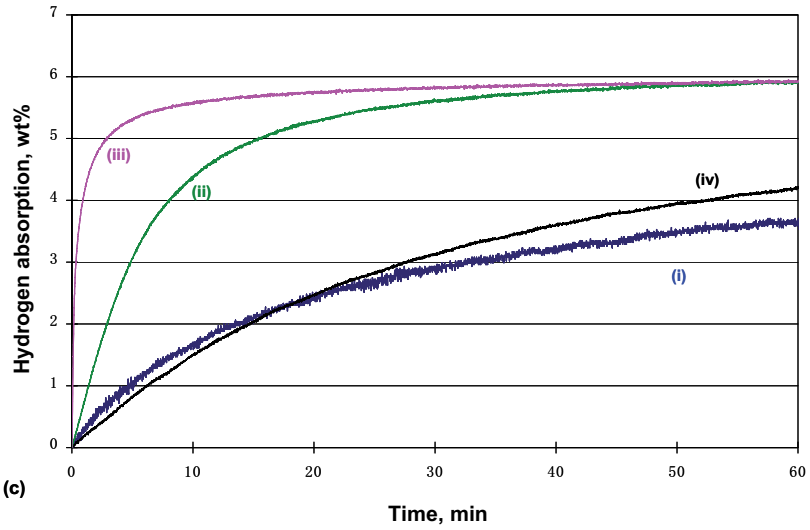
Hydrogen absorption, wt%
Time, min
(iii)
(ii)
(iv)
(i)
0
1
2
3
4
5
6
7
0
10
20
30
40
50
60

(c)

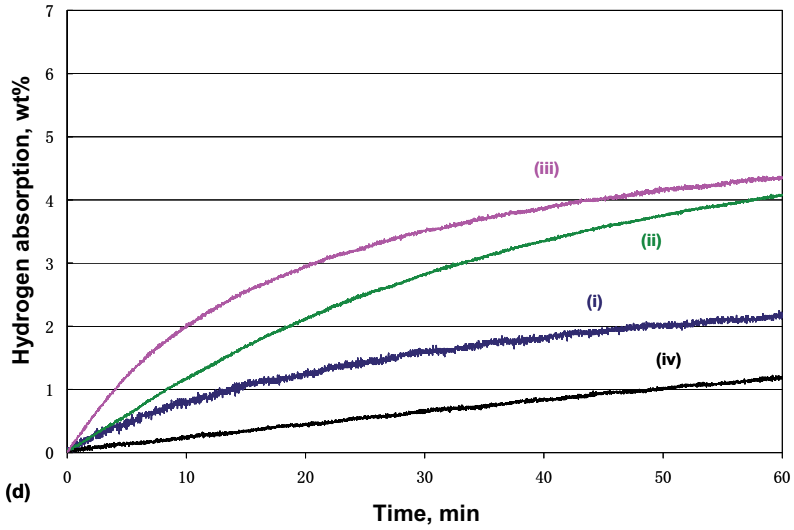

Figure 4.23 Hydrogen absorption of powder: (i) wet ball milled MgH_2; (ii) wet ball milled MgH_2+3wt%V; (iii) wet ball milled MgH_2+3wt%Nb_2O_5 and (iv) wet ball milled MgH_2+3wt%CNT under an initial hydrogen pressure of 12bar at different temperatures: (a) 250°C; (b) 200°C; (c) 150°C; and (d) 100°C.

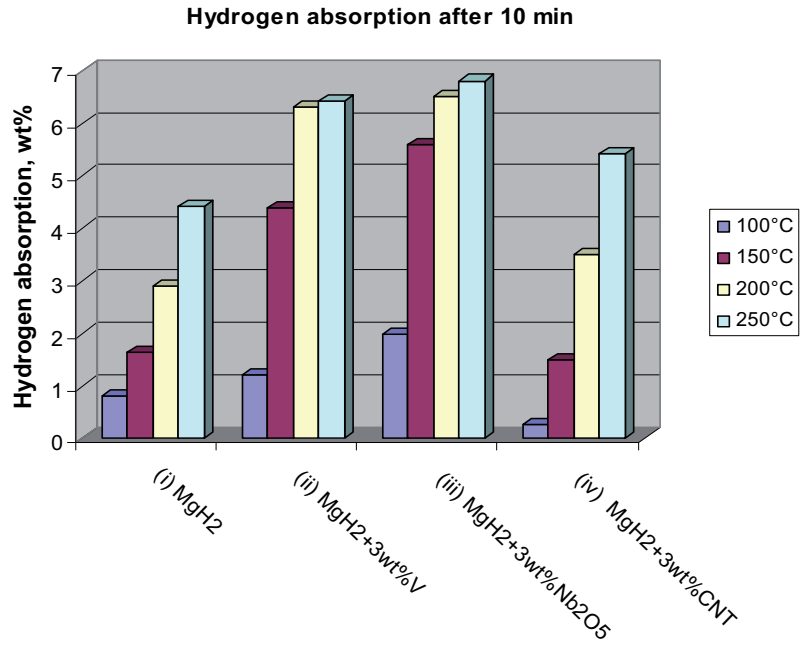

Figure 4.24 Comparison of wet ball milled MgH_2 without/with catalysts at different temperatures at 10min absorption.

It is found that even the specific surface area and particle size of wet ball milled MgH_2 with catalysts were very similar to that without catalysts, the sorption behaviour of wet ball milled MgH_2 was improved due to the addition of catalysts. The reasons expected are: (1) the decrease of grain size had positive influence on improvement of hydrogen sorption. But compared to the previous results (comparison of as-received, dry ball milled and wet ball milled MgH_2 powder sorption), its influence was not as strong as that of decrease of particle size，i.e. Increase of specific surface area; (2) formation of new structure Mg-Nb/V/C-O which could support hydrogen diffusion in the bulk and on the top surface as well as improved the surface reaction. However, the loss of Mg resulted in the decrease of hydrogen capacity compared to wet ball milled MgH_2 without catalysts.

4.1.2.4 Improvement of cycling behaviour due to catalysts

The desorption/absorption cycling properties of wet ball milled MgH_2 powder with 3wt%Nb_2O_5 were also characterized with the volumetric apparatus BELSORP-HP as described above. Totally 10 cycles of hydrogen desorption/absorption were made.

In **Figure 4.25** it is shown that in the 1st desorption, wet ball milled MgH_2 powder with 3wt%Nb_2O_5 had a slower release rate but a larger hydrogen desorption capacity compared to the other cyclic desorptions. From 1st to 5th cycle, its desorption kinetics kept the same but its hydrogen desorption capacity decreased. From 5th cycle to 10th cycle both desorption kinetics and decreased hydrogen capacity remain rather unchanged.

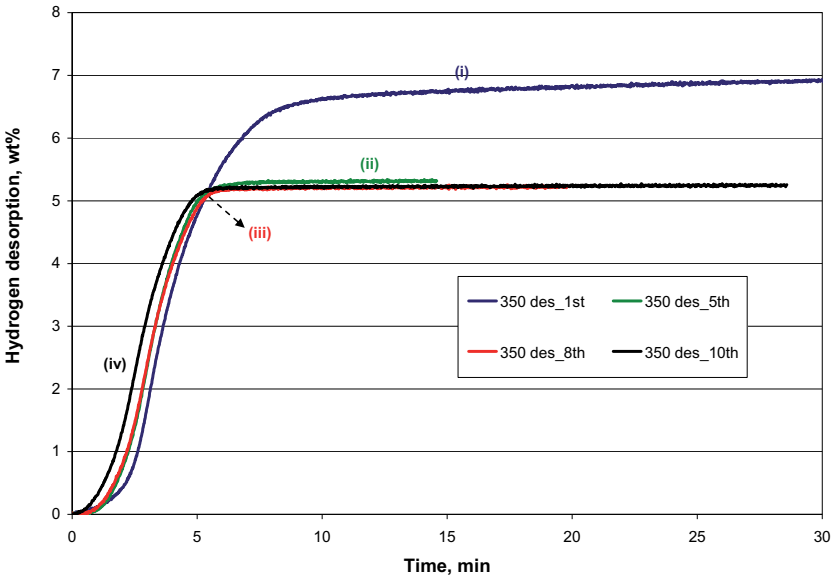

Figure 4.25 Cyclic desorption behaviour of wet ball milled MgH_2 + 3wt%Nb_2O_5 powder at (i) 1st, (ii) 5th, (iii) 8th and (iv) 10th cycle in a vacuum (~0.1Pa) initial atmosphere at 350°C.

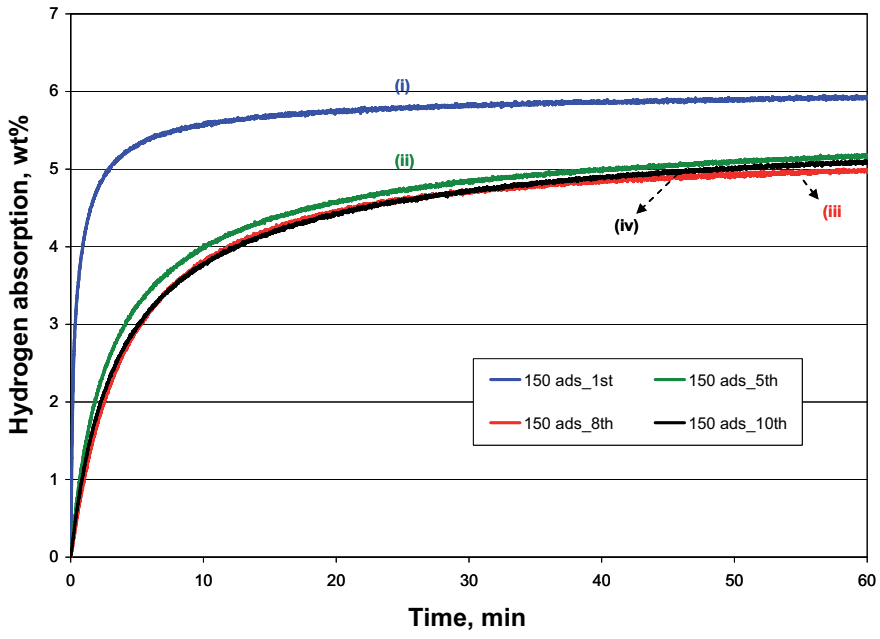

Figure 4.26. Cyclic absorption behaviour of wet ball milled MgH_2 + 3wt%Nb_2O_5 powder at (i) 1st, (ii) 5th, (iii) 8th and (iv) 10th cycle with an initial hydrogen pressure of 12bar at 150°C.

A similar trend is found for the hydrogen capacity during absorption (see **Figure 4.26**). From the 5th cycle on, both hydrogen absorption kinetics and capacity seem to be constant.

In order to determine quantitatively the influence of catalysts on the hydrogen cycling performance, the amount of both desorbed and absorbed hydrogen after 5min for wet ball milled MgH_2 powder without and with catalysts is plotted in **Figure 4.27**.

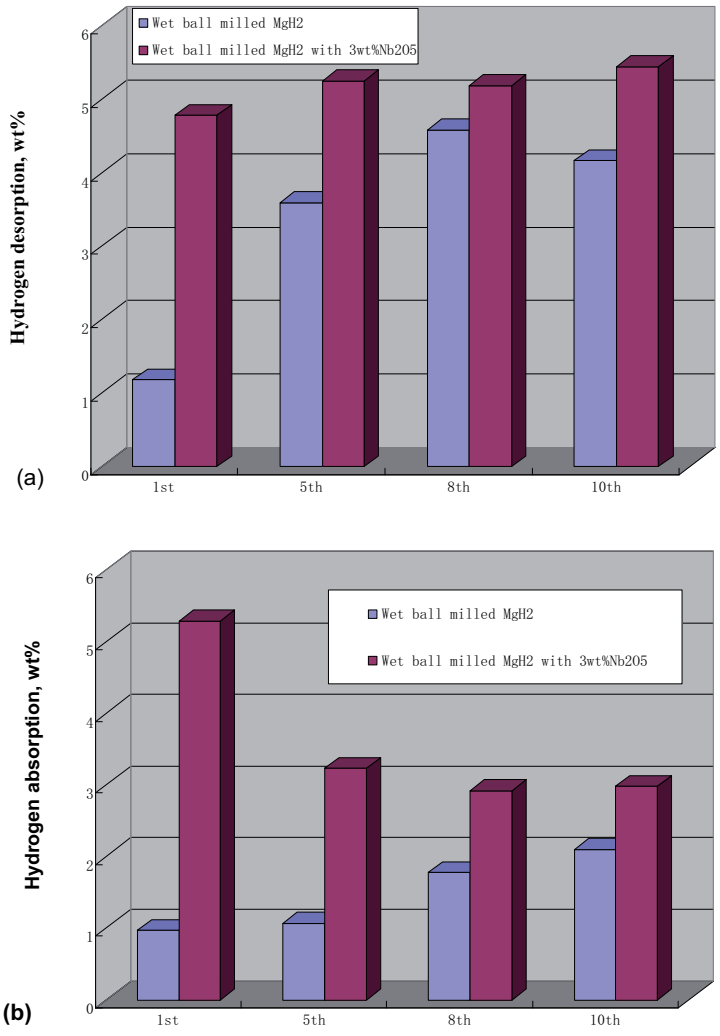

Figure 4.27 Comparison of wet ball milled MgH_2 and wet ball milled MgH_2 with 3wt%Nb_2O_5 after 5min of 1st, 5th, 8th and 10th of (a) desorption and (b) absorption.

Obviously, the cyclic desorbed and absorbed hydrogen amounts are larger for the wet ball milled MgH_2 powder with Nb_2O_5 catalysts. With the number of cycles there is a tendency of a increased absorption of the MgH_2 without catalyst while for the MgH_2 with catalyst a decrease is found.

In conclusion the Nb_2O_5 catalyst in the wet ball milled MgH_2 powder improved its initial sorption behaviour and also improved its cycling sorption performance. The large reduction of hydrogen capacity might be attributed to the formation of Nb-Mg-O at the Nb_2O_5 particles' interfaces with the surrounding MgH_2 nano-grains [83]. GKSS proved that during the desorption process, Nb_2O_5 Bragg peaks disappeared while Bragg peaks of a phase identified as $MgNb_2O_{3.67}$ [83] appeared. This Mg bound with Nb_2O_5 is no more available for hydrogen desorption and absorption, leading to a reduced hydrogen storage capacity. After several cycles (in our experiments it was 5 cycles) the formation of Nb-Mg oxide seems to reach an equilibrium, thus the hydrogen sorption capacity keeps rather stable. Although the formed Nb-Mg-O has a negative on the hydrogen capacity of MgH_2 powder, it could improve the sorption kinetics of MgH_2 due to the pathway effect of hydrogen atoms [84]

4.1.2.5 Thermodynamics of wet ball milled MgH_2 with catalysts

In **Chapter 4.1.1.5**, pressure-composition isotherms (P-C-T diagrams) of the hydrogen absorption of wet ball milled MgH_2 powder are shown. Based on its plateau and the van't Hoff plot the formation enthalpy of wet ball milled MgH_2 powder was calculated, which is similar to the reference formation enthalpy of MgH_2 $\Delta H^0 = -74.5 kJ / mol H_2$ [43]. In this chapter, the same method is used to measure the formation enthalpy of wet ball milled MgH_2 powder with 3wt%Nb_2O_5, 3wt%V and 3wt%CNT, respectively. **Figure 4.28** presents their P-C-T diagrams and the corresponding van't Hoff plots.

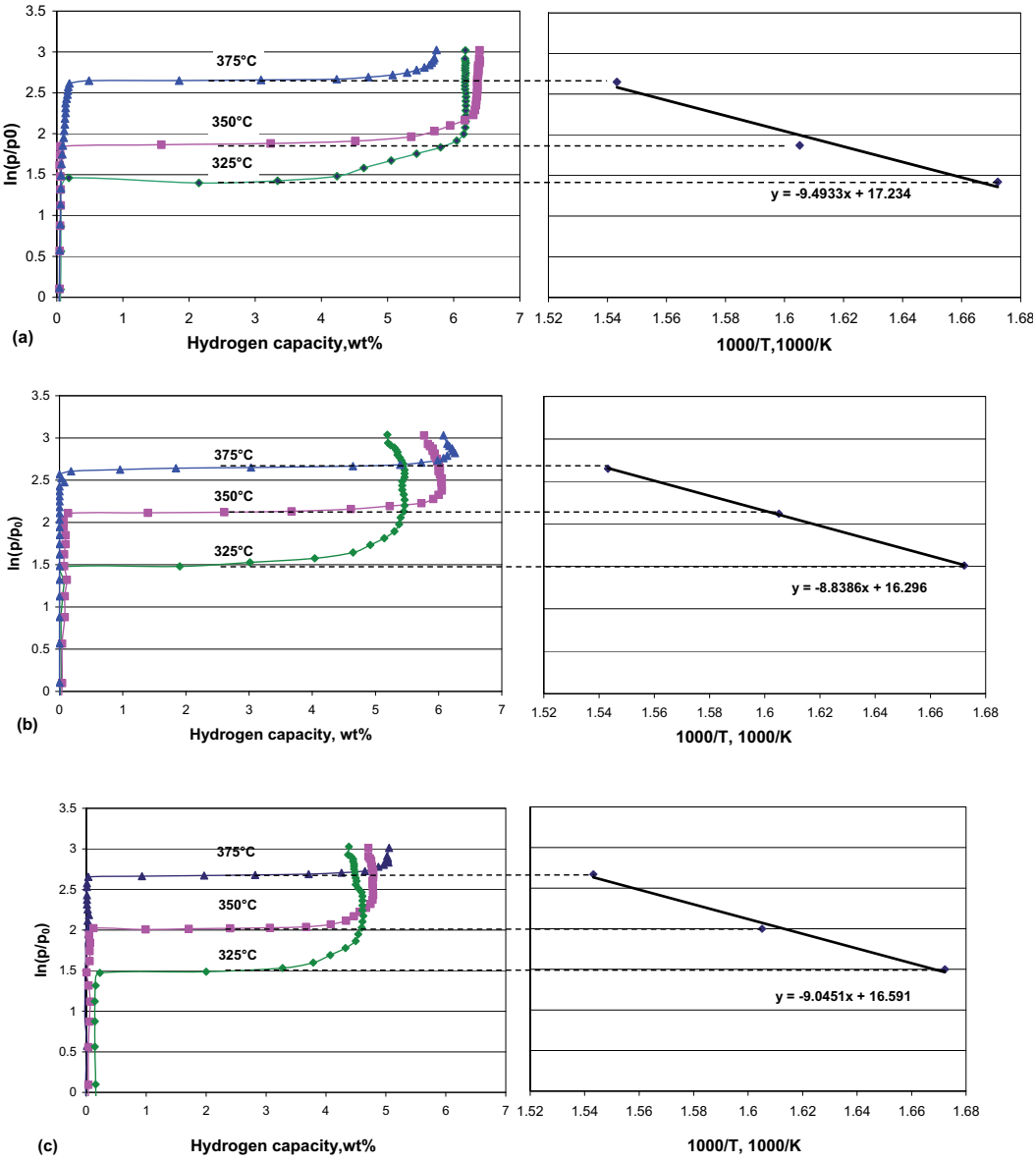

Figure 4.28 Absorbing PCT curves (left) and van't Hoff Plots (right) of wet ball milled MgH_2 powder (a) with 3wt%Nb_2O_5, (b) with 3wt%V and (c) with 3wt%CNTs.

In the above PCT curves, it is shown that with an increase of the absorption temperature, the hydrogen absorption amount increase and the equilibrium hydrogen pressure also is enhanced. Based on the slope of van't Hoff plots, the formation

enthalpies of wet ball milled MgH_2 powder with 3wt%Nb_2O_5, 3wt%V and 3wt%CNTs are calculated by 78.9kJ/molH_2, 73.5kJ/molH_2 and 75.2kJ/molH_2, respectively. They are very close to the reference value which was mentioned above, thus the thermodynamic properties of wet ball milled MgH_2 powder were not influenced by catalysts but mainly its hydrogen sorption kinetics was influenced.

4.1.2.6 Further improvement of the milling conditions for wet ball milled MgH_2 powder with Nb_2O_5 catalyst

In order to further improve the sorption behaviour, an improvement of the milling conditions of the wet ball milled MgH_2 powder with 3wt%Nb_2O_5 was found to achieve a further decrease of particle size and grain size and increase of the specific surface area. Thus after 72h ball milling with 5mm YSZ, another 24h ball milling with 0.1mm diameter YSZ milling balls by the planetary ball mill was applied on the wet ball milled MgH_2 with 3wt%Nb_2O_5 suspension. The suspension was treated as discussed above and the corresponding MgH_2 with Nb_2O_5 powder was produced by the same method and characterized. From the comparison of XRD analysis (see **Figure 4.29**), in the latter case the peaks showed broader than the former case, i.e. a much finer grain size was obtained by further wet ball milling. The grain size in the former case was 13nm while it was 8nm in optimized latter case. A SEM image of the new finer wet ball milled MgH_2 with 3wt%Nb_2O_5 powder is shown in **Figure 4.30**, which proves the particle size is also reduced. The specific surface area of MgH_2 with 3wt%Nb_2O_5 powder from the new milling conditions is about 2.3 times larger than that of the initial case (see **Table 4.2**).

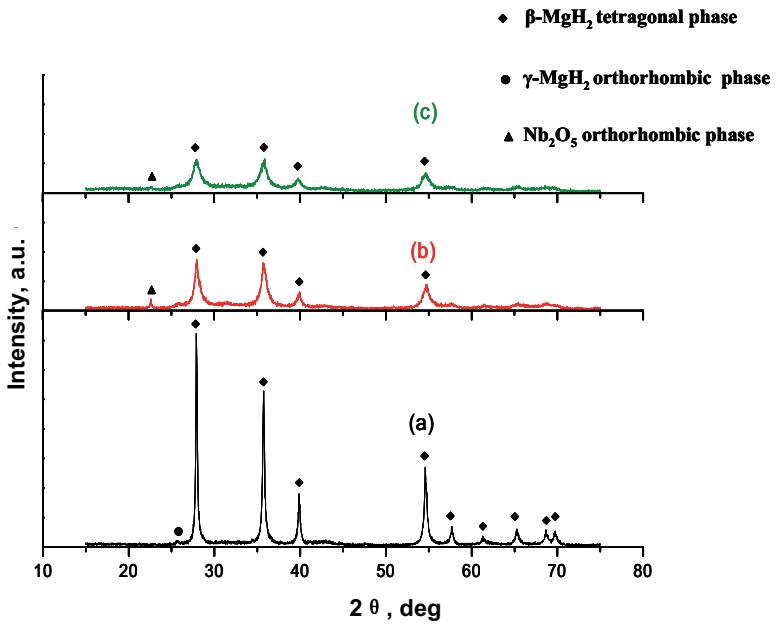

Figure 4.29 XRD patterns of (a)wet ball milled MgH_2 powder without catalyst (72h milling with 5mm diameter YSZ balls), (b)wet ball milled MgH_2 powder with 3wt%Nb_2O_5 (72h milling with 5mm diameter YSZ balls) and (c) wet ball milled MgH_2 powder with 3wt%Nb_2O_5 (72h milling with 5mm and another 24h 0.1mm diameter YSZ balls) .

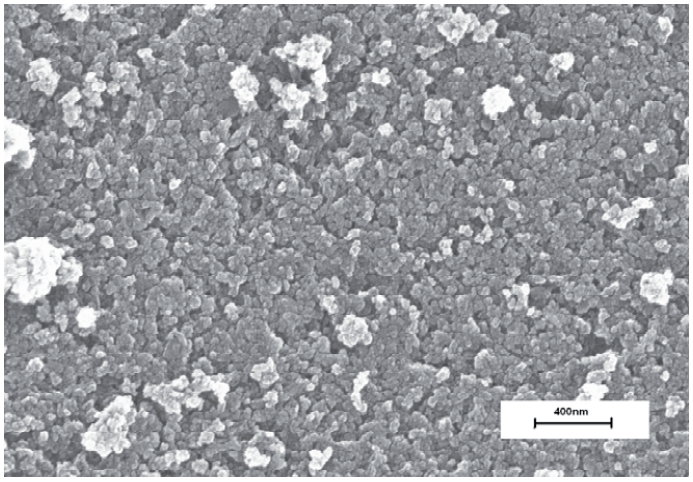

Figure 4.30 SEM image of wet ball milled MgH_2 powder with 3wt% Nb_2O_5 (72h milling with 5mm diameter and another 24h 0.1mm diameter YSZ balls).

The isothermal desorption tests of the improved finer wet ball milled MgH_2 with 3wt%Nb_2O_5 powder were made as before, i.e. with the initial vacuum atmosphere. As

expected the improvement of microstructure leads to an improvement of hydrogen desorption kinetics of wet ball milled MgH_2 with 3wt%Nb_2O_5 powder (see **Figure 4.31)**. For example, after 4min of hydrogen desorption the MgH_2 powders with 3wt%Nb_2O_5 milled with standard conditions desorbed 0.32wt% and 1.77wt% of hydrogen at 300°C and 350°C, respectively. The improved MgH_2 with 3wt%Nb_2O_5 powder desorbed 0.91wt% and 4.65wt% of hydrogen at 300°C and 350°C, giving a 2.6 and 2.8 times increase. Through the previous conclusion from comparison of as-received, dry ball milled and wet ball milled MgH_2 powder (with the same chemical composition), the improvement of hydrogen desorption kinetics in this case is attributed to the extreme increase of specific surface area. A specific surface area of 180.2m^2g^{-1} was determined for the improved powder which is 1.3 times more than the value for the MgH_2 powder milled with the old conditions. Besides, decrease of grain size was also one of the reasons to improve its sorption kinetics. But obviously the microstructural key parameter for the sorption behaviour is the specific surface area of powder. A more detailed discussion will follow also based on a modelling approach.

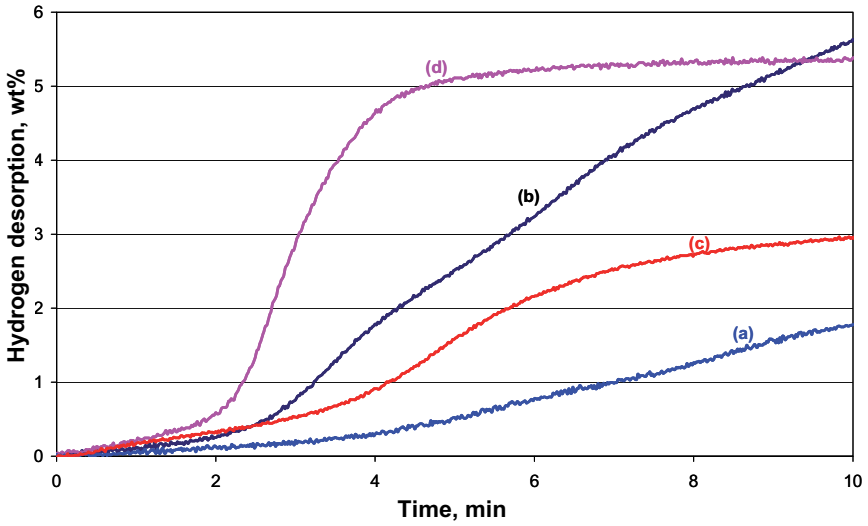

Figure 4.31 Hydrogen desorption at (a) 300°C and (b) 350°C of wet ball milled MgH_2 with 3wt%Nb_2O_5 after 72h milling with 5mm diameter YSZ milling balls; Hydrogen desorption at (c) 300°C and (d) 350°C of wet ball milled MgH_2 with 3wt%Nb_2O_5 after 72h with 5mm diameter and 24h with 0.1mm diameter YSZ milling.

Table 4.2 Comparison of microstructure and hydrogen desorption kinetics of different MgH_2 powder before and after wet ball milling as well as without and with catalyst Nb_2O_5.

Powder	Grain size (nm)	Particle size (nm)	Specific surface area (m^2g^{-1})	Hydrogen desorption amount after 5min at 350°C (wt%)
1. As-received MgH_2	120	20000-100000	6.2	~0
2. Dry ball milled MgH_2	7	500-4000	16.4	~0
3. Standard wet ball milled MgH_2	31	30-500	75.5	1.3
4. Standard wet ball milled MgH_2 with 3wt%Nb_2O_5	13	20-500	78.8	2.2
5. Improved wet ball milled MgH_2 with 3wt%Nb_2O_5	8	20-200	180.2	5.1

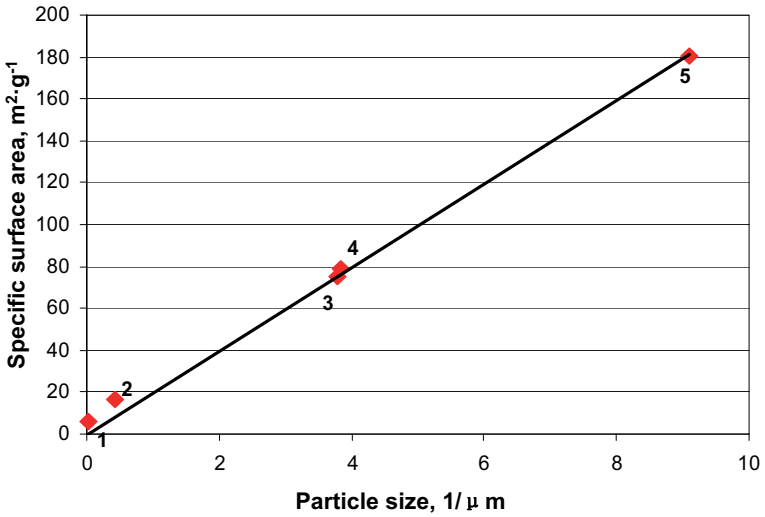

Figure 4.32 The relationship between average particle size and corresponding specific surface area of the samples in Table 4.2.

Compared to as-received, dry ball milled MgH_2 powder, the hydrogen desorption kinetic improvement of wet ball milled MgH_2 powder results from the significant increase of specific surface area (see **Table 4.2**). With the same wet ball milling conditions, catalyst Nb_2O_5 is attributed to the hydrogen desorption kinetic but did not influence of the specific surface area (see **Table 4.2**). With further wet ball milling of MgH_2 with 3wt%Nb_2O_5, its large increase of specific surface area results in the further improvement of hydrogen desorption kinetic (see **Table 4.2**). In a word, the specific surface area is the key micro structural parameter to influence the hydrogen sorption behaviour. The reduction of the particle size due to the high colliding force during ball milling is the mainly attributed to the enlargement of the corresponding specific surface area (see **Figure 4.32**). After hydrogen desorption at 350°C, the specific surface area of wet ball milled MgH_2 with/without Nb_2O_5 was decreased due to the morphology change during the desorption. The specific surface area of standard wet ball milled MgH_2 without/with Nb_2O_5 had the similar specific surface area even after hydrogen desorption. But the standard wet ball milled MgH_2 with Nb_2O_5 had much better hydrogen absorption kinetics compared to MgH_2 without Nb_2O_5 (see **Figure 4.23**), while the improved MgH_2 with Nb_2O_5 showed much better absorption kinetics than the others. These results also proved the previous conclusions again: for the same materials (see. NO.4 and NO.5 in **Table 4.2**), the specific surface area was the critical structural parameter for controlling hydrogen sorption kinetics. But the improvement from NO.3 to NO.4 in **Table 4.2** did not come from the change of specific surface area but from the influence of Nb_2O_5 as mentioned in **Chapter 4.1.2.4**.

4.2 Comparison of results with literature values

A number of research results about the sorption behaviour of dry ball milled MgH_2 powder as well as the influence of catalysts are reported in literatures. In this chapter the current available literature results and our own results about wet ball milled MgH_2 powder without/with catalysts will be compared.

K.S. Jung et al. [85] produced nano-structured MgH_2 powder using a SPEX 8000 miller for 1h, with a ball-to-powder ratio of 10:1. The nano-sized MgH_2 powder was annealed at 350°C for 20h to desorb the hydrogen and to perform absorption experiments. It absorbed 3.3wt% of hydrogen at 300°C and 2.7wt% of hydrogen at 250°C after 100min, respectively. In comparison, our wet ball milled MgH_2 powder absorbed 6.33wt% and 5.97wt% of hydrogen at 300°C and 250°C, respectively.

C.Z. Wu et al. [86] found after 10h ball milling, with 1wt%, 5wt%, 10wt% and 20wt% of single wall nanotubes (SWNTs) addition, the ball milled MgH_2 powder with 5wt% SWNTs showed the best sorption behaviour. After ball milling times longer than 10h, the hydrogen storage capacity decreased. Thus they produced MgH_2 powder with 5wt% SWNTs by ball milling 10h. It desorbed 0.5wt% and 6wt% of hydrogen in 5min at 300°C and 350°C, respectively. Our wet ball milled MgH_2 powder with 3wt% CNTs could desorb 0.7wt% and 2.2wt% of hydrogen in 5min at 300°C and 350°C, respectively. It seems that at the low temperature our wet ball milled MgH_2 powder with 3wt%CNTs desorbed a comparable amount of hydrogen as the dry ball milled MgH_2 powder with 5wt% SWNTs. But at 350°C the sample from C.Z. Wu showed an increased performance. A difference to our work is the used carbon nanotubes. The carbon nanotubes supplied by Bayer Company are multi wall carbon nanotubes. The structural benefit of single wall carbon nanotubes over the multi wall carbon nanotubes might result in an improvement of hydrogen desorption behaviour. Besides, the ball milling time may be another influencing parameter, as for one long milling time, the CNTs might at least partially destroyed (see **Figure 4.17**).

Á. Révész et al. [87] ball milled MgH_2 powders with and without the catalysts Nb_2O_5 under hydrogen in a high-energy mill for 10h. After ball milling, the average particle size range of ball milled MgH_2 powder without catalysts was from 40 to 50 μm, which decreased drastically down to about 0.87 and 0.79 μm for ball milled MgH_2 powder with catalyst Nb_2O_5. In their work, the calculated grain sizes for ball milled MgH_2 without and with catalyst Nb_2O_5 were 9 and 10 nm, respectively. Both ball milled MgH_2 powder without and with catalyst of 2mol%Nb_2O_5 have a maximal hydrogen capacity of 4.7wt% and they could reach the maximal desorption capacity at

300°C in 11 and 15min, respectively, i.e. the catalyst of Nb_2O_5 didn't improve the hydrogen desorption behaviour of ball milled MgH_2 powder. The ball milled MgH_2 powder absorbed 4.7wt% of hydrogen at 300°C in 25min. In comparison, our wet ball milled MgH_2 powder without and with catalyst 3wt%Nb_2O_5 showed the particle sizes in the range of 0.03~0.5 μm and their grain sizes were 31 nm and 13 nm, respectively. The desorption behaviour of wet ball milled MgH_2 powder without and with catalyst (3wt%Nb_2O_5) seems not better than the literature results, but the wet ball milled MgH_2 powder with 3wt%Nb_2O_5 showed an significantly improved hydrogen absorption behaviour. It could absorb 5.3wt% of hydrogen even at 150°C in 5min.

H. Imamura et al. [88] prepared nanosized MgH_2 powder with the help of organic additives which result in small crystallite sizes 9-10nm and a high surface area 24-25m^2/g. The MgH_2 powder milled with bezene for 3h could absorb 2.36wt% of hydrogen in 120min at 180°C after it was desorbed at 350°C for 1h. In our case, the wet ball milled MgH_2 powder had a grain size of 31nm and a much higher surface area of 75.52m^2/g. After desorption at 350°C, it adsorbed 4.34wt% of hydrogen in 120min at 150°C. The improved absorption behaviour can be attributed mainly to the enlargement of specific surface area due to wet ball milling.

Z.Dehouche et al. [89] produced nanosized MgH_2 powder with 5 at.%V using a Spex mill 8000 for a period of 20h. The MgH_2 powder could desorb 3.4wt% of hydrogen at 300°C in 5min and then it reached its maximal hydrogen capacity of 5.7wt% at the same temperature and in the same period. In our case, the wet ball milled MgH_2 powder with 3wt%V desorbed 0.5wt% of hydrogen at 300°C in 5min which is much lower than the Z.Dehouche's results, however, the wet ball milled MgH_2 could absorb 6.3wt% of hydrogen even at 250°C in 5min. The better absorption results in this work can be explained, the higher specific surface area of the wet ball milled MgH_2 powder with 3wt%V (79.4m^2g^{-1}), compared to one of the nanosized MgH_2 powder with 5 at.%V (16.4m^2g^{-1}). The reason why the specific surface area did not influence the hydrogen desorption might be related to a surface contamination due to wet ball milling process.

T.Klassen R. Bormann et al. from the Institute of Material Research in GKSS Research Center have been working on the improvement of hydrogen sorption of MgH_2 by high energy ball milling and catalysts since many years. Till now the results they got are the best sorption results found in the literatures. After ball milling for 200h by a Fritsch P5 planetary mill, nanosized MgH_2 powder with a particle size in the range of 250nm to 5μm and with about 15nm grain size are found. The specific surface area of ball milled MgH_2 powder was $9.1 m^2 g^{-1}$ [90]. It could desorb 7.4wt% at 300°C in 1000s and absorb 6.8wt% of hydrogen at the same temperature in the same period. With the same ball milling parameters, they also produced nanosized MgH_2 powder with 17wt%Nb_2O_5 with much smaller particle size which showed an increased specific surface area of $22.4 m^2 g^{-1}$. The improved microstructure also influenced its sorption behaviour, i.e. it could desorb and absorb 6wt% of hydrogen in 200s at 300°C. In comparison, our wet ball milled MgH_2 powder after 72h ball milling by planetary mill showed particle sizes in the range of 30 to 500nm and a specific surface area of $75.5 m^2 g^{-1}$. The grain size was 31nm. It could desorb 0.6wt% of hydrogen at 300°C and absorb 6.0wt% of hydrogen at 300°C in 1000s. The absorption kinetics of wet ball milled MgH_2 powder was better than that of literature but its desorption kinetics was much poorer. For wet ball milled MgH_2 with 3wt%Nb_2O_5 the similar particle size distribution and the specific surface area ($78.8 m^2 g^{-1}$) were also quite similar to the wet ball milled MgH_2 powder without catalyst $75.5 m^2 g^{-1}$. But with catalyst the grain size of wet ball milled MgH_2 was finer 13nm. The wet ball milled MgH_2 powder with 3wt%Nb_2O_5 desorbed 0.4wt% of hydrogen and adsorbed 6.1wt% of hydrogen in 200s at 300°C. It is obvious that the improvement of Nb_2O_5 on the desorption of wet ball milled MgH_2 was not as good as that given in literature but the absorption was quite similar. The rather bad 1st cycle of desorption behaviour might be explained by surface contaminations. After the 1st desorption, the surface of the powder was activated and the further absorption and desorption kinetics were improved a lot.

Through comparison with above literature results, it is found that the desorption behaviour of wet ball milled MgH_2 powder without and with catalysts seem to be

reduced compared to literature values. From the TEM composition analysis of wet ball milled MgH_2 powder without catalysts, it is found that a part of the top surface of MgH_2 particles is oxidized and the weight percentage of oxygen is 15.1wt% and 21.3at.%. A dense MgO coating could inhibit hydrogen release. However, after desorption the top surface of wet ball milled MgH_2 powder is activated due to the damaged MgO layer, thus the further absorption behaviour is not influenced. From the given comparison, our wet ball milled MgH_2 powder showed a better absorption behaviour than the literature results. Although there might be a negative influence of the MgO layer on the hydrogen sorption behaviour, our wet ball milled MgH_2 powder showed a much better hydrogen sorption behaviour due to the improved microstructure compared to the conventionally dry ball milled MgH_2 powder.

4.3 Mechanism of hydrogen desorption of wet ball milled MgH_2 powder

Up to now the exact mechanism of H_2 desorption from ball milled MgH_2 is not fully understood. There are many different assumptions about the mechanism which were introduced in **Chapter 2.4.1**. At the moment the rate-limiting step in hydrogen desorption from MgH_2 has been proposed to be either the diffusion pathways of hydrogen through the magnesium grains formed on the surface of the particle, or the recombination of H_2 molecules on the particle surface prior to desorption [91]. In this part our own model and the modelling results will be introduced to prove which step mentioned above is the real controlling one. Compared to the hydrogen absorption at the certain temperature the hydrogen desorption shows lower kinetics (shown in **Chapter 4.1.1.3**. Therefore this work mainly focuses on modelling of hydrogen desorption of MgH_2 powder. Based on the modelling results, the relationship between the kinetics of the hydrogen desorption in MgH_2 powder and the microstructual parameter, e.g. specific surface area can be analysed.

4.3.1 Typical features of hydrogen desorption behaviour of wet ball milled MgH_2 powder

Based on the hydrogen desorption of wet ball milled MgH_2 powder shown in **Figure 4.8c** some inheriting features are summarized here:

- Desorption behaviour is temperature dependent. It seems that one lowest temperature exists below no hydrogen desorption is observed;
- There is a delay of hydrogen desorption at the beginning of the isothermal desorption.
- The main part of the desorption curve is linear increase;
- Finally there is an asymptotic behaviour of desorption approaching the saturation limit.
- Increase of specific surface improves the kinetics

In this work the model is built up to reproduce the main part of the hydrogen desorption behaviour.

4.3.2 Construction of the model and corresponding results

The modelling of hydrogen desorption of MgH_2 powder is built up based on the assumptions made in **Chapter 2.4.3** and the shrinkage model of hydrogen desorption in **Figure 2.5.**

In this model the hydrogen desorption process is divided into the following stages:

- Hydride decomposition on the β-surface: A transition of hydrogen atoms bounded in the stoichiometric MgH_2 hydride into the Mg surrounded with dissolved hydrogen atoms. This process (called later as β-dissolution) is localized on the surface of the β-phase (β-surface).
- Hydrogen diffusion in the Mg hydrogen solid solution (called later as α-diffusion)

- Degassing from the top surface of the α-phase (α-surface): Several processes take place on the outer surface of the α-phase (α-surface), which is in contact with the hydrogen gas. For example penetration of hydrogen atoms through the surface of particles, combination of the hydrogen atoms at the surface of the particle and leave from the surface to the hydrogen gas.

It is clear that the kinetics of the hydrogen desorption process should be controlled by the slowest step of them mentioned above. It is known that the phase transition of α-phase to β-phase compared to the other two steps is very fast [62]. Thus the kinetics of hydrogen desorption in this model is controlled by either hydrogen diffusion in the α-phase or degassing from the top surface of the particles.

Corresponding to the discussion above the modelling is divided into:

- Case I: hydrogen diffusion in α-phase is the rate controlling step;
- Case II: degassing is the rate-controlling step.

In case I, the characteristic diffusion rate is supposed as:

$$k = \frac{0.0766m}{2M_H}\frac{D}{L^2}$$

where k is the desorption rate, m is the mass of sample powder, 7.66wt% is the theoretical maximal hydrogen capacity in MgH_2, D represents the diffusion coefficient and M_H stands for the molar mass of hydrogen atoms $1.008 \cdot 10^{-3}$kg mol^{-1}. Among them, the diffusion coefficient D of hydrogen atoms in magnesium based on the different experiments [92 , 93] ranges from $1.54 \cdot 10^{-6} e^{-\frac{40000}{RT}}$ to $1.54 \cdot 10^{-6} e^{-\frac{24100}{RT}}$ m^2 s^{-1}. For a 149mg sample ($L \sim 200nm$) at 350°C desorption temperature the desorption rate is between 0.096 and 2.08mol s^{-1}. However, the experimental desorption result at 350°C of wet ball milled MgH2 powder (see **Figure 4.8**) shows the desorption rate is about $5.33 \cdot 10^{-4}$ mol s^{-1}. Thus it seems to be unrealistic that diffusion of hydrogen atoms in α-phase is the controlling step of hydrogen desorption of wet ball milled MgH_2 powder. Therefore, in the following work the desorption kinetics is supposed to be controlled only by the α-surface degassing.

The diffusion transfer of dissolved hydrogen in solid Mg and MgH_2 is described by the Fick's current $j = -D\nabla c$, with c-volume concentration of hydrogen atoms, m^{-3}, which also appears later as the molar concentration; D is the Fick's diffusion coefficient, for both regions of α- and β- phase D_α, D_β are constant respectively. A schematic of the hydrogen concentration in the two phases is shown in **Figure 4.33**.

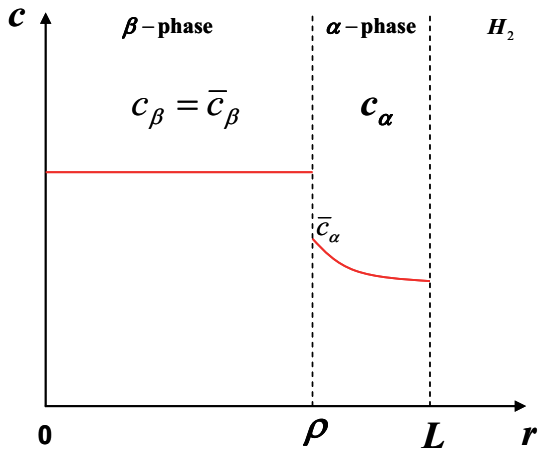

Figure 4.33 Hydrogen concentration distribution in α- and β- phases during hydrogen desorption of MgH_2. r is the distance from core center of the particle to the particle boundary. ρ and L are the distances from core center of the particle to the β -phase and α -phase edges. c_α and c_β are hydrogen concentration in the β -phase and α -phase, respectively.

Due to assumed spherical symmetry of the Mg/MgH_2 particles, the balance of hydrogen concentration due to diffusion is:

$$\frac{\partial c}{\partial t} = D\left(\frac{\partial^2 c}{\partial^2 r} + \frac{2}{r}\frac{\partial c}{\partial r}\right) \qquad \textbf{(4. 1)}$$

where r is distance between particle centre and an arbitrary point in the whole particle (see **Figure 4.33**).

In the model, the β-phase forms the MgH_2-core inside of the particle with radius ρ. The surface of the β-phase (β-surface) moves entirely with the condition of

hydrogen mass balance (out-/inflow). It leads to a simple moving boundary condition (so called 'Stefan-condition') at $r = \rho$:

$$(c_\beta - c_\alpha)\frac{\partial \rho}{\partial t} = D_\beta \frac{\partial c_\beta}{\partial r} - D_\alpha \frac{\partial c_\alpha}{\partial r} \quad \textbf{(4. 2)}$$

where c_α and c_β are hydrogen concentration inside of α - and β - phases, respectively.

In **Figure 4.33** the surface of the α -phase (α -surface) is the interface between the α -phase and the atmosphere H_2 gas. Based on the mass balance of the $H_2 \leftrightarrow 2H$ process, the equilibrium of chemical potentials provides the proportionality $p \sim c_\alpha^2$, or

$$p = C_s(T)c_\alpha^2 \quad \textbf{(Sievert's law)} \quad \textbf{(4. 3)}$$

where C_s is the Sievert's equilibrium constant depending on temperature.

From the desorption curves of wet ball milled MgH_2 powder shown in **Figure 4.8,** the main hydrogen desorption appears to be a linear determined with a tangential ascent which represents desorption rate under the isobaric process and is based on two simplifying assumptions:

1. The $\bar{c}_\alpha$ is the hydrogen atom concentration on the β- surface (see **Figure 4.33**), which doesn't change with the shrinkage of the β- core, i.e. $\bar{c}_\alpha = X$. The hydrogen concentration in the β- phase is always constant $\bar{c}_\beta = Y$.

2. The concentration profile $c_\alpha(r)$ obeys:

$$c_\alpha(r) = A/r + B \quad \textbf{(4. 4)}$$

where A and B are constant. $A > 0$ for hydrogen desorption.

Under these assumptions and the Stefan boundary condition mentioned in equation (4.2), on the β surface, it holds:

$$(\bar{c}_\beta - \bar{c}_\alpha)\dot{\rho} = -D_\alpha A/\rho^2 \quad \text{i.e. } (Y - X)\dot{\rho} = -D_\alpha A/\rho^2 \quad \textbf{(4. 5)}$$

On the boundary between α - phase and hydrogen molecular gas, the desorption kinetic is governed entirely by two counter currents corresponding to the $H_2 \leftrightarrow 2H$ reaction. The rate of both processes is dependent on the concentration of hydrogen atoms in α -phase close to α -surface and the concentration of H_2 molecules outside of α -surface, which is proportional to the hydrogen pressure. From this point on, the further deduction should be completed corresponding to two cases, i.e. degassing process or diffusion in α -phase is the desorption rate controlling step:

In this case, the hydrogen atom concentration in the α -phase on α -surface and on β -surface can be regarded as the same. Therefore the flux of hydrogen atoms on the α -surface is:

$$-D_\alpha \nabla c_\alpha\big|_{r=L} = D_\alpha A / L^2 = b\bar{c}_\alpha^{2} - kp = bX^2 - kp \qquad \textbf{(4. 6)}$$

where $b\bar{c}_\alpha^{2} = bX^2$ is the hydrogen flux from α -phase to α -surface with positive constant b (responsible for hydrogen atoms to form hydrogen molecules and release from α -surface). kp is the hydrogen flux from the hydrogen molecular to α -surface with another positive constant k (responsible for dissociation of hydrogen molecules to hydrogen atoms on the α -surface) and hydrogen pressure p. Here a Sievert's constant is defined as $C_s = b/k$.

Combining the boundary conditions with equations (4.5) and (4.6), the resulting kinetic equation for evolution of the β -core with radius ρ becomes then:

$$(\bar{c}_\beta - \bar{c}_\alpha)\rho^2\dot{\rho} = -L^2(b\bar{c}_\alpha^{2} - kp) \quad \text{i.e.} \quad (Y - X)\rho^2\dot{\rho} = -L^2(bX^2 - kp) \qquad \textbf{(4. 7)}$$

This model does not include the diffusion mechanism explicitly and for hydrogen desorption with $\phi = (b\bar{c}_\alpha^{2} - kp) > 0$. If the factor ϕ approaches to 0 during the desorption, it means the pressure approaches to the saturation value $\bar{p}$.

$$p \to \bar{p} = \frac{b}{k}\bar{c}_\alpha^{2} = \frac{b}{k}X^2 \qquad \textbf{(4. 8)}$$

In our case the volumetric equipment BELSORP-HP is used for measuring the desorbed hydrogen pressure. At the beginning of the desorption, the pressure inside the system is quite low, it can be regarded as the isobaric case. With the increase of desorbed hydrogen pressure, the pressure inside the system increases to a large value and enhances the reverse process, i.e. absorption process. In general, the sorption runs under the isochoric condition. Thus under two situations, i.e. isobaric and isochoric cases, this model can be used.

The calculation of the desorption below is performed for the isobaric case. All particles assumed to be spherical with an equal radius L. The relative volume V of β-core is:

$$V = (\rho / L)^3 \qquad \textbf{(4. 9)}$$

With this notation, the kinetic equation (4.7) becomes:

$$(Y - X)\frac{L}{3}\dot{V} = -(bX_2 - kp) = -k(\overline{p} - p) \qquad \textbf{(4.10)}$$

with $p = bX^2 / k$ from (4.8). The equation (4.10) for constant temperature T and constant pressure p is easily integrated. With the initial condition: $V(0) = 1$, i.e. desorption starts from the stoichiometric MgH_2 hydride, the evolution of the inner β-core is:

$$V(t) = 1 - \frac{k(\overline{p} - p)}{Y - X} \cdot \frac{3}{L} t \qquad \textbf{(4.11)}$$

With the final condition: $V(\tau) = 0$, i.e. the particle becomes the pure homogeneous Mg hydrogen solution, i.e. α-solution with the critical concentration $\overline{c}_\alpha$. Thus the time for complete desorption, i.e. complete decomposition of β- phase is:

$$\tau = \frac{L}{3k} \cdot \frac{(Y - X)}{\overline{p} - p} \qquad \textbf{(4.12)}$$

where $\overline{p} - p = const. > 0$. It can be used for evaluation of desorption kinetics at the very beginning of the process where the dynamics looks approximately linear.

The calculation performed above is based on the assumption, the desorption runs under the constant external pressure p. Actually the real kinetics of the sorption behaviour is essentially sensitive to an external pressure with the desorption running. With the volumetric equipment the desorption process is not isotherm-isobar but isotherm-isochor. Therefore, the ascent of pressure in the system is taken into account in order to describe an experimental kinetic curve.

The initial volume of single MgH_2 particle is defined as $v_{\sin gle} = \frac{4\pi}{3} L^3$ and the volume change from β-phase to α-phase is defined as η. Thus the molar amount of desorbed hydrogen molecules is:

$$v_{\sin gle}^{des} = \frac{1}{2}\left(\frac{4\pi}{3} YL^3 - \left(\frac{4\pi}{3} YL^3 + \frac{4\pi}{3} X\left(L^3 - \rho^3\right)\eta\right)\right) \qquad \textbf{(4.13)}$$

After a series of derivation of equation (4.13) and with equation (4.9), the simplified form is obtained:

$$v_{des} = \frac{1}{2} v_{\sin gle}^{des} (1 - V) \cdot [Y - \eta X] \qquad \textbf{(4.14)}$$

An alternation of the mass density and the volume change rate $\eta \approx \rho_{MgH_2} / \rho_{Mg} \approx 0.77$ during the desorption is taken into account here. Under the assumption that all particles have the same size, the mole number N of particles in the sample is:

$$N = m/(\rho_{MgH_2} \cdot v_{des}) \qquad \textbf{(4.15)}$$

where m is the initial mass of the MgH_2 powder.

For a 100%-pure stoichiometric MgH_2 powder, if no leakage occurs, the pressure p produced by desorbed hydrogen in the measurement volume is a function of the β-phase core in each single particle:

$$v^{des} = N \cdot v_{\sin gle}^{des} \qquad \textbf{(4.16)}$$

With the gas law and equation (4.16), the hydrogen pressure is:

$$p(\tilde{r}) = \frac{R \cdot v^{des}}{\{V/T\}} = \frac{m \cdot R}{2 \cdot \rho_{MgH_2} \cdot \{V/T\}} (1 - V) \cdot (Y - \eta X) \qquad \textbf{(4.17)}$$

and time evolution of the pressure is described by:

$$\dot{p}(\tilde{r}) = -\frac{m \cdot R \cdot (Y - \eta X)}{2\rho_{MgH_2} \cdot \{V/T\}} V = \frac{3 \cdot k \cdot m \cdot R(\bar{p} - p)}{2 \cdot L \cdot \rho_{MgH_2} \cdot \{V/T\}} \approx k\varepsilon(\bar{p} - p) \qquad \textbf{(4.18)}$$

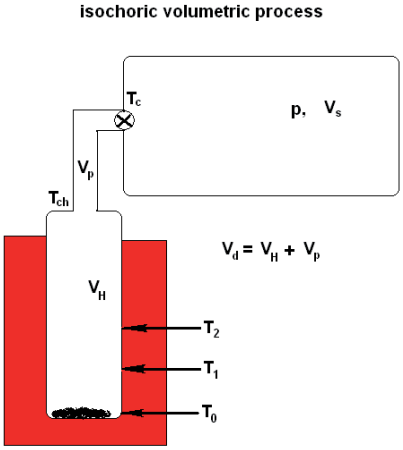

Figure 4.34 Schematic of BELSORP-HP system.

In equation (4.18) the symbol V/T means the effective ratio of {V/T} for gas with inhomogeneous temperature distribution in the volumetric space. If the gas temperature is overall homogeneous and constant, it is exactly the ratio V/T. In our case the volumetric system is shown in **Figure 4.34**. And in **Figure 4.34** the symbols have the meaning as follows:

V_H - the volume of the holder with the sample and hot gas in the thermostat at T_0;

V_p - volume of the pipe channel containing the gas with the descendent temperature from T_{ch} down to T_c;

V_d – dead volume;

V_s - the system volume behind the valve, with the cold gas of temperature T_c;

T_1, T_2, T_{ch} the temperature measured in control points.

T_c, T_0 are set by the experimental conditions.

The sample holder is directly heated by furnace. The temperature distribution in the whole system is qualitatively shown in **Figure 4.35**.

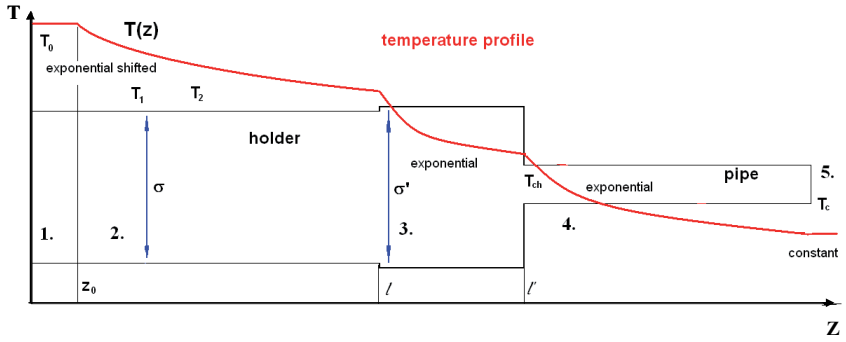

Figure 4.35 Temperature distribution profile in the volumetric system (BELSORP-HP)

For the inhomogeneous temperature profile, the effective ratio {V/T} is defined:

$$\{V/T\} = \frac{v}{p}R \qquad \textbf{(4.19)}$$

It is composed of (see **Figure 4.35**):

(1). Furnace heated segment at T_0: $\{V/T\}_1 = z_0\sigma/T_0$;

(2). First exponential segment ($z_0 \to l$): $\{V/T\}_2 = \int_{z_0}^{l}\frac{dz}{T(z)} = \frac{\sigma}{\bar{T}\tau}\ln\left[1+\frac{\bar{T}}{T_0}\left(e^{\tau(l-z_0)}-1\right)\right]$

(3). Second exponential segment ($l \to l'$)

$$\{V/T\}_3 = \int_{l}^{l'}\frac{dz}{T(z)} = \sigma'\frac{l'-l}{\bar{T}\left[\ln\frac{T_0-\bar{T}}{T_{ch}-\bar{T}}-\tau(l-z_0)\right]}\cdot\ln\frac{T_{ch}}{\left(T_{ch}-\bar{T}\right)\left[1+\frac{\bar{T}}{T_0-\bar{T}}e^{\tau(l-z_0)}\right]}$$

(4). Third exponential segment (pipe of length L):

$$\{V/T\}_4 = \int_{pipe}\frac{dz}{T(z)} = \frac{V_p}{\bar{T}\ln\frac{T_{ch}-\bar{T}}{T_c-\bar{T}}}\cdot\ln\left(\frac{\bar{T}}{T_{ch}}\cdot\frac{T_{ch}-T_c}{T_c-\bar{T}}+1\right)$$

(5). Cooled volumetric pool at T_c corresponding to 25°C: $\{V/T\}_5 = V_s/T_c$.

Thus the effective ratio $\{V/T\}$ in the inhomogeneous temperature profiles:

$$\{V/T\} = \Sigma_i\{V/T\}_i \qquad \textbf{(4.20)}$$

here $V_p = V_d - V_H$ is the dead volume, $\frac{\sigma'}{\sigma} = \left(\frac{r'}{r}\right)^2$ is the ratio of two inner cross sections of the sample holder.

For practical purposes we need also the effective ratio of "dead volume":

$$\{V/T\}_d = V/T - V_s/T_c$$

In equation (4.18) the coefficient ε is defined as: $\varepsilon = \frac{3mR}{2L\rho_{MgH_2}\{V/T\}} > 0$. And for the desorption process is assumed that $\overline{p} - p > 0$.

With the initial value of p_0 the solution of equation (4.18) for desorption is:

$$p(t) = \overline{p} - (\overline{p} - p_0)e^{-\varepsilon kt} \qquad \textbf{(4.21)}$$

The model reproduces therefore a desorption process starting from the initial pressure p_0 and running down to approach the threshold pressure $\overline{p} = bX^2/k$ shown in **Figure 4.36**.

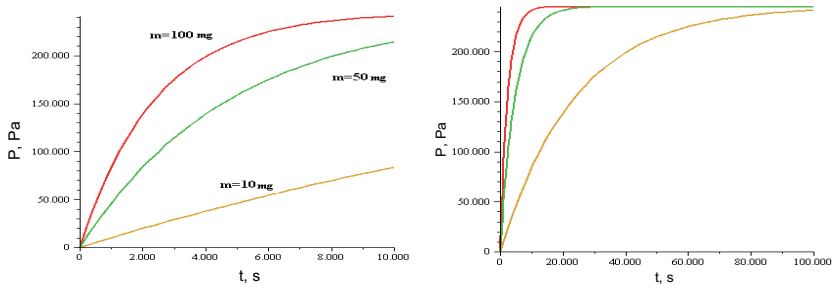

Figure 4.36 Experiments of desorption kinetics for two time intervals, starting from vacuum

The equation (4.21) does not take into account the finite amount of desorbed hydrogen. It is defined independently by the hydrogen capacity of the sample. Assume that a sample compound doesn't only consist of pure magnesium hydride, but with a purity $\psi = m_{MgH_2}/m_{sample}$, after the full decomposition of β-phase into α-phase, the produced hydrogen pressure is:

$$p_{\beta\to\alpha} = \frac{\psi \cdot m_{sample} \cdot Y \cdot R}{2 \cdot \{V/T\} \cdot \rho_{MgH_2}}\left(Y - \eta X^{des}\right) = \frac{L\varepsilon}{3}\left(Y - \eta X^{des}\right) \qquad \textbf{(4.22)}$$

The total desorbed hydrogen should produce the maximal hydrogen pressure:

$$p_{\max} = \frac{\psi \cdot m_{sample} \cdot Y \cdot R}{2 \cdot \{V/T\} \cdot \rho_{MgH_2}} = \frac{L\varepsilon}{3} Y \qquad \textbf{(4.23)}$$

which is in fact only about 0.2~ 0.7% of $p_{\beta\to\alpha}$, since they obeys the relationship $p_{\beta\to\alpha} / p_{\max} = 1 - \eta X / Y$.

As a result of a continuous measurement of pressure in a closed volumetric equipment with desorbing sample, the following two cases are possible:

Case I: If the maximal pressure $p_{\max}$ achieved by desorption is higher than the saturation pressure $p_{eq} \equiv \overline{p}$, the slope of the desorption curve approaches this asymptotic value $\overline{p}$, the rest of hydrogen remains in the sample (see **Figure 4.37** dash lines).

Case II: Otherwise if $p_{\max} < \overline{p}$, the curves are restricted by $p_{\max}$ (see **Figure 4.37** solid lines).

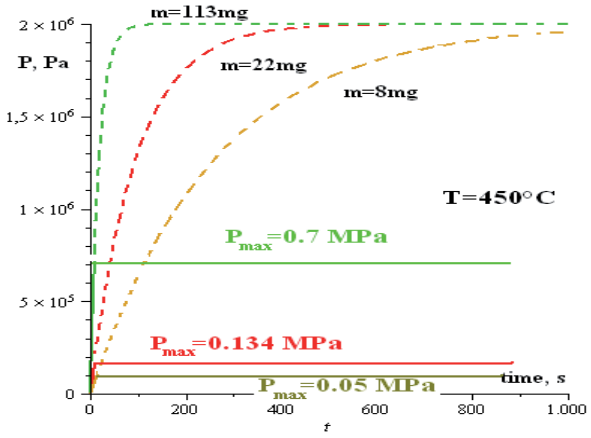

Figure 4.37 Asymptotic saturation pressure (dash lines) vs. maximal pressure (solid lines).

For experimental validation of the model as well as evaluation of the desorption kinetics, the factual amount m_{MgH_2} of magnesium hydride in the sample should be

estimated, and then it must be distinguished attentively between these two possibilities, although the shape of resulting kinetic curves appears to be very similar to each other.

As it was shown above, the simple linear model reproduces the progress of pressure by desorption $p(t)$ as measured. The results of the diagram $\%wt(t)$ (the hydrogen sorption mass percentage) usually can be performed by the definition with equation (4.21):

$$\%wt(t) = \frac{m_{H_2}}{m_{MgH_2}} \cdot 100\% = \frac{\mu_{H_2} \cdot \{V/T\}}{m_{sample} \cdot \psi \cdot R} \left[\overline{p} - (\overline{p} - p_0) \cdot e^{-\varepsilon k t}\right] \cdot 100\% \qquad \textbf{(4.24)}$$

where μ_{H_2} is the mole mass of the hydrogen molecule. Due to the quite small starting pressure p_0 compared to $\overline{p}$, equation (4.24) can be simplified:

$$\%wt(t) = \frac{100\% \cdot \mu_{MgH_2} \cdot \{V/T\}}{m_{sample} \cdot \psi \cdot R} \overline{p}^{\,des} \cdot \left[1 - e^{-\varepsilon k t}\right] \qquad \textbf{(4.25)}$$

The molar concentration of hydrogen atoms in the stoichiometric magnesium hydride MgH_2 is $Y = c_\beta = 110199 mol/m^3$. An average particle size can be obtained from the SEM evaluation. For the wet ball milled MgH_2 powder the diameter of particle is $2L = 31nm$ (see **Table 4.2**).

Some examples for practical evaluation of measurement results are presented below. The measurement at $m_{sample} = 142mg$ and $T = 350°C$ ($\overline{p}^{des}_{350°C} = 394kPa$, $\{V/T\}_{350°C} = 1.0073 \cdot 10^{-7}$) exhibits like the case II, which can be fitted for purity 80% with a constant $k_{350°C} = 1.6 \cdot 10^{-12} mol/(m^2 \cdot s \cdot Pa)$ shown in **Figure 4.38**. Another measurement is shown for 180mg MgH_2 powder desorbing at 300°C (**Figure 4.39**). The desorbed hydrogen amount corresponds to $p_{\max} = 447kPa$ for the same purity 80% as above, it belongs to case I. The pressure reached $p = 164kPa$ for a purity of $\psi = 80\%$, the shape of $p(t)$ can be fitted with $k_{300°C} \approx 4.6 \cdot 10^{-13} mol/(m^2 \cdot s \cdot Pa)$.

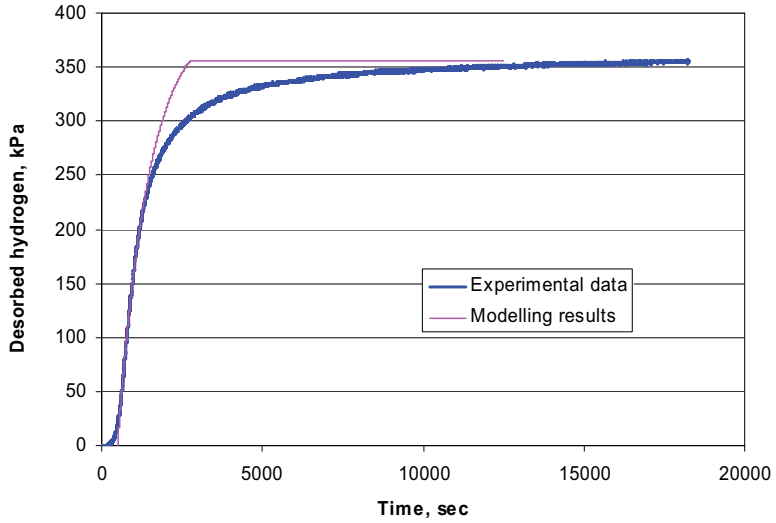

Figure 4.38 Desorption of 142 mg 80% wet ball milled MgH_2 powder at 350°C, Case II

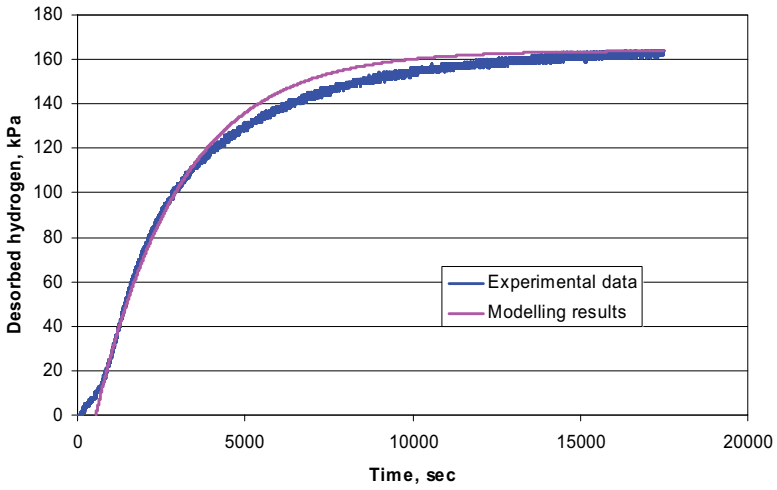

Figure 4.39 Incomplete desorption of 180 mg 80% wet ball milled MgH_2 at 300°C, Case I

The model is also evaluated for the wet ball milled MgH_2 powder with Nb_2O_5. The kinetic constant of 99mg wet ball milled MgH_2 powder with Nb_2O_5 with a specific surface area of 78.8m^2g^{-1} (after 72h milling by diameter 5mm YSZ balls) is $k_{Nb_2O_5,350°C} = 4.2 \cdot 10^{-12} mol/(m^2 \cdot s \cdot Pa)$ (see **Figure 4. 40a**) and the other 68mg sample

with 180.2m²g^{-1} (after 72h milling by diameter 5mm YSZ balls and another 24h milling by diameter 0.1mm YSZ balls) is $k'_{Nb_2O_5,350°C} = 8.4 \cdot 10^{-12} mol/(m^2 \cdot s \cdot Pa)$ (see **Figure 4. 40b**). It is found that the latter desorption kinetic constant, i.e. desorption rate is twice as large as that of the former situation, which is in accordance with that of the correlation between their specific surface area.

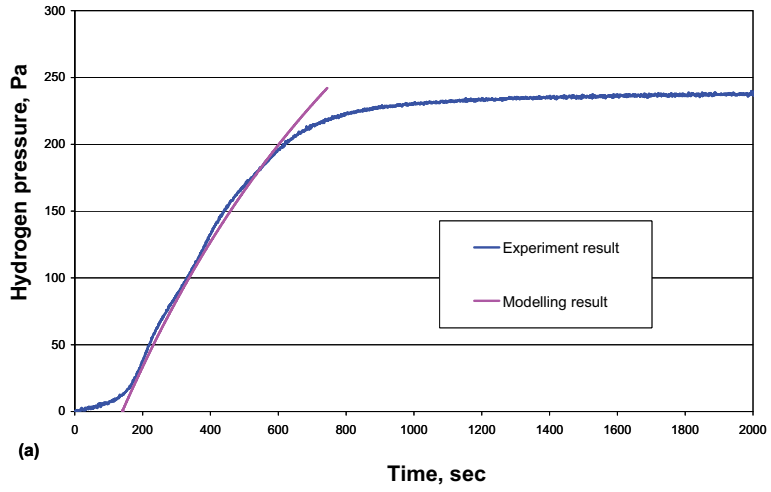

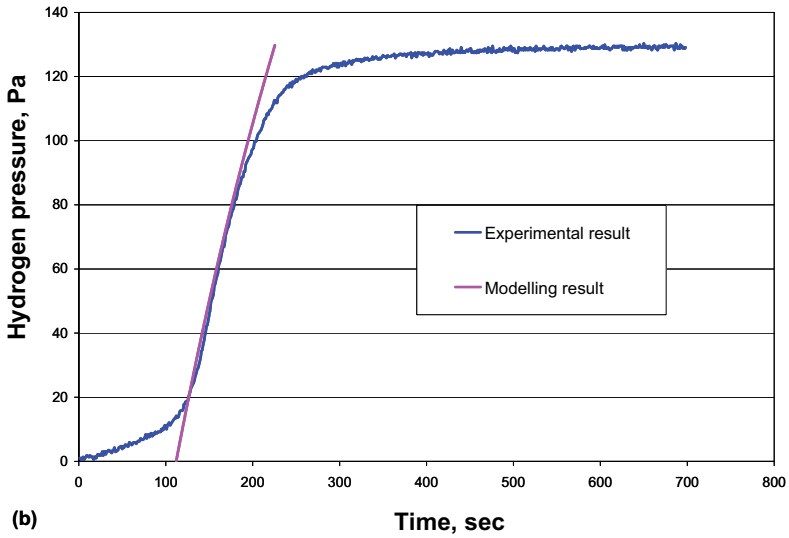

Figure 4. 40 (a) Desorption of 99mg 78% wet ball milled MgH_2 powder with 3wt%Nb_2O_5 at 350°C (after 72h milling by diameter 5mm YSZ balls), Case II; (b) Desorption of 68mg 61% wet ball milled MgH_2 powder with 3wt%Nb_2O_5 at 350°C (after 72h milling by diameter 5mm YSZ balls and another 24h milling by diameter 0.1mm YSZ balls), Case II;

However, this relationship was not found for the samples of wet ball milled without catalyst and with Nb_2O_5 (after 72h milling using 5mm YSZ balls). Here the improved kinetic constant might be related to the effect of Nb_2O_5 as discussed above (see **Figure 4.41**).

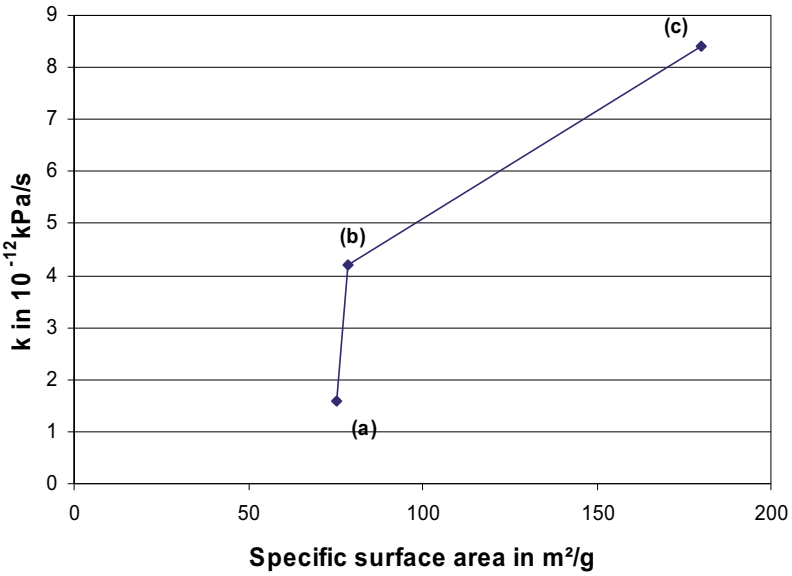

Figure 4.41 Relationship between specific surface area and the desorption rate at 350°C of (a) standard wet ball milled MgH_2 powder; (b) standard wet ball milled MgH_2 with 3wt%Nb_2O_5 and (c) improved wet ball milled MgH_2 with 3wt%Nb_2O_5.

4.4 Hydrogen sorption of $NaAlH_4$

The purpose of this work is to investigate the effects of wet ball milling on hydrogen desorption/absorption of $NaAlH_4$. In this work the same treatment as for MgH_2 powder, i.e. dry ball milling and wet ball milling were used for $NaAlH_4$. The hydrogen desorption behaviour of three different $NaAlH_4$ powder is shown in **Figure 4. 42.**

From **Figure 4. 42a** it was shown that the as-received $NaAlH_4$ powder could only desorb about 3wt% of hydrogen after 500min at 230°C, which proves that probably only the 1st desorption step occurred (see **Chapter 2.2.5**) for the as-received powder. In contrast the higher amount of released hydrogen in **Figure 4. 42b and c** indicated

that both the 1st and 2nd desorption steps might take place in the dry and wet ball milled $NaAlH_4$ powder. In addition, the wet ball milled $NaAlH_4$ powder showed a higher desorption kinetics than dry ball milled $NaAlH_4$ powder. However, for desorption temperature lower than 200°C no more hydrogen desorption behavior for all three kinds of $NaAlH_4$ powder was found. That means even after wet ball milling, the desorption temperature of $NaAlH_4$ powder cannot be decreased below the melting point of $NaAlH_4$ powder (~183°C [94]).

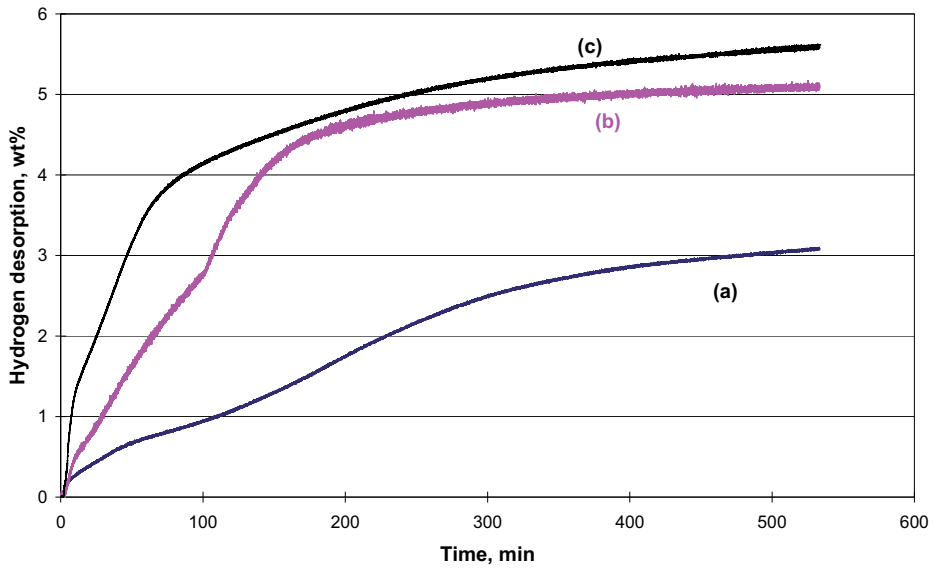

Figure 4. 42 Hydrogen desorption at 230°C of (a) as-received $NaAlH_4$ powder, (b) dry ball milled $NaAlH_4$ powder and (c) wet ball milled $NaAlH_4$ powder.

For the above desorbed $NaAlH_4$ powders, absorption experiments were performed with the initial hydrogen pressure of 12MPa at 230°C. No absorption was found. So no benefit from wet ball milling on the hydrogen sorption behavior is seen.

A hydrogen storage material with a release process consisting of several steps might not be suitable for the optimization by milling.

Chapter 5 Summary of the conclusions

Through comparison of the different milling parameters on the suspension particle size, the optimal milling parameters in this work were: 20wt% of MgH_2 in the its THF suspension, 10:1 as the milling BPR, 5mm diameter YSZ balls as the ball milling medium and 72h as the milling time.

Compared to as-received and dry ball milled MgH_2 powder, wet ball milled MgH_2 powder had much finer particle size and larger specific surface area. Their sorption behaviour showed that wet ball milled MgH_2 powder had much higher kinetic at different sorption temperatures, especially at relatively low temperatures. It is concluded that decrease of particle size and large increase of specific surface area due to wet ball milling result in an improvement of sorption kinetics of MgH_2 powder. The kinetic improvement of cyclic desorption and absorption was also advantageous of wet ball milling. The desorption kinetics of wet ball milled MgH_2 powder was improved since 2^{nd} cycle. Although the maximal desorption capacity decreased from 1^{st} to 2^{nd} cycle (from 7wt% to 6wt%), it kept the same from 2^{nd} to 10^{th} cycle. While the absorption kinetics and capacity continuously improved from 1^{st} to 10^{th} cycle. Why the 1^{st} cyclic desorption kinetics was much slower than the other cycles was explained that during wet ball milling, part of MgH_2 powder top surface could not avoid to be oxidized, which blocked the hydrogen sorption from the top surface. After 1^{st} cyclic desorption, the surface of MgH_2 powder was activated thus the sorption kinetic was improved quite a lot. Besides, based on their P-C-T curves and Van't Hoff plots different MgH_2 powders showed similar formation enthalpy and entropy. It was again proved that the enhancement of sorption behaviour of MgH_2 was only from the kinetic improvement due to wet ball milling.

In this work, three different catalysts, i.e. Nb_2O_5, V and CNTs were used as catalysts. For hydrogen desorption, Nb_2O_5 and CNTs showed the better influence on its kinetic, while for hydrogen absorption Nb_2O_5 and V improved its kinetics more strongly than CNTs. Combination of improvement desorption and absorption, Nb_2O_5 was the best catalysts in this work. Compared to the wet ball milled MgH_2 powder,

the catalysts the powder had similar particle size and specific surface area but finer grain size. Thus the reasons why catalysts improved hydrogen sorption kinetics were expected as: (1) decrease of grain size resulted in improvement of the sorption kinetic of wet ball milled MgH_2; (2) from literature it was shown that formation of Mg-Nb-O supported the diffusion in the MgH_2 bulk and in the surface. This could be also used to explain the results of the other two catalysts. The partial Mg was lost for hydrogen sorption due to formation of new oxides thus its hydrogen capacity was lower than MgH_2 powder without catalysts. Besides, its cyclic sorption kinetics was also improved due to added catalyst as expected.

Based on the above wet ball milled MgH_2 powder with Nb_2O_5 catalyst, another 24h milling was operated by diameter 0.1mm YSZ milling balls in order to improve its microstructure. After the further ball milling, the specific surface area of the wet ball milled MgH_2 powder was largely increased from 78.78m^2/g to 180.16m^2/g. From the comparison of hydrogen desorption at 300°C and 350°C the desorption kinetics of the new wet ball milled MgH_2 with 3wt%Nb_2O_5 powder was 2.6 and 2.8 times as large as that of the previous standard wet ball milled MgH_2 with 3wt%Nb_2O_5 powder. It was once again proved that the specific surface area was the key microstructural parameter for hydrogen sorption kinetics.

With this characteristics, the model of MgH_2 desorption was built up and the modelling results were in accordance with experimental results quite well.

Another metal complex hydride $NaAlH_4$ was also used in this work for hydrogen storage. However, its desorption temperature is higher than its melting point. The improved microstructure due to wet ball milling cannot play a role on improvement of the desorption behaviour of molten $NaAlH_4$.

In a word, due to the MgH_2 powder, it is found that through wet ball milling with the help of THF the particle size was largely decreased and surface area was enormously enlarged, which were important for enhancement of the sorption kinetics. However, this optimization was only valid for the storage material having the desorption temperature lower than the melting temperature but not for the material

with several releasing processes and desorption temperature higher than the melting temperature.

Reference

[1] Energy Information Administration (EIA), Primary Energy Consumption by Source, 1949-2008 (http://www.eia.doe.gov/emeu/aer/txt/ptb0103.html).

[2] BP Distribution Services, BP Statistical Review of World Energy 2004 (June 2004).

[3] D.A.J. Rand, R.M.Dell, Hydrogen Energy Challenges and Prospects, RSC Publishing.

[4] L.Schlapbach, A.Züttel, Nature 2001, 414, 353-358.

[5] A.Züttel, Naturwissenschaften 2004, 91, 157-172.

[6] D.R.Lide CRC Handbook of Chemistry and Physics (ed. Lide, D. R.) (CRC Press, Boca Raton, 2005).

[7] G.Sandrock, J. Alloys Compd.1999, 295, 877-888.

[8] A.Züttel, A.Borgschulte, L.Schlapbach, Hydrogen as a Future Energy Carrier, Wiley-VCH.

[9] M.Grätzel, Nature 2001, 414, 338-344.

[10] R.W.P.Wagemans, Magnesium for hydrogen storage from micrometer to nanometer, 2006.

[11] I.Chorkendorff, J.W.Niemantsverdriet, Concepts of modern catalysis and kinetics, Wiley-VCH, 2003.

[12] B.C.H.Steele, A.Heinzel, Nature 2001, 414, 345-352.

[13 http://en.wikipedia.org/wiki/Internal_combustion_engine

[14] Review of the Research Program of the FreedomCAR and Fuel Partnership: First Report, The National Academies Press, 2005.

[15] International Partnership for the Hydrogen Economy, Hydrogen storage. http://www.iphe.net/docs/Fact_Sheets/Hydrogen_Storage.pdf

[16] Targets for on-board hydrogen storage systems: Current R&D focus is on 2010 Targets

http://www1.eere.energy.gov/hydrogenandfuelcells/pdfs/freedomcar_targets_explanations.pdf

[17] Hydrogen fuel Production, Transport, and Storage (ed. R.B.Gupta) (CRC Press, Boca Raton, 2008).

[18] A.F.Burke, M. Gardiner, Hydrogen Storage Options: Technologies and Comparisons for Light-duty Vehicle Applications, Research Report UCD-ITS-RR-05-01, Institute of Transportation Studies, University of California, Davis, 2005.

[19] A.Züttel, Materials for hydrogen storage, Materials Today, 2003 September.

[20] G.Arnold, Advanced Hydrogen Storage Technologies, General Motors Hydrogen Storage and Refueling, Global Alternative Propulsion Center, Mainz-Kastel, Germany.

[21] W.B.Leung, N.H.March and H.Motz, Physical Letters 1976, 56a, 425-426.

[22] P.Selvam, B.Viswanathan, C.S.Swamy, V.Srinivasan, Int. J. Hydrogen Energy 1986, 11, 169-192.

[23] A.M.Seayad, D.M.Antonelli, Adv. Mater. 2004, 16, 765-777 (a review).

[24] N.Gerard, S.Ono, Hydride formation and decomposition kinetics, in: L.Schlapbach (Ed.), Hydrogen in Intermetallic Comounds II, Springer-Verlag, Berlin, 1992.

[25] J.Rowsell, A.Millward, K.Park, O.Yaghi, J. Am. Chem. Soc. 2004, 126, 5666–5667.

[26] J.Rowsell, E. Spencer, J. Eckert, J. Howard, O. Yaghi, Gas adsorption sites in a large pore metal–organic framework, Science 2005, 309, 1350–1354.

[27] A.C.Dillon, P.A.Parilla, Y.Zhao, Y.-H.Kim, T.Genett, C.Curtis, J.L.Blackburn, K.E.H.Gilbert, J.L.Alleman, K.M.Jones, S.B.Zhang and M.J.Heben, The 2005 U.S. Department of Energy Hydrogen Program Review, May 23-26, 2005.

[28] A.C.Dillon, K.M.Jones, T.A.Bekkedahl, C.H.Kiang, D.S.Bethune and M.J.Heben, Nature, 1997, 386, 377-379.

[29] J.Schwarz, Activated carbon-based hydrogen storage system, 1993 DOE/NREL Hydrogen Program Review 1993, 89–102.

[30] Category: Metal hydrides http://en.wikipedia.org/wiki/Category:Metal_hydrides

[31] J.E Lennard-Jones, Trans. Faraday Soc. 1932, 28, 333.

[32] K.R.Christmann, Surf. Sci. Rep., 1988, 9, 1.

[33] A.Züttel, in H2net seminar, University of Birmingham, Birmingham, 2004.

[34] K.Christmann, Z. Phys. Chem. NF, 1987, 154, 145.

[35] J.K.Norskov, Physica, 1984, B127, 193. Phys. Rev. B, 1982, 26, 2875.;
J.K.Norskov, F.Besenbacher, J. Less-Common Met., 1987, 130, 475.

[36] M.Strongin, J.Colbert, G.J.Dienes, D.O.Welch, Phys. Rev. B, 1982, 26, 2715.

[37] M.Martin, C.Gommel, C.Borkhart, E.Fromm, J. Alloys. Compd., 1996, 238, 193.

[38] S.A.Jin, J.H.Shim, J.P.Ahn, Y.W.Cho, K.W.Yi, Acta Mater. 2007, 55, 5073.

[39] G.Liang, J.Huot, S.Boily, A.Van Neste, R.Schulz, J. Alloys Compd. 1999, 292, 247.

[40] J. F. Stampfer, C. E. Holley, J. F. Suttle, J. Am. Chem. Soc. 1960, 82, 3504.

[41] A. Zaluska, L. Zaluska, J. O. Ström-Olsen, Appl. Phys. A, 2001, 72, 157.

[42] J. J. Reilly, R. H. Wiswall, Inorg. Chem. 1968, 7, 2254.

[43] Solid –state hydrogen storage Materials and chemistry (Ed. Gavin Walker), CRS Press.

[44] T.Noritake, M.Alki, S.Towata, Y.Seno, E.Nishibori, M.Takata and M.Sakata, Applied Physicas Letter, 2008-2010, 81.

[45] J.P.Bastide, B.Bonnetot, J.M.Letoffe and P.Claudy, Materials Research Bulletin, 1980, 6, 285-294.

[46] K.N.Semenenko, V.N.Verbestkii, Y.A.Kalashnikov, N.V.Temofeeva and M.I.Ioffe, Phase transitions of metal hydrides under condition of superhigh pressure, Vest. Mosk. Univ. Ser.2, Khim., 1978, 19, 718-722.

[47] R.B. Gupta, Hydrogen fuel production, transport, and storage. CRC Press, Taylor & Francis Group.

[48] B.Bogdanovic, R.A.Brand, A.Marianovic, M.Schwickardi, J.Tölle, J.Alloys Compd. 2000, 302, 36-58.

[49] B. Bagdanovic, M. Schwickardi, J. Alloys Compd. 1997, 253/254, 1-9.

[50] R.A.Zidan, S.Takara, A.G. Hee, C.M. Jensen J. Alloys Compd. 1999, 285, 119-22.

[51] C. M. Jensen and K. J. Gross, Appl. Phys. A, 2001, 72, 213-19.

[52] A.Zaluska, L.Zaluski and J.O.Ström-Olsen, J. Alloys Compd. 2000, 298, 125-34.

[53] K.J.Gross, G.J.Thomas, C.M. Jensen, J. Alloys Compd, 2002, 330-332, 683-90.

[54] D.L.Anton, 2003 Catalytic effect of transition metal additions to NaAlH4 for hydrogen desorption Proc. Int. Symp. on Metal Hydrogen Systems (Annecy, France, Sept. 2002); J. Alloys Compounds at press.

[55] M.Avrami, J. Chem. Phys. 1939, 7, 1103.

[56] W.A.Johnson, R.F.Mehl, Trans. Am. Inst. Min. Metall. Pet. Eng. 1939, 135, 416.

[57] P.S.Rudman, J. Appl. Phys. 1979, 50, 7195.

[58] M.H.Mintz, Y.Zeeri, J. Alloys Compd. 1994, 216, 159.

[59] F.J.Castro, G.Meyer, J. Alloys Compd. 2002, 330-332, 59.

[60] G.Barkhordarian, T.Klassen, R.Bormann, J. Alloys. Compd. 2006, 407, 249-255.

[61] J.Avrami, I , J. Chem. Phys. 1939, 7,1103; J. Chem. Phys. 1940, 8, 212, J. Chem. Phys. 1941,9,177.

[62] K.C.Chou, K.Xu, Intermetallics, 2007, 15, 767-777.

[63] R.A.Varin and T.Czujko, Mater. & Manufacturing Processes 2002, 17, 129.

[64] C.Suryanarayana, Progress in Materials Science 2001,46,1-184.

[65] L.M. Di, H Bakker. J. Phys. C: Condens Matter 1991, 3, 3427-32.

[66] S.D Kaloshkin, I.ATomlin, G.A.Andrianov, U.V.Baldokhin, E.V.Shelekhov, Mater. Sci. Forum 1997, 235-238, 565-70.

[67] C.Kuhrt, H. Schultz, E. Arzt. In: J.J. deBarbadillo, et al., editors. Mechanical alloying for structural applications. Materials Park, OH: ASM International, 1993. 269-73.

[68] C. Suryanarayana, Intermetallics 1995, 3, 153-60.

[69] http://en.wikipedia.org/wiki/N-hexane

[70] http://en.wikipedia.org/wiki/THF

[71] http://www.cem.msu.edu/~reusch/VirtualText/enrgtop.htm#top4

[72] http://en.wikipedia.org/wiki/Rheometer

[73]http://www.labcompare.com/32-Particle-Size-Analyzer-Particle-Analyzers-Particle-Sizer/597-LB-550-Dynamic-Light-Scattering-Nano-Analyzer/

[74] G.K.Williamson, W.H.Hall, Acta Metall. 1953, 1, 22.

[75] J.P.Bastide, B.Bonnetot, J.M.Létoffé, Mater. Res. Bull. 1980, 15, 1779.

[76] J.Huot, G.Liang, S.Boily, A.Van Neste, R.Schulz, J. Alloys Compds. 1999, 293-295, 495.

[77] J.P.Bastide, B.Bonnetot, J.M.Létoffe, P.Claudy, Mater. Res. Bull 1980, 15, 1215.

[78] J.J.Reilly, Jr.R.H.Wiswall, Inorg. Chem. 1968,7,2254.

[79] B.Tanguy, J.L.Soubeyroux, M.Pezat, J.Portier, P.Hagenmuller, Mater. Res. Bull 1976, 11, 1441.

[80] G.Liang, J.Huot, S.Boily, A.V.Neste, R.Schulz, J. Alloys Compd. 1999, 291, 295.

[81] P.C.H. Mitchell, A.J.Ramirez-Cuesta, S.F. Parker, J. Tomkinson and D. Thompsett, Journal Physical Chemistry B, 2003, 107, 6838-6845.

[82] G.K.Williamson, W.H. Hall. Acta Metall 1953, 1, 22-23.

[83] Network Scientific Highlights (3rd Year and Final Report) and http://www.inpg.fr/RTN-MgH2/

[84] O.Friedrichs, J.C.Sánchez-López, C.López-Cartes, T.klassen, R.Bormann, and A.Fernández, J. Phys. Chem. B 2006, 110, 7845-7850.

[85] K.S. Jung et al., Hydrogen sorption of magnesium hydride doped with nano-sized TiO2, Catal. Today (2006), doi: 10.1016/j. cattod.2006.09.028.

[86] C.Z.Wu, P.Wang, X.Yao et a.l, J. Alloys. Compd. 2006, 420, 278-282.

[87] Á.Révész, D.Fátay, T.Spassov, J. Alloys. Compd. 2007, 434-435, 725-728.

[88] H.Imamura, K.Masanari, M.Kusuhara et al., J. Alloys. Compd. 2005, 386, 211-216.

[89] Z.Dehouche, R.Djaozandry, J.Huot et al., J. Alloys. Compd. 2000, 305, 264-271.

[90] K.F.Aguey-Zinsou, J.R.Ares Fernandez, T.Klassen, R.Bormann, Int. J. Hydrogen Energy 2007, 32, 2400-2407.

[91] Solid-state hydrogen storage materials and chemistry, Edited by Gavin Walker. Woodhead publishing in materials.

[92] J.Renner, H.J.Grabke, Zeitficat f. Metallkunde 1978, 68, 639.

[93] C.Nishimura, M.Komaki, M.Amano. J. Alloys. Compd. 1999, 293-295, 329-333.

[94] R.T.Walters, J.H.Scogin, A reversible mechanism for sodium alanate: the role alanes and the catalytic effect of the dopant (U), WSRC-MS-2004-00099.

Acknowledge

This Ph.D work has been done in Forschungszentrum Jülich in the Institute of Energy and Climate Research (IEK-1: Materials Synthesis and Processing) during the period from Dec. 2006 to Nov. 2009.

At the first I would like to thank Prof. Dr. Detlev Stöver to be my Doctor Father and gave me chance to work in IEK-1.

I appreciate Prof. Dr. Robert Vaßen to select such an interesting and challenging topic for my last 3 years Ph.D work. During the whole period he gave me quite systematic and continuous guide of the topics as well as the field of material science. When I met any problem during my experiments and discussion, he was always patient to give me suggestions and helped me to solve the problems. Thank him to train me to become a real scientist.

I am quite grateful to Dr. Georg Mauer for his continuous and thorough support and help during my Ph.D work. Thank him for guiding me to organize my experimental plans; guiding me how to avoid the failures during experiments; correcting my quarter reports and papers, and training me to improve my English writing and oral skills. With his help I was successful with my last 3 years of Ph.D work and final examination.

I would like to thank Dr. Igor Drozdov for his kind discussion and hard working to build up the modeling for hydrogen sorption kinetics calculation.

I thank Dr. Holger Kaßer and Oliver Büchler for the help at the beginning of my experiment and guiding me familiar with the regulations of labs and instruments. I appreciate Dr. Maria Ophelia Jarligo and Alesandre Guignard for their help to supply me quite a lot of knowledge and experimental experience about material science as well as their discussion with me about my experiments and results.

I appreciate Dr. Werner Fischer and Mirko Ziegner for XRD experiments and their professional support for the result analysis. Thank Dr. Doris Sebold for the SEM pictures as well as the suggestions for the safety regulations during experiments.

Sigrid Schwartz-Lückge is thanked due to her help for test of specific surface area and Nicole Adels and Andrea Hilgers are appreciated for their support during particle size and viscosity measurements.

I want to also thank Dr. Stefan. Baumann, Andrea Hilgers for their help during working with BELSORP-HP. Rauwald Karl-Heinz is thanked for his quite a lot of help for changing the heavy argon bottles, repairing the vacuum pump and other technical help.

Special thanks to Mr. Dirk Meister from Rubotherm Präzisionsmesstechnik GmbH as well as his Japanese colleges for his great technical support on the usage of BEL-SORP and analysis of the isothermal desorption results.

I appreciate quite a lot Vicky Rostin, Stefan Weitz, Hannelore Rüther, Marlene Pionke and Marianne Meyer for their support of organization and administration during my working period. For the help of computer problems I would like to thank Björb Lambertz and Stephan. Giesen.

I would like to thank especially the Chinese colleagues, Qianli Ma, Ye Xing, Feng Han, Wen Ma, Yanfei Zhang, Yi Zeng, Linnan Du for their grateful support for experiments discussion, Chinese communication and for great help for the private problems, like movement, auto reparation.

Finally I would like to thank my boyfriend Nan Meng for his support and help in all the aspects of my work and life in the last 2 years. Without him I could not successfully graduate and get the new job as expected. I want to deeply thank my father and mother, who keep quite often communication with me and let me always feel I am quite happy and lucky. Thank them during the whole period of my study in Germany whatever problems I met they always tried their best to support and help me.

1. **Einsatz von multispektralen Satellitenbilddaten in der Wasserhaushalts- und Stoffstrommodellierung – dargestellt am Beispiel des Rureinzugsgebietes**
   von C. Montzka (2008), XX, 238 Seiten
   ISBN: 978-3-89336-508-1

2. **Ozone Production in the Atmosphere Simulation Chamber SAPHIR**
   by C. A. Richter (2008), XIV, 147 pages
   ISBN: 978-3-89336-513-5

3. **Entwicklung neuer Schutz- und Kontaktierungsschichten für Hochtemperatur-Brennstoffzellen**
   von T. Kiefer (2008), 138 Seiten
   ISBN: 978-3-89336-514-2

4. **Optimierung der Reflektivität keramischer Wärmedämmschichten aus Yttrium-teilstabilisiertem Zirkoniumdioxid für den Einsatz auf metallischen Komponenten in Gasturbinen**
   von A. Stuke (2008), X, 201 Seiten
   ISBN: 978-3-89336-515-9

5. **Lichtstreuende Oberflächen, Schichten und Schichtsysteme zur Verbesserung der Lichteinkopplung in Silizium-Dünnschichtsolarzellen**
   von M. Berginski (2008), XV, 171 Seiten
   ISBN: 978-3-89336-516-6

6. **Politikszenarien für den Klimaschutz IV – Szenarien bis 2030**
   hrsg.von P. Markewitz, F. Chr. Matthes (2008), 376 Seiten
   ISBN 978-3-89336-518-0

7. **Untersuchungen zum Verschmutzungsverhalten rheinischer Braunkohlen in Kohledampferzeugern**
   von A. Schlüter (2008), 164 Seiten
   ISBN 978-3-89336-524-1

8. **Inorganic Microporous Membranes for Gas Separation in Fossil Fuel Power Plants**
   by G. van der Donk (2008), VI, 120 pages
   ISBN: 978-3-89336-525-8

9. **Sinterung von Zirkoniumdioxid-Elektrolyten im Mehrlagenverbund der oxidkeramischen Brennstoffzelle (SOFC)**
   von R. Mücke (2008), VI, 165 Seiten
   ISBN: 978-3-89336-529-6

10. **Safety Considerations on Liquid Hydrogen**
    by K. Verfondern (2008), VIII, 167 pages
    ISBN: 978-3-89336-530-2

11. **Kerosinreformierung für Luftfahrtanwendungen**
von R. C. Samsun (2008), VII, 218 Seiten
ISBN: 978-3-89336-531-9

12. **Der 4. Deutsche Wasserstoff Congress 2008 – Tagungsband**
hrsg. von D. Stolten, B. Emonts, Th. Grube (2008), 269 Seiten
ISBN: 978-3-89336-533-3

13. **Organic matter in Late Devonian sediments as an indicator for environmental changes**
by M. Kloppisch (2008), XII, 188 pages
ISBN: 978-3-89336-534-0

14. **Entschwefelung von Mitteldestillaten für die Anwendung in mobilen Brennstoffzellen-Systemen**
von J. Latz (2008), XII, 215 Seiten
ISBN: 978-3-89336-535-7

15. **RED-IMPACT**
Impact of Partitioning, Transmutation and Waste Reduction Technologies on the Final Nuclear Waste Disposal
SYNTHESIS REPORT
ed. by W. von Lensa, R. Nabbi, M. Rossbach (2008), 178 pages
ISBN 978-3-89336-538-8

16. **Ferritic Steel Interconnectors and their Interactions with Ni Base Anodes in Solid Oxide Fuel Cells (SOFC)**
by J. H. Froitzheim (2008), 169 pages
ISBN: 978-3-89336-540-1

17. **Integrated Modelling of Nutrients in Selected River Basins of Turkey**
Results of a bilateral German-Turkish Research Project
project coord. M. Karpuzcu, F. Wendland (2008), XVI, 183 pages
ISBN: 978-3-89336-541-8

18. **Isotopengeochemische Studien zur klimatischen Ausprägung der Jüngeren Dryas in terrestrischen Archiven Eurasiens**
von J. Parplies (2008), XI, 155 Seiten, Anh.
ISBN: 978-3-89336-542-5

19. **Untersuchungen zur Klimavariabilität auf dem Tibetischen Plateau - Ein Beitrag auf der Basis stabiler Kohlenstoff- und Sauerstoffisotope in Jahrringen von Bäumen waldgrenznaher Standorte**
von J. Griessinger (2008), XIII, 172 Seiten
ISBN: 978-3-89336-544-9

20. **Neutron-Irradiation + Helium Hardening & Embrittlement Modeling of 9%Cr-Steels in an Engineering Perspective (HELENA)**
by R. Chaouadi (2008), VIII, 139 pages
ISBN: 978-3-89336-545-6

21. **in Bearbeitung**

22. **Verbundvorhaben APAWAGS (AOEV und Wassergenerierung) – Teilprojekt: Brennstoffreformierung – Schlussbericht**
von R. Peters, R. C. Samsun, J. Pasel, Z. Porš, D. Stolten (2008), VI, 106 Seiten
ISBN: 978-3-89336-547-0

23. **FREEVAL**
Evaluation of a Fire Radiative Power Product derived from Meteosat 8/9 and Identification of Operational User Needs
Final Report
project coord. M. Schultz, M. Wooster (2008), 139 pages
ISBN: 978-3-89336-549-4

24. **Untersuchungen zum Alkaliverhalten unter Oxycoal-Bedingungen**
von C. Weber (2008), VII, 143, XII Seiten
ISBN: 978-3-89336-551-7

25. **Grundlegende Untersuchungen zur Freisetzung von Spurstoffen, Heißgaschemie, Korrosionsbeständigkeit keramischer Werkstoffe und Alkalirückhaltung in der Druckkohlenstaubfeuerung**
von M. Müller (2008), 207 Seiten
ISBN: 978-3-89336-552-4

26. **Analytik von ozoninduzierten phenolischen Sekundärmetaboliten in *Nicotiana tabacum* L. cv Bel W3 mittels LC-MS**
von I. Koch (2008), III, V, 153 Seiten
ISBN 978-3-89336-553-1

27. **IEF-3 Report 2009. Grundlagenforschung für die Anwendung**
(2009), ca. 230 Seiten
ISBN: 978-3-89336-554-8

28. **Influence of Composition and Processing in the Oxidation Behavior of MCrAlY-Coatings for TBC Applications**
by J. Toscano (2009), 168 pages
ISBN: 978-3-89336-556-2

29. **Modellgestützte Analyse signifikanter Phosphorbelastungen in hessischen Oberflächengewässern aus diffusen und punktuellen Quellen**
von B. Tetzlaff (2009), 149 Seiten
ISBN: 978-3-89336-557-9

30. **Nickelreaktivlot / Oxidkeramik – Fügungen als elektrisch isolierende Dichtungskonzepte für Hochtemperatur-Brennstoffzellen-Stacks**
von S. Zügner (2009), 136 Seiten
ISBN: 978-3-89336-558-6

31. **Langzeitbeobachtung der Dosisbelastung der Bevölkerung in radioaktiv kontaminierten Gebieten Weißrusslands – Korma-Studie**
von H. Dederichs, J. Pillath, B. Heuel-Fabianek, P. Hill, R. Lennartz (2009), Getr. Pag.
ISBN: 978-3-89336-532-3

32. **Herstellung von Hochtemperatur-Brennstoffzellen über physikalische Gasphasenabscheidung**
von N. Jordán Escalona (2009), 148 Seiten
ISBN: 978-3-89336-532-3

33. **Real-time Digital Control of Plasma Position and Shape on the TEXTOR Tokamak**
by M. Mitri (2009), IV, 128 pages
ISBN: 978-3-89336-567-8

34. **Freisetzung und Einbindung von Alkalimetallverbindungen in kohlebefeuerten Kombikraftwerken**
von M. Müller (2009), 155 Seiten
ISBN: 978-3-89336-568-5

35. **Kosten von Brennstoffzellensystemen auf Massenbasis in Abhängigkeit von der Absatzmenge**
von J. Werhahn (2009), 242 Seiten
ISBN: 978-3-89336-569-2

36. **Einfluss von Reoxidationszyklen auf die Betriebsfestigkeit von anodengestützten Festoxid-Brennstoffzellen**
von M. Ettler (2009), 138 Seiten
ISBN: 978-3-89336-570-8

37. **Großflächige Plasmaabscheidung von mikrokristallinem Silizium für mikromorphe Dünnschichtsolarmodule**
von T. Kilper (2009), XVII, 154 Seiten
ISBN: 978-3-89336-572-2

38. **Generalized detailed balance theory of solar cells**
by T. Kirchartz (2009), IV, 198 pages
ISBN: 978-3-89336-573-9

39. **The Influence of the Dynamic Ergodic Divertor on the Radial Electric Field at the Tokamak TEXTOR**
von J. W. Coenen (2009), xii, 122, XXVI pages
ISBN: 978-3-89336-574-6

40. **Sicherheitstechnik im Wandel Nuklearer Systeme**
von K. Nünighoff (2009), viii, 215 Seiten
ISBN: 978-3-89336-578-4

41. **Pulvermetallurgie hochporöser NiTi-Legierungen für Implanat- und Dämpfungsanwendungen**
von M. Köhl (2009), XVII, 199 Seiten
ISBN: 978-3-89336-580-7

42. **Einfluss der Bondcoatzusammensetzung und Herstellungsparameter auf die Lebensdauer von Wärmedämmschichten bei zyklischer Temperaturbelastung**
von M. Subanovic (2009), 188, VI Seiten
ISBN: 978-3-89336-582-1

43. **Oxygen Permeation and Thermo-Chemical Stability of Oxygen Permeation Membrane Materials for the Oxyfuel Process**
by A. J. Ellett (2009), 176 pages
ISBN: 978-3-89336-581-4

44. **Korrosion von polykristallinem Aluminiumoxid (PCA) durch Metalljodidschmelzen sowie deren Benetzungseigenschaften**
von S. C. Fischer (2009), 148 Seiten
ISBN: 978-3-89336-584-5

45. **IEF-3 Report 2009. Basic Research for Applications**
(2009), 217 Seiten
ISBN: 978-3-89336-585-2

46. **Verbundvorhaben ELBASYS (Elektrische Basissysteme in einem CFK-Rumpf) - Teilprojekt: Brennstoffzellenabgase zur Tankinertisierung - Schlussbericht**
von R. Peters, J. Latz, J. Pasel, R. C. Samsun, D. Stolten
(2009), xi, 202 Seiten
ISBN: 978-3-89336-587-6

47. **Aging of ^{14}C-labeled Atrazine Residues in Soil: Location, Characterization and Biological Accessibility**
by N. D. Jablonowski (2009), IX, 104 pages
ISBN: 978-3-89336-588-3

48. **Entwicklung eines energetischen Sanierungsmodells für den europäischen Wohngebäudesektor unter dem Aspekt der Erstellung von Szenarien für Energie- und CO_2 - Einsparpotenziale bis 2030**
von P. Hansen (2009), XXII, 281 Seiten
ISBN: 978-3-89336-590-6

49. **Reduktion der Chromfreisetzung aus metallischen Interkonnektoren für Hochtemperaturbrennstofzellen durch Schutzschichtsysteme**
von R. Trebbels (2009), iii, 135 Seiten
ISBN: 978-3-89336-591-3

50. **Bruchmechanische Untersuchung von Metall / Keramik-Verbundsystemen für die Anwendung in der Hochtemperaturbrennstoffzelle**
von B. Kuhn (2009), 118 Seiten
ISBN: 978-3-89336-592-0

51. **Wasserstoff-Emissionen und ihre Auswirkungen auf den arktischen Ozonverlust**
Risikoanalyse einer globalen Wasserstoffwirtschaft
von T. Feck (2009), 180 Seiten
ISBN: 978-3-89336-593-7

52. **Development of a new Online Method for Compound Specific Measurements of Organic Aerosols**
by T. Hohaus (2009), 156 pages
ISBN: 978-3-89336-596-8

53. **Entwicklung einer FPGA basierten Ansteuerungselektronik für Justageeinheiten im Michelson Interferometer**
von H. Nöldgen (2009), 121 Seiten
ISBN: 978-3-89336-599-9

54. **Observation – and model – based study of the extratropical UT/LS**
by A. Kunz (2010), xii, 120, xii pages
ISBN: 978-3-89336-603-3

55. **Herstellung polykristalliner Szintillatoren für die Positronen-Emissions-Tomographie (PET)**
von S. K. Karim (2010), VIII, 154 Seiten
ISBN: 978-3-89336-610-1

56. **Kombination eines Gebäudekondensators mit H2-Rekombinatorelementen in Leichwasserreaktoren**
von S. Kelm (2010), vii, 119 Seiten
ISBN: 978-3-89336-611-8

57. **Plant Leaf Motion Estimation Using A 5D Affine Optical Flow Model**
by T. Schuchert (2010), X, 143 pages
ISBN: 978-3-89336-613-2

58. **Tracer-tracer relations as a tool for research on polar ozone loss**
by R. Müller (2010), 116 pages
ISBN: 978-3-89336-614-9

59. **Sorption of polycyclic aromatic hydrocarbon (PAH) to Yangtze River sediments and their components**
by J. Zhang (2010), X, 109 pages
ISBN: 978-3-89336-616-3

60. **Weltweite Innovationen bei der Entwicklung von CCS-Technologien und Möglichkeiten der Nutzung und des Recyclings von CO_2**
Studie im Auftrag des BMWi
von W. Kuckshinrichs et al. (2010), X, 139 Seiten
ISBN: 978-3-89336-617-0

61. **Herstellung und Charakterisierung von sauerstoffionenleitenden Dünnschichtmembranstrukturen**
von M. Betz (2010), XII, 112 Seiten
ISBN: 978-3-89336-618-7

62. **Politikszenarien für den Klimaschutz V – auf dem Weg zum Strukturwandel, Treibhausgas-Emissionsszenarien bis zum Jahr 2030**
hrsg. von P. Hansen, F. Chr. Matthes (2010), 276 Seiten
ISBN: 978-3-89336-619-4

63. **Charakterisierung Biogener Sekundärer Organischer Aerosole mit Statistischen Methoden**
von C. Spindler (2010), iv, 163 Seiten
ISBN: 978-3-89336-622-4

64. **Stabile Algorithmen für die Magnetotomographie an Brennstoffzellen**
von M. Wannert (2010), ix, 119 Seiten
ISBN: 978-3-89336-623-1

65. **Sauerstofftransport und Degradationsverhalten von Hochtemperaturmembranen für CO2-freie Kraftwerke**
von D. Schlehuber (2010), VII, 139 Seiten
ISBN: 978-3-89336-630-9

66. **Entwicklung und Herstellung von foliengegossenen, anodengestützten Festoxidbrennstoffzellen**
von W. Schafbauer (2010), VI, 164 Seiten
ISBN: 978-3-89336-631-6

67. **Disposal strategy of proton irradiated mercury from high power spallation sources**
by S. Chiriki (2010), xiv, 124 pages
ISBN: 978-3-89336-632-3

68. **Oxides with polyatomic anions considered as new electrolyte materials for solid oxide fuel cells (SOFCs)**
by O. H. Bin Hassan (2010), vii, 121 pages
ISBN: 978-3-89336-633-0

69. **Von der Komponente zum Stack: Entwicklung und Auslegung von HT-PEFC-Stacks der 5 kW-Klasse**
von A. Bendzulla (2010), IX, 203 Seiten
ISBN: 978-3-89336-634-7

70. **Satellitengestützte Schwerewellenmessungen in der Atmosphäre und Perspektiven einer zukünftigen ESA Mission (PREMIER)**
von S. Höfer (2010), 81 Seiten
ISBN: 978-3-89336-637-8

71. **Untersuchungen der Verhältnisse stabiler Kohlenstoffisotope in atmosphärisch relevanten VOC in Simulations- und Feldexperimenten**
von H. Spahn (2010), IV, 210 Seiten
ISBN: 978-3-89336-638-5

72. **Entwicklung und Charakterisierung eines metallischen Substrats für nanostrukturierte keramische Gastrennmembranen**
von K. Brands (2010), vii, 137 Seiten
ISBN: 978-3-89336-640-8

73. **Hybridisierung und Regelung eines mobilen Direktmethanol-Brennstoffzellen-Systems**
von J. Chr. Wilhelm (2010), 220 Seiten
ISBN: 978-3-89336-642-2

74. **Charakterisierung perowskitischer Hochtemperaturmembranen zur Sauerstoffbereitstellung für fossil gefeuerte Kraftwerksprozesse**
von S.A. Möbius (2010) III, 208 Seiten
ISBN: 978-3-89336-643-9

75. **Characterization of natural porous media by NMR and MRI techniques: High and low magnetic field studies for estimation of hydraulic properties**
by L.-R. Stingaciu (2010), 96 pages
ISBN: 978-3-89336-645-3

76. **Hydrological Characterization of a Forest Soil Using Electrical Resistivity Tomography**
by Chr. Oberdörster (2010), XXI, 151 pages
ISBN: 978-3-89336-647-7

77. **Ableitung von atomarem Sauerstoff und Wasserstoff aus Satellitendaten und deren Abhängigkeit vom solaren Zyklus**
von C. Lehmann (2010), 127 Seiten
ISBN: 978-3-89336-649-1

78. **18th World Hydrogen Energy Conference 2010 – WHEC2010 Proceedings**
Speeches and Plenary Talks
ed. by D. Stolten, B. Emonts (2010)
ISBN: 978-3-89336-658-3

78-1. **18th World Hydrogen Energy Conference 2010 – WHEC2010 Proceedings**
Parallel Sessions Book 1:
Fuel Cell Basics / Fuel Infrastructures
ed. by D. Stolten, T. Grube (2010), ca. 460 pages
ISBN: 978-3-89336-651-4

78-2. **18th World Hydrogen Energy Conference 2010 – WHEC2010 Proceedings**
Parallel Sessions Book 2:
Hydrogen Production Technologies – Part 1
ed. by D. Stolten, T. Grube (2010), ca. 400 pages
ISBN: 978-3-89336-652-1

78-3. **18th World Hydrogen Energy Conference 2010 – WHEC2010 Proceedings**
Parallel Sessions Book 3:
Hydrogen Production Technologies – Part 2
ed. by D. Stolten, T. Grube (2010), ca. 640 pages
ISBN: 978-3-89336-653-8

78-4. **18th World Hydrogen Energy Conference 2010 – WHEC2010 Proceedings**
Parallel Sessions Book 4:
Storage Systems / Policy Perspectives, Initiatives and Cooperations
ed. by D. Stolten, T. Grube (2010), ca. 500 pages
ISBN: 978-3-89336-654-5

78-5. **18th World Hydrogen Energy Conference 2010 – WHEC2010 Proceedings**
Parallel Sessions Book 5:
Stategic Analysis / Safety Issues / Existing and Emerging Markets
ed. by D. Stolten, T. Grube (2010), ca. 530 pages
ISBN: 978-3-89336-655-2

78-6. **18th World Hydrogen Energy Conference 2010 – WHEC2010 Proceedings**
Parallel Sessions Book 6:
Stationary Applications / Transportation Applications
ed. by D. Stolten, T. Grube (2010), ca. 330 pages
ISBN: 978-3-89336-656-9

78 Set (complete book series)

18th World Hydrogen Energy Conference 2010 – WHEC2010 Proceedings
ed. by D. Stolten, T. Grube, B. Emonts (2010)
ISBN: 978-3-89336-657-6

79. **Ultrafast voltex core dynamics investigated by finite-element micromagnetic simulations**
by S. Gliga (2010), vi, 144 pages
ISBN: 978-3-89336-660-6

80. **Herstellung und Charakterisierung von keramik- und metallgestützten Membranschichten für die CO_2-Abtrennung in fossilen Kraftwerken**
von F. Hauler (2010), XVIII, 178 Seiten
ISBN: 978-3-89336-662-0

81. **Experiments and numerical studies on transport of sulfadiazine in soil columns**
by M. Unold (2010), xvi, 115 pages
ISBN: 978-3-89336-663-7

82. **Prompt-Gamma-Neutronen-Aktivierungs-Analyse zur zerstörungsfreien Charakterisierung radioaktiver Abfälle**
von J.P.H. Kettler (2010), iv, 205 Seiten
ISBN: 978-3-89336-665-1

83. **Transportparameter dünner geträgerter Kathodenschichten der oxidkeramischen Brennstoffzelle**
von C. Wedershoven (2010), vi, 137 Seiten
ISBN: 978-3-89336-666-8

84. **Charakterisierung der Quellverteilung von Feinstaub und Stickoxiden in ländlichem und städtischem Gebiet**
von S. Urban (2010), vi, 211 Seiten
ISBN: 978-3-89336-669-9

85. **Optics of Nanostructured Thin-Film Silicon Solar Cells**
by C. Haase (2010), 150 pages
ISBN: 978-3-89336-671-2

86. **Entwicklung einer Isolationsschicht für einen Leichtbau-SOFC-Stack**
von R. Berhane (2010), X, 162 Seiten
ISBN: 978-3-89336-672-9

87. **Hydrogen recycling and transport in the helical divertor of TEXTOR**
by M. Clever (2010), x, 172 pages
ISBN: 978-3-89336-673-6

88. **Räumlich differenzierte Quantifizierung der N- und P-Einträge in Grundwasser und Oberflächengewässer in Nordrhein-Westfalen unter besonderer Berücksichtigung diffuser landwirtschaftlicher Quellen**
von F. Wendland et. al. (2010), xii, 216 Seiten
ISBN: 978-3-89336-674-3

89. **Oxidationskinetik innovativer Kohlenstoffmaterialien hinsichtlich schwerer Lufteinbruchstörfälle in HTR´s und Graphitentsorgung oder Aufarbeitung**
von B. Schlögl (2010), ix, 117 Seiten
ISBN: 978-3-89336-676-7

90. **Chemische Heißgasreinigung bei Biomassenvergasungsprozessen**
von M. Stemmler (2010), xv, 196 Seiten
ISBN: 978-3-89336-678-1

91. **Untersuchung und Optimierung der Serienverschaltung von Silizium-Dünnschicht-Solarmodulen**
von S. Haas (2010), ii, 202 Seiten
ISBN: 978-3-89336-680-4

92. **Non-invasive monitoring of water and solute fluxes in a cropped soil**
by S. Garré (2010), xxiv, 133 pages
ISBN: 978-3-89336-681-1

93. **Improved hydrogen sorption kinetics in wet ball milled Mg hydrides**
by L. Meng (2011), II, 119 pages
ISBN: 978-3-89336-687-3

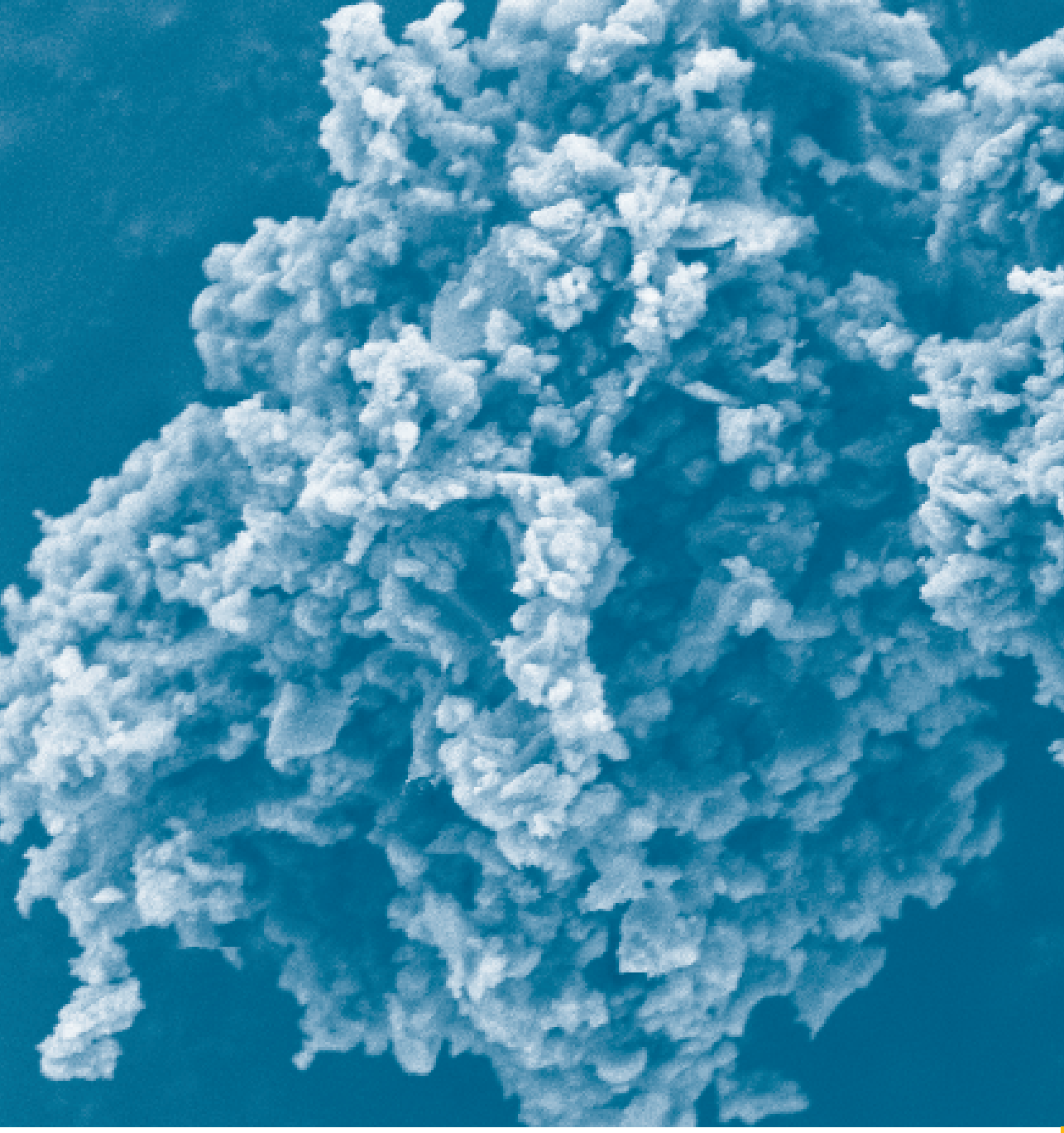

Energie & Umwelt / Energy & Environment
Band / Volume 93
ISBN 978-3-89336-687-3

JÜLICH
FORSCHUNGSZENTRUM